

MASTER

An investigation into the replacement of mercury by indium iodide or tin halides in high-intensity discharge lamps

Lemmens, T.L.

Award date:
2013

[Link to publication](#)

Disclaimer

This document contains a student thesis (bachelor's or master's), as authored by a student at Eindhoven University of Technology. Student theses are made available in the TU/e repository upon obtaining the required degree. The grade received is not published on the document as presented in the repository. The required complexity or quality of research of student theses may vary by program, and the required minimum study period may vary in duration.

General rights

Copyright and moral rights for the publications made accessible in the public portal are retained by the authors and/or other copyright owners and it is a condition of accessing publications that users recognise and abide by the legal requirements associated with these rights.

- Users may download and print one copy of any publication from the public portal for the purpose of private study or research.
- You may not further distribute the material or use it for any profit-making activity or commercial gain

An investigation into the replacement of
mercury by indium iodide or tin halides
in high-intensity discharge lamps

T.L. Lemmens BSc

2013

Eindhoven University of Technology

Under supervision of:
ir. A. J. Rijke
dr. ir. S. Nijdam
prof. dr. ir. G. M. W. Kroesen

Abstract

In this study we investigated the possibility to replace mercury by metal-halide molecules in the filling of CMH lamps, since mercury is a poisonous substance. Indium iodide was considered a viable alternative, because atomic indium has a high electron-atom collisional cross section.

Several lamps were created, in which the indium iodide content was varied, as well as the addition of sodium iodide and dysprosium iodide. The spectra of the lamps were measured in an integrating sphere and their energy balances were determined. The spectra showed that indium iodide emits a broad continuum in the visible and infrared part of the spectrum. There was also a complete absence of ultraviolet radiation. The plasma properties in the core of the discharge were determined from the integrating-sphere measurements. Atomic indium lines were used to calculate the core temperature, and a simplified model, developed by Elenbaas, was used to calculate the atomic indium and electron densities. This way, we determined that the broad band continuum was not caused by bremsstrahlung or recombination radiation, but rather by molecular radiation emitted by InI molecules.

Varying the indium iodide content in the lamps confirmed that indium iodide increased the resistivity of the lamps and indeed functioned as a buffer gas. However, the application of the Elenbaas model on the integrating-sphere measurements suggested that indium iodide led to contraction of the arc column.

A separate side-on setup was created to measure the spectrum as a function of the lateral position in the lamp. A series of measurements over the total lateral width of the lamp were Abel transformed in order to create a radial temperature profile, which showed contraction of the arc. This was also confirmed by photos taken with a cross polarized filter. Contraction by indium iodide can lead to arc instability and limits the use of additives in CMH lamps.

A different set of lamps was created that contained tin bromide and tin iodide as an alternative to mercury. These were only measured in the integrating sphere. The spectra of these lamps showed the same trends as the indium iodide lamps. We therefore concluded that neither indium iodide nor tin halides are a suitable alternative to mercury.

Contents

1	Introduction	1
1.1	Operation	2
1.1.1	Start-up phase	2
1.1.1.1	Townsend Avalanche	2
1.1.1.2	The influence of pressure	2
1.1.1.3	Voltage and current during the start-up phase	3
1.1.2	Steady-state phase	4
1.1.2.1	Physical properties	4
1.1.2.2	Electrical properties	5
1.1.2.3	Cataphoresis and de-mixing	6
1.2	Design and terminology	6
1.2.1	Components	6
1.2.2	Lamp driver	8
1.2.3	Photometry	8
1.3	Replacing mercury in HID lamps	8
1.4	Energy balance	9
1.5	Project goals	11
2	Theory	13
2.1	Notation	13
2.2	Maxwell-Boltzmann	13
2.3	Power in the discharge	14
2.4	Radiation	16
2.4.1	Line radiation	16
2.4.2	Molecular radiation	17
2.4.3	Bremsstrahlung and recombination radiation	17
2.4.4	Thermal radiation	18
2.5	Thermal conductivity	18
2.6	Channel model	19
2.7	Elenbaas plots	20
2.8	Abel inversion	22

3	Experimental setup and calibration methods	25
3.1	General setup	25
3.2	Spectrometers	27
3.2.1	FTIR theory	27
3.2.2	Measurement procedures	28
3.3	Integrating sphere	30
3.3.1	Integrating sphere theory	30
3.3.2	Integrating sphere design	33
3.3.3	Integrating sphere calibration	36
3.3.3.1	Theory of the calibration	36
3.3.3.2	Calibration sources	37
3.3.3.3	Integrating sphere error analysis	41
3.4	Side-on setup	50
3.4.1	Side-on setup design	50
3.4.2	Calibration of the side-on setup	52
3.4.3	Side-on setup error analysis	52
4	Experimental procedures	57
4.1	Determining the energy balance	57
4.1.1	Plasma radiation	57
4.1.2	Thermal radiation	57
4.1.3	Conduction losses via holder legs	59
4.1.4	Electrode losses	59
4.2	Determining Elenbaas plots	60
4.3	Determining discharge parameters	61
4.4	Abel inversion of the side-on measurements	67
5	Experimental results	69
5.1	Indium iodide	69
5.1.1	Lamp spectrum	70
5.1.2	Radiative processes in InI lamps	72
5.1.2.1	Atomic line radiation	73
5.1.2.2	Bremsstrahlung and recombination radiation	74
5.1.2.3	Molecular radiation	76
5.1.3	Boltzmann plots	77
5.1.4	Elenbaas plots	80
5.1.5	Energy balance	82
5.2	Indium iodide lamps with additives	83
5.2.1	Lamp spectrum	83
5.2.2	Boltzmann plots	84
5.2.3	Elenbaas plots	87
5.2.4	Energy balance	87
5.3	Side-on measurements on InI lamps	88
5.3.1	Photos	89

5.3.2	Side-on measurements	92
5.4	Tin halides	98
5.4.1	Tin bromide	99
5.4.2	Tin iodide	103
6	Conclusion and outlook	107
6.1	Conclusion	107
6.2	Outlook	108

Contents

Chapter 1

Introduction

A gas discharge lamp is an artificial light source that generates light by creating an electrical discharge through an ionized gas. When the lamp is in operation, free electrons, accelerated by the electrical field in the tube, collide with the atoms in the discharge. Some electrons in the orbitals of the atoms will be excited by the collisions. When the excited atoms fall back to a lower energy state, they emit photons, resulting in radiation.

Our work focused on a specific type of gas discharge lamps: the high-intensity discharge (HID) lamps. In these lamps, light is produced by means of an electric arc between two electrodes. The electrodes are usually made of tungsten, housed inside a translucent or transparent discharge tube. HID lamps are filled with a variety of species that have different functions. The gas that is used to start the discharge is called the start-up gas, while other species are added because they are strong radiators of visible radiation. The species in the discharge with which the free electrons predominantly collide, and which is therefore responsible for the resistive properties of the discharge, is called the buffer gas, which was the focus of our research. In ceramic metal-halide (CMH) lamps, a variation of the HID lamp, this buffer gas is mercury, which is a poisonous substance. Consequently, efforts are being made to replace mercury in CMH lamps. In this project we researched the possibility of replacing mercury with metal-halide molecules. This project was part of a larger collaboration between Philips and Eindhoven University of Technology to find a suitable replacement for mercury.

In this general introduction, the operation of a gas discharge lamp will be explained first to give a general idea about the working mechanisms of HID lamps. This can be split up into two phases: the start-up phase and the steady-state phase. A gas discharge lamp takes several minutes before it reaches a state of equilibrium. This is the start-up phase. After several minutes, the discharge will reach a steady state. Both phases will be explained separately, but in this work we were mostly interested in the steady state operation of CMH lamps.

After that, the design of an CMH lamp is shown and the different components are named. The important parameters in lamp design, such as efficacy, color temperature and color rendering, will be explained. An short analysis of the problems of mercury replacement will be given. Finally, an outline of the project and its goals are defined.

1.1 Operation

The actual operation of the lamp can be split up into two phases: the start-up phase and the steady-state phase.

1.1.1 Start-up phase

1.1.1.1 Townsend Avalanche

Typical gas discharge lamps are filled with an inert noble gas and additional materials. Depending on these materials, the lamp will behave differently. A discharge lamp that contains mercury and additional metal halides is called a metal-halide lamp. At room temperature the mercury and metal halides are not vaporized, but present in liquid or solid form in the so-called ‘salt pool’. In order to vaporize mercury and metal halides and heat up the discharge tube, a noble gas discharge is needed. Noble gases have the advantage that they hardly react with other species, ignite easily and that they are gaseous at room temperature. The discharge is started by applying a high-voltage peak in the order of several kilovolts, which causes an electrical breakdown in the noble gas: single electrons in the discharge are accelerated and ionize gas atoms by inelastic collisions, thus creating new electron-ions pairs. If the accelerating voltage is sufficient, enough electrons are produced to create a self-sustaining discharge. This process is called a Townsend avalanche. To aid this process, sometimes small quantities of a radioactive element are added to the filling of the lamp, to add the first free electrons that help start up the discharge [1]. Another method is the use of emitters at the electrodes to reduce their work function.

1.1.1.2 The influence of pressure

The pressure of the starter gas is an important factor in starting the discharge. According to Paschen’s law, there is an optimum value for the gas pressure. If the pressure is too low, the mean free path of the electrons is too large, meaning that they may not even hit one gas atom at their way through the discharge or that their energy gain between collisions is much higher than the ionization energy, reducing the efficiency of ion and electron production. Increasing the pressure leads to smaller mean free paths, making the ionizing process more efficient. However, if the pressure becomes too large, the mean free path becomes too small, i.e. the electrons will not be accelerated sufficiently to ionize the gas atoms.

After the initial startup, the discharge will warm up the lamp and the metals and other additives will start evaporating. Their final vapor pressure is determined by the cold spot temperature, i.e. the coldest spot on the wall of the burner. This spot is where the unevaporated metals and metal halides will accumulate. If not all of the metals and metal halides are evaporated after the lamp reaches equilibrium, the lamp is called saturated. If everything is evaporated, the lamp is called unsaturated.

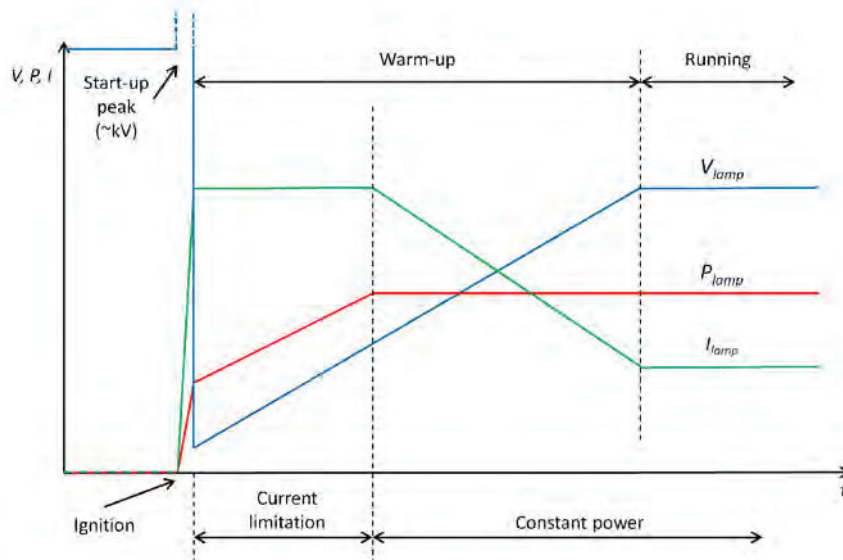


Figure 1.1 The development of the voltage, current and input power during the start-up phase.

1.1.1.3 Voltage and current during the start-up phase

A gas discharge lamp does not behave like an ohmic resistor, for which the number of free electrons carrying the current is fixed. Doubling the current leads to a doubling of the voltage, which is linearly related to the velocity of the electrons, hence a constant number of free electrons. A gas discharge lamp behaves rather differently. Generally, in a gas discharge lamp, the number of free electrons increases more than linearly with the current. This results in a negative voltage-current characteristic. This has consequences for the stability of the lamp. For instance, a discharge connected to a conventional voltage source V_0 will carry a current I_0 . If the lamp current increased by a small amount ΔI , a smaller lamp voltage drop $V_0 - \Delta V$ is needed. At this point the voltage drop over the discharge becomes ΔV higher than necessary. This will increase electron velocity. A higher electron velocity means more coulombs per seconde and therefore a higher current I . This leads to a snowball effect until the current has increased enough to blow the fuse.

To counter this effect, modern HID lamps are operated with an electronic ballast, which starts and operates the lamp and ensures an efficient steady-state operation at a constant power. Figure 1.1 shows a typical start-up profile for metal halide lamps. Before ignition, the lamp is an open circuit with an applied voltage of around 400 V. By applying a high-voltage pulse, the lamp ignites, after which the lamp voltage quickly drops to a very low value due to the low resistance of the lamp. Because the voltage-current characteristic is negative, the lamp current would increase to a very high value. It should therefore be limited to a maximum value. The discharge causes the lamp to warm up and become more resistive, so the lamp voltage and power will increase. After

a while the maximum power is reached and electric driver switches from a constant-current to a constant-power mode. The discharge will continue warming up until it reaches equilibrium.

1.1.2 Steady-state phase

1.1.2.1 Physical properties

In section 1.1.1 it was already mentioned that pressure plays an important role in the start-up phase of the discharge. This is no different for the steady-state phase. In a conventional low-pressure lamp the energy is dissipated into the discharge via the electrons. They gain enough energy between collisions to directly excite the metal atoms in the discharge, that may emit radiation when they de-excite.

Metal-halide lamps operate under high pressure, so its radiation process is different. Under high pressure the mean free path of the electrons decreases and the number of collisions increases. Although the transfer of kinetic energy from electrons to heavy particles is only a very small percentage of the kinetic energy of the electrons, the huge number of collisions causes a considerable energy transfer from the electrons to the heavy particles, even so far that the plasma is in local thermal equilibrium (LTE), so that locally all species in the discharge have the same intensive parameters (e.g. pressure and temperature). This is different from low-pressure discharge lamps, where the particle are not in LTE [2, 3]. Discharges that are in LTE can be described by these few parameters. This will be explained in detail in chapter 2.

In the core of the discharge of HID lamps the heavy particle temperatures are typically around 6000 K [4], although the exact temperature depends on the lamp filling, operation conditions, lamp design, et cetera. At these temperatures, the thermal excitation of atoms and molecules is sufficiently high, resulting not only in resonance radiation, but also radiation from transitions between excited states and molecular radiation. Electromagnetic spectra are therefore very useful in determining processes and conditions inside HID lamps.

Metal-halide lamps are filled with a starter gas, a buffer gas and metal halides. The discharge will be heated by mercury-electron collisions, mercury having a large electron-atom collisional cross section. In this case the presence of mercury mainly affects the electrical properties of the discharge, hence mercury acts as a buffer gas. The evaporated metal halides will dissociate in the discharge. The resulting metal atoms have much lower excitation level energies than mercury (e.g. sodium), so their line radiation will dominate the spectrum.

The pressure in HID lamps is often high enough that the resonance lines will be missing from the spectral power distribution, because they are reabsorbed in the outer part of the plasma in the discharge tube, called the mantle. Since the mantle is much colder than the center of the plasma, called the core, the density of atoms is much higher there, plus relatively more of these atoms are in the ground state and capable of absorbing resonance radiation. The mantle of the plasma also contains the metal-halide molecules, which under circumstances are also capable of absorbing radiation from the

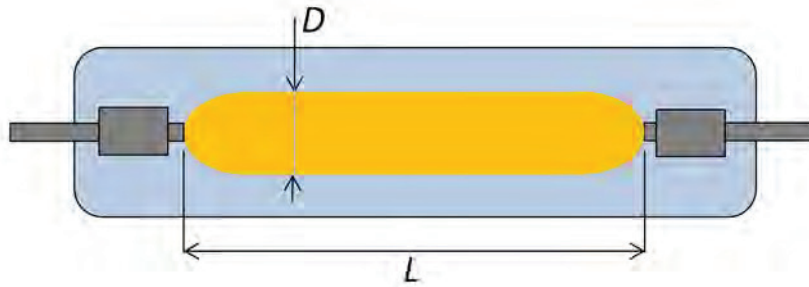


Figure 1.2 A schematic diagram of a discharge. The resistivity of the discharge can be influenced by either the geometry or the plasma properties.

center and in turn emit a molecular radiation. The reabsorption of radiation in the mantle aids in broadening the arc column and stabilizing the discharge. The exact behavior and spectrum of the metal-halide lamp are therefore strongly dependent on the specific filling.

The reason that the radiating species are added to the contents of the lamp as metal halides instead of pure metals is twofold. The first reason is that salts often are much easier to evaporate than metals [5], because generally speaking metals are easier to evaporate when present in the molecular form of a salt than in their elemental form. Once the salts have evaporated they will diffuse to the core, where they will dissociate into atoms. The metal atoms will be excited thermally and will emit (useful) visible radiation. Once they diffuse towards the mantle they will again recombine with the halogen atoms.

This introduces the second function of the salts: the halogen part of the halide is part of the halogen cycle that is also present in halogen lamps. Normally, the tungsten electrodes will slowly evaporate under the influence of the intense heat. Once tungsten atoms are in the discharge, they will mostly deposit on the cool burner wall. This will cause the burner to darken, called ‘blackening’. However, if there are halogens present in the mantle, they will react with the tungsten, ensuring that it is not (or more slowly) deposited on the wall. The tungsten does not necessarily redeposit on the electrodes, so the electrodes will still wear out over time.

1.1.2.2 Electrical properties

The electrical properties of the gas are mainly determined by the buffer gas. The main goal of the buffer gas is to make the discharge more resistive, lowering the current. A low current significantly reduces electrode losses, i.e. the amount of input power that is lost in heating up the electrodes [6]. It also limits the need for electronic control gear and lamp construction.

Figure 1.2 shows a schematic diagram of the discharge in simplified form, with dis-

charge length L and discharge diameter D . The impedance R of the discharge is given by

$$R = \frac{4m_e \nu_m L}{\pi e n_e D^2}, \quad (1.1)$$

with m_e the electron mass, e the elementary charge, ν_m the electron-atom collisional frequency and n_e the electron density. This expression shows that the resistivity of the discharge can be influenced by the properties of the buffer gas. It needs a high electron-atom collisional frequency and a high ionization potential to increase the resistivity. A high ionization potential can limit the electron density in the core. However, in most lamps ionization of the metal additives will be the dominant process for the electrons in the discharge.

The geometry of the discharge tube also influences the resistivity. A long discharge tube has a larger discharge length, which increases the resistivity. As a consequence the diameter of the discharge tube will need to be small to limit the volume of the discharge tube, which is needed to create enough pressure in the lamp. A thinner discharge tube will heat up more than a wider discharge tube. A hotter discharge tube wall will consume power, which is therefore not emitted as (useful) discharge radiation. Hence the design of the discharge tube is a trade-off between resistivity and power lost to the wall.

There is a limit to the discharge diameter D . If the diameter becomes too small with respect to the diameter of the wall, the discharge can become unstable. This is called arc contraction. This can cause the lamp to flicker and has an adverse effect on the longevity of the lamp.

1.1.2.3 Cataphoresis and de-mixing

It is preferable to operate the lamp at low currents and high voltage. Low currents are necessary to increase the lifetime of the electrodes. The lamp will typically be driven by an alternating current to prevent the effect of cataphoresis. Cataphoresis occurs when a lamp is operated in DC mode. This causes an accumulation of the active species near the cathode. This can be prevented by driving the lamp with an alternating current.

De-mixing happens because the active species (e.g. the salts in metal-halide lamps) is more likely to ionize than the buffer gas. Ions are susceptible to ambipolar diffusion, of the active species leave the center of the discharge faster than they can be replaced by the diffusion of neutral atoms or molecules through the buffer gas. This may lead to depletion of the active species in the center of the discharge.

1.2 Design and terminology

1.2.1 Components

Figure 1.3 shows the image of a CMH lamp. The bottom of the lamp is the lamp socket, through which the current is fed. It flows via the conduction wires to the electrodes in the discharge tube. In the feedthrough the wires are glued to the discharge tube, so the

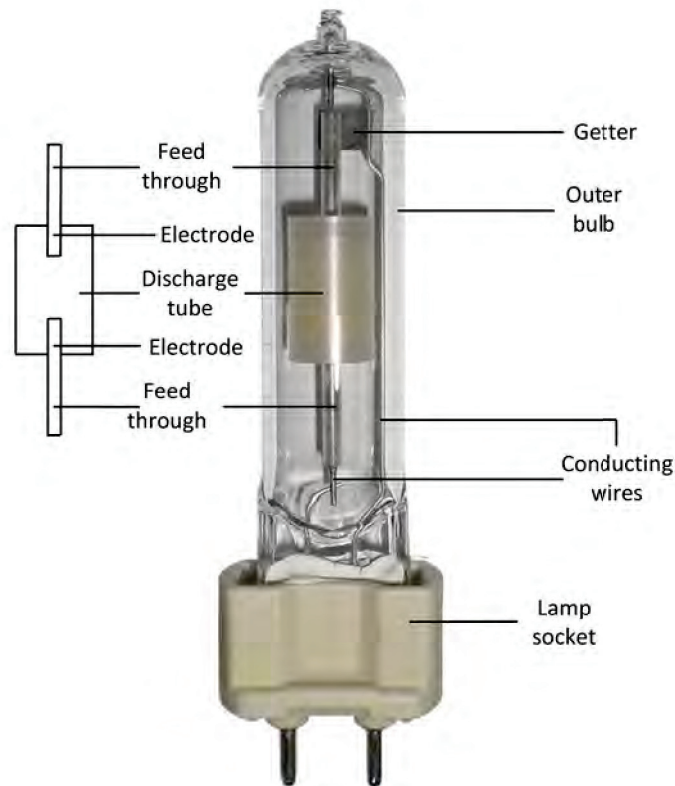


Figure 1.3 This CDM lamp shows all the basic components of a metal-halide lamp. The discharge tube contains the mixture of gasses and metal halide additives. It is contained within a low pressure environment to prevent corrosion of the discharge tube wall, which is made of PCA. The getter serves as an oxygen trap.

tube is effectively a closed vessel. It is in this discharge tube, also known as the burner, that the plasma is created.

The tube is filled with an inert gas and metal-halide additives in order to produce light. Since the burner has to withstand large temperatures, it has to be made of a heat resisting material, which is transparent or translucent. In most commercial metal-halide lamps this material is PCA (polycrystalline aluminium), but different materials, such as fused quartz, are being used in other discharge lamps (e.g. xenon-arc lamps, that are used in movie theatres). Likewise, the electrodes need to be able to withstand large temperatures to prevent them from melting, so they are made of tungsten. In turn, the feedthrough has to be made of a material with a matching thermal expansion coefficient to the PCA. It is made of either niobium alloys, ceramic metal composites or alloyed iridium.

Surrounding the discharge tube is the outer bulb, which enables the discharge tube to be contained within a low-pressure atmosphere. This is necessary to provide a stable thermal environment for the discharge tube and to isolate the hot discharge tube from the surroundings. It also blocks unwanted UV radiation. The getter is a highly reactive

material that neutralizes the remaining oxygen within the bulb.

1.2.2 Lamp driver

An HID lamp is conventionally driven by a low-frequency, square wave electronic driver [7]. The lamp should be driven by an alternating current to prevent cataphoresis of the different species in the plasma. A disadvantage of this is that the discharge will basically extinguish each time the polarity changes, since at each switch the voltage will drop below a certain threshold voltage needed to sustain the discharge. Therefore, many lamps are driven with a square wave instead of a conventional sinusoidal AC current. The square wave has a relative low frequency (~ 100 Hz) to prevent acoustic resonance. At higher frequencies, there is more interaction between the discharge and the electronic driver, which can cause problems such as instabilities, high output fluctuations and, in the worst case, cracked tubes.

1.2.3 Photometry

The most defining property of CMH lamps, and by far the most commercially important one, is the efficacy (unit: lumens per watt). Typical commercial lamps operate at an efficacy around 100 lm/W [8]. Other important qualities are the correlated color temperature (CCT) and the color rendering index (CRI). The color temperature is a measure to compare the hue of the lamp to the light of an ideal black-body radiator. The preferred CCT depends very much on the application of the lamp, but a good rule of thumb is 3000 K, as this is the CCT of incandescent lamps. The higher the CCT, the ‘bluer’ the light will appear. Finally, the CRI is a measure for the effect of the HI lamp on the color appearance of an object in comparison to the color appearance under a black-body source. The highest possible value is 100, while typical commercial CMH HID lamps have a value above 90 [8].

1.3 Replacing mercury in HID lamps

In the past decades there has been an increased awareness and understanding of environmentally and health related issues of mercury [9, 10]. This has led to an increased effort from lamp manufacturers to eliminate it from their products. However, any mercury-free lamp would have to perform equal to the current commercial models on the market in order to become attractive as a substitute. So far no suitable replacements have been found, mainly because mercury has a unique combination of properties:

- Mercury is chemically inert and therefore does not react with the wall or the electrodes.
- Mercury is the only metal that is liquid at room temperature and has a very low enthalpy of vaporization (59.23 kJ/mol). It is therefore possible to reach a high vapor pressure of mercury at relatively low cold spot temperatures.

- Mercury has a large electron-atom collisional cross section and therefore a high electron-atom momentum transfer frequency ν_m . This leads to a lower lamp current at the same power input.
- Mercury atoms are heavy, which means that they have a low thermal velocity and hence a low thermal conductivity. This reduces the amount of power that is lost to the wall. It also reduces the evaporation rate of the electrodes.
- The high excitation and ionization levels of mercury significantly limit its contribution to the spectrum in metal-halide lamps. This makes it possible to create and adjust the spectrum in metal-halide lamps by adding salts to the lamp filling. It also means that mercury will not contribute to the electron production and therefore has no adverse effect on the plasma resistivity.
- Mercury binds with free iodine, which makes it even easier to evaporate. This eases cold ignition and even speeds up warm restrike. It also reduces the free iodine pressure.

It is clear that mercury is dominant in the behavior of the discharge and that its removal will greatly alter it. A straightforward strategy for mercury replacement is to select substitutes which have properties similar to mercury. Already in 1964 Reiling [11] concluded that quartz metal-halide lamps with a noble gas as a buffer gas had a much lower efficacy than lamps that contained mercury. In the meantime other alternatives have been investigated, such as zinc [12, 13]. Metallic zinc shares several properties with mercury. The most important one is that the momentum transfer cross section for elastic electron scattering is similar to mercury. However, zinc also suffers several drawbacks. For one, mercury is very volatile. As a consequence, and in contrast to zinc, mercury lamps can be operated in unsaturated mode. The vapor pressure of mercury is therefore directly related to the total mass of mercury in the salt pool. The fact that zinc lamps have to be operated in saturated mode makes it much harder to accurately tune the vapor pressure of zinc in the discharge. Additionally, zinc suffers from larger thermal losses. Experiments that were not part of this project have also shown that lamps with zinc filling are prone to blackening and that zinc can react with various lamp components. Especially the latter problems need to be resolved first to make zinc a suitable alternative to mercury. The problems with zinc illustrate the difficulty of finding a suitable alternative to mercury, especially the difficulty of reaching a high vapor pressure when elemental metals are used as lamp filling. For this reason attempts are made to replace mercury with metal halides. We already showed that metal halides are used in CMH lamp to increase the efficacy, but in this case the metal halides are not added for their radiative, but for their resistive qualities.

1.4 Energy balance

Figure 1.4 shows a diagram of the energy balance, i.e. an overview of the different energy flows, in HID lamps. An energy balance shows via which processes the input power is

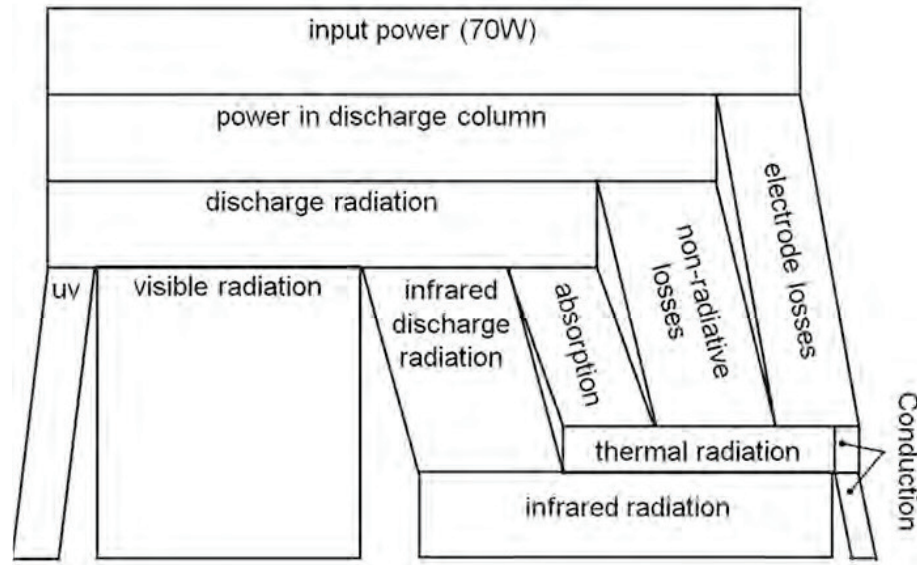


Figure 1.4 The energy balance of a discharge lamp.

lost. The lamps used in this work typically worked with an input power of 70 W. Part of this power is transferred to the electrodes by charged particles. This heats them up to the temperature required for secondary electron emission. The rest of the power is dissipated in the discharge column. Most of this power will be converted into radiation, while the rest of this power will be transferred by conduction to the burner wall, which are called non-radiative losses. The power lost to non-radiative processes is determined by the local thermal conductivity and temperature gradient at the wall, in accordance with Fourier's expression for heat flux. However, the wall is not just heated by the conduction to the wall. The wall is never fully transparent, so it will also absorb some of the radiation emitted by the plasma. The rest of the radiation will pass through in the form of ultraviolet, visible and infrared radiation.

Most of the radiation in the plasma will be emitted by atomic and molecular species. Radiation is not only emitted from the core, but from the cooler parts of the discharge as well. Part of the infrared radiation is the result of electron-atom and electron-ion interactions. This is called bremsstrahlung. Because electrons mainly exist in parts of the discharge where the temperature is high enough to ionize the atoms, bremsstrahlung originates from the core of the plasma. We explained that the wall is heated up by a combination of conductive heat flux to the wall and absorption of part of the plasma radiation. The wall will mainly lose its energy as (infrared) thermal radiation. Together with the infrared plasma radiation and the thermal radiation of the electrodes it makes up the total infrared output of the HID lamp. The remaining power will leave the system by means of conduction to the metallic structure holding the ceramic tube.

The determination of an energy balance is vital to help understand the energy flows

in the lamp. For a long time the determination of the energy balance of HID lamps has been an important aspect of HID lamp research [2, 14, 15]. It can aid in the improvement of existing lamps and the development of new ones and is therefore very useful for lamp designers.

Up until now, energy balance measurements were limited, as most research focuses on the visible output of the lamps. Yet even in the most efficient cases less than half of the input power ends up as visible radiation. In fact, most of the input power ends up as infrared radiation [16]. So far, studies on infrared radiation were limited to a wavelength of 2.5 μm . Another limiting factor was that most of the measurements were carried out in the form of side-on infrared measurements [15, 17, 18]. During this study we could determine the spectral power of lamps over the full range of the spectrum and calculate the total discharge radiation power. We also conducted experiments to determine the other components of the energy balance, such as the non-radiative losses and electrodes losses.

During our study spectrally resolved, absolutely calibrated integrating sphere measurements were used to determine the infrared contributions to the spectrum up to 10 μm . An integrating sphere makes it possible to measure the spectral power of a lamp, independent of spatial or angular variations in the radiation output of the lamp. In the ideal case this means measurements in integrating spheres do not depend on the angular profile of the source and spatial distribution – only the input power. In some cases these measurements were combined with side-on measurements on the lamp to locally determine the source of the radiation.

In most commercial HID lamps the ultraviolet output is limited by the outer bulb, which contains a UV blocker. We therefore removed the outer bulb in our integrating sphere measurements.

1.5 Project goals

The focus of this research was to understand the behavior of mercury-free metal halide lamps with a variety of fillings. Prior to this project an array of different solutions have already been tried, ranging from high-pressure xenon to magnesium(-iodides), but this has not resulted in a solution.

In our research we focused on indium iodide as a replacement for mercury. Indium was considered to be a viable alternative, since it has an even larger electron-atom cross section than mercury. Lamps were filled with indium iodide in order to create a sufficient atomic indium vapor pressure in the discharge, since metal halides evaporate more easily than metals.

Several lamps were created with various amounts of indium iodide filling. Earlier tests showed that indium iodide indeed improved the resistivity of the lamps, but that its spectrum contained a broad band continuum. The main goal was to understand the influence of indium iodide on the discharge. More specifically we wanted to determine the source of this continuum radiation and to determine what caused the increased resistivity in the discharge. This way we could determine whether indium iodide was a

Chapter 1 Introduction

suitable replacement for mercury.

We also tested several lamps with tin iodide and tin bromide. Because of time constraints these lamps could not be measured as extensively as the indium iodide lamps. The goal of these measurements was to determine whether there were parallels between the tin-halide lamps and the indium-iodide lamps and investigate whether tin-halide lamps merited more research.

Chapter 2

Theory

Much of this project focuses on the spectral power distribution of metal-halide lamps. It is therefore necessary to explain the theory behind the radiation of these lamps, as well as how it can be used to determine other characteristics of the lamps.

2.1 Notation

In spectrometry, spectral powers are often measured as a function of the wavenumber (unit cm^{-1}). This is symbolized by $\tilde{\nu}$. The wavenumber of a photon is related to the frequency ν and wavelength λ via

$$\tilde{\nu}[\text{cm}^{-1}] = \frac{10^7}{\lambda[\text{nm}]} = \frac{\nu[\text{Hz}]}{100c}. \quad (2.1)$$

Furthermore, physical quantities, such as the power, can have a symbol for radiation as a subscript, be it λ , ν or $\tilde{\nu}$. This means that this is the spectral variant of the quantity. For a hypothetical quantity X this is expressed as

$$X = \int X_\lambda d\lambda. \quad (2.2)$$

2.2 Maxwell-Boltzmann

The Maxwell-Boltzmann distribution is a probability density function that has its roots in the kinetic theory of gases. It is used to describe many fundamental gas properties, but in plasma physics it can also be used to calculate densities of excited particles, temperature profiles, and so on. The Boltzmann distribution is a probability density function for the distribution of an amount of energy between identical but distinguishable particles in a closed system. It assumes that there is no constriction to the number of particles in a certain state and that the system is in local thermal equilibrium. It is for that reason that the Boltzmann distribution can only be applied to high-density

plasmas. Under these condition, the probability of a particle having energy E_i is given by

$$\frac{N_i}{N} = \frac{g_i e^{-\frac{E_i}{kT}}}{\sum_j g_j e^{-\frac{E_j}{kT}}}, \quad (2.3)$$

where N_i is the number of particles at equilibrium temperature T having energy level E_i , N is the total number of particles in the system, g_i the degeneracy factor of each energy state i and k is the Boltzmann constant.

This distribution function can be applied to the atoms in our discharge, since there is no restriction on the number of atoms is a certain excited state and since it is assumed that the discharge is in thermal equilibrium. The density n_i of atoms being in the excited state with energy E_i is then given by

$$n_i = n_0 \frac{g_i}{Z} e^{-\frac{E_i}{kT}}, \quad (2.4)$$

where n_0 is the total particle density of atoms and Z is the partition function, i.e. the sum over all possible states:

$$Z = \sum_i g_i \exp(-E_i/kT). \quad (2.5)$$

2.3 Power in the discharge

Power is coupled into the arc of the discharge via collisions of electrons and heavy particles. This can be expressed as the total power coupled into the discharge discharge P_{dis} :

$$P_{\text{dis}} = P_{\text{la}} - P_{\text{el}}, \quad (2.6)$$

with $P_{\text{la}} = U_{\text{la}} I_{\text{la}}$ the total lamp power and P_{el} the power lost to the electrodes. The lamp voltage and current are expressed by U_{la} and I_{la} , respectively. If the arc of the discharge is cylindrically symmetric, with radius R and length d , with d being the distance between the electrodes, then the discharge power is described by

$$P_{\text{dis}} = dE^2 \int_0^R \sigma(T(r)) dr, \quad (2.7)$$

with E the electric field in the arc, σ the electrical conductivity in the arc, which depends on a temperature T . In HID lamps the temperature varies with the radius r . The electric field is given by

$$E = \frac{U_{\text{la}}}{d}. \quad (2.8)$$

The current density J and the electric field E can be used to calculate the electrical conductivity σ :

$$\sigma = \frac{J}{E}. \quad (2.9)$$

The current density can be viewed as the number of electrons moving with a drift velocity v_d across the arc:

$$J = v_d n_e e, \quad (2.10)$$

with e the elementary charge of the electrons and n_e the electron density. In its turn, the drift velocity can be expressed as a function of the electron mobility μ and the electric field:

$$v_d = \mu E. \quad (2.11)$$

Equations 2.9, 2.10 and 2.11 can be combined to give an expression for the electrical conductivity:

$$\sigma = e n_e \mu. \quad (2.12)$$

The electrical conductivity in the arc therefore only depends on the electron density and the electron mobility. Both can be calculated.

The electron density in an ionized plasma can be described as a function of temperature, density and ionization energies of the atoms. This is expressed by the Saha equation, which can be used to describe ionization in gas discharge lamps. The Saha equation of single ionized atomic species, where the ion density is equal to the electron density, is

$$\frac{n_e^2}{n_a} = 2 \left(\frac{2\pi m_e kT}{h^2} \right)^{3/2} \frac{g_i}{Z} \exp\left(-\frac{E_i}{kT}\right), \quad (2.13)$$

with m_e the electron mass, n_e the electron density, and n_a the neutral atom density and T the temperature, both of which depend on the radius r . The degeneracy of the ionization level is expressed by g_i , Z the partition sum of the neutral atoms and E_i the ionization energy of the atom.

The electron mobility depends on the electron-atom collisional cross section $Q_{ea}(v)$, which depends on the electron velocity v . The electron velocity for a certain temperature is determined by the Maxwell-Boltzmann equation. This distribution has an average electron velocity $\langle v \rangle$:

$$\langle v \rangle = \sqrt{\frac{8kT}{\pi m_e}}, \quad (2.14)$$

with k Boltzmann's constant. Q_{ea} can be calculated for $\langle v \rangle$, and will therefore no longer be a function of v , but a value that only depends on the temperature: Q_{eam} . This results in this expression for the electron mobility:

$$\mu = 0.75 \frac{e}{m_e n_a Q_{eam} \langle v \rangle}. \quad (2.15)$$

In conclusion, the electrical conductivity depends on the electron mobility and electron density, which in their turn only depend on the radius-dependent temperature and neutral particle density:

$$\sigma(T) = 0.75 \frac{e^2 n_e}{m_e n_a Q_{eam} \langle v \rangle}. \quad (2.16)$$

2.4 Radiation

There are different radiation processes in an HID lamp: line radiation, molecular radiation, bremsstrahlung, recombination radiation and thermal radiation.

2.4.1 Line radiation

One of the most important light-emitting processes in metal-halide lamps is line radiation. Line radiation is the result of photons that are produced by bound electrons that fall back to a lower energy state. The amount of emitted power P_{ul} per unit volume V by electrons that fall back from the upper energy level E_u to the lower energy level E_l is given by

$$\frac{P_{ul}}{V} = n_u A_{ul} E_{ul}, \quad (2.17)$$

where n_u is the density of atoms in energy state E_u , A_u is the Einstein coefficient for spontaneous emission and $E_{ul} = E_u - E_l = h\nu_{ul}$ is the energy of the emitted photon. This expression can be combined with the Boltzmann distribution:

$$\frac{P_{ul}}{V} = h\nu_{ul} A_{ul} n_0 \frac{g_u}{Z} e^{\frac{-E_u}{kT_e}}. \quad (2.18)$$

This shows that the emitted power per atomic line in our discharge only depends on the density of the radiating species n_0 and the temperature, which makes line radiation a useful tool for diagnosis of the spectrum. Equation 2.18 can be rewritten as:

$$\ln \left(\frac{P_{ul}}{h\nu_{ul} A_{ul} g_u} \right) = -\frac{E_u}{kT} + \ln \left(\frac{V n_0}{Z(T)} \right). \quad (2.19)$$

2.4.2 Molecular radiation

Since many additives are added to metal halide lamps as molecules, part of the spectrum will consist of molecular radiation. The energy levels of molecules are more complicated than those of atoms, because molecules, in addition to the electron configuration, have additional vibrational and rotational degrees of freedom due to the motions of their nuclei. The ground state and excited states are therefore divided in energy levels that represent the various vibrational and rotational states. As a result, molecular radiation does not take the form of one sharp emission line, like atomic radiation, but rather a combination of lines over a broader part of the spectrum. Because of the high pressure in HID lamps, spectral lines are often broadened, and since molecular lines are grouped closely together, molecular radiation will often appear to have the form of a continuum.

Molecular densities will be higher in the mantle of the discharge, as molecules tend to dissociate in the hotter core environment. However, the ratio of molecules that is dissociated depends heavily on the type of molecule and it is possible that some molecules still have a considerable density in the core. Besides density and temperature, calculating molecular radiation requires knowledge of the potential curves as a function of intermolecular separation and accurate transition probabilities. It is therefore considerably more complex than atomic radiation and requires modeling to exactly predict molecular radiation.

2.4.3 Bremsstrahlung and recombination radiation

Bremsstrahlung and recombination radiation are the result of free electrons colliding with atoms and ions. If the electron is captured by an ion in a free-bound collision, recombination radiation is emitted. If the electron is just deflected it will still lose energy in the form of radiation. These free-free collision produce e-a bremsstrahlung if the electron is deflected by an atom and e-i bremsstrahlung if the atom is deflected by an ion. The collisions involve a free particle, so, opposed to the molecular radiation, the resulting radiation will form a continuum.

Bremsstrahlung and recombination radiation can be expressed via the emission coefficient j_λ . The emission coefficient can be explained as the local intensity in a plasma. Integrating the emission coefficient over a line of sight will result in the spectral intensity. The three contributions to the continuum can be expressed by equations that only depend on the main plasma parameters electron temperature T_e , the electron density n_e , the charge number of the ion Z and the ion density n_i .

Recombination radiation can be expressed by [19]

$$j_\nu^{\text{rec}}(\nu, T_e) = c_1 Z^2 \frac{n_e n_i}{(k_B T_e)^{1/2}} \exp\left(-\frac{h\nu}{k_B T_e}\right) \xi^{\text{rec}}(\nu, T_e), \quad (2.20)$$

with

$$c_1 = \frac{16\pi}{3c^3(6\pi m_e^3)^{1/2}} \left(\frac{e^2}{4\pi\epsilon_0}\right)^3. \quad (2.21)$$

h is Planck's constant, Z the ion charge, e is the elementary charge, m_e is the mass of the electron, k_B is Boltzmann's constant and ϵ_0 is the vacuum permittivity. The Biberman factor ξ^{rec} [20] is a correction factor that depends on the atom species, because the original expression for recombination radiation is deduced for simple systems, such as hydrogen.

The expression for e-i bremsstrahlung is

$$j_\nu^{\text{ei}}(\nu, T_e) = c_1 Z^2 \frac{n_e n_i}{(k_B T_e)^{1/2}} \left(1 - \exp\left(-\frac{hc}{\nu k_B T_e}\right) \right) \xi^{\text{ei}}(\nu, T_e), \quad (2.22)$$

which is quite similar to the expression for recombination radiation and features the same constant c_1 . This equation also contains a Biberman factor ξ^{ei} .

Finally, there is the process that creates e-a bremsstrahlung. In this case, a passing electron polarizes an atom by inducing a dipole moment. The interaction between this dipole and the electron slows the electron, so it emits radiation. The calculation of the emission coefficient depends on the collisional cross section of the electrons and atoms. This is quite complicated, as this cross section depends on the relative velocity of the electron with respect to the atom. For our purposes, it suffices to use the expression of e-a bremsstrahlung for electrons with an averaged cross section Q_{eam} :

$$j_\nu^{\text{ea}}(\nu, T_e) = \frac{32e^2}{12\pi\epsilon_0 c^3} \left(\frac{k_B T_e}{2\pi m_e} \right)^{3/2} n_e n_a Q_{\text{eam}}(T_e) \left[1 + \left(1 + \frac{h\nu}{k_B T_e} \right)^2 \right] \exp\left(-\frac{h\nu}{k_B T_e}\right). \quad (2.23)$$

2.4.4 Thermal radiation

A body at temperature T that is in thermodynamic equilibrium with its environment emits thermal radiation. The spectral radiance B_ν for a body that is perfectly opaque and non-reflective can be described by Planck's law:

$$B_\nu = \frac{2h\nu^3}{c^2} \frac{1}{e^{\frac{h\nu}{kT}} - 1}. \quad (2.24)$$

If an object is not a perfect black-body it will not absorb all incoming radiation. It is necessary to multiply the black-body curve with the spectral emissivity $\epsilon_\nu(\nu, T)$ to determine its spectral radiance. This is the ratio between the spectral radiance of the object and the spectral radiance of a perfect black-body.

2.5 Thermal conductivity

The thermal conductivity is important if we want to understand more of the non-radiative processes in the discharge. P_C is the power per unit length that is lost to the heat conduction. This is described by Fourier's law, which depends on the gradient

of the temperature T and the heat conduction coefficient λ . In a cylindrical discharge this looks as follows:

$$P_C = -2\pi\lambda(T)r \frac{dT}{dr}. \quad (2.25)$$

There are several processes in HID lamps that significantly influence this heat conduction coefficient. Expressions for these processes are often complex and depend on collision integrals of the species within the plasma. However, their influence can be determined quantitatively, since they do depend on the macro-properties of the discharge. There are three processes that influence the thermal conductivity in HID lamps [21]:

- **Translational conductivity** is the transfer of kinetic energy by heavy particles. For monatomic gases this scales with $\sqrt{T/M}$, with M the atomic weight of the atoms and T the temperature of the gas. Heavier atoms in the discharge therefore limit conduction losses.
- **Electronic conductivity** is transfer of kinetic energy by the electrons. This scales with $n_e^2\sqrt{T}$, with n_e the density of the electrons. It is only relevant in the core of the discharge, because it scales quadratically with the density of the electrons.
- **Reactive conductivity** is the transport of the heat of dissociation of a chemical reaction. In the core of the discharge, molecules in the discharge will dissociate. This is an endothermic reaction. The resulting atoms will then diffuse to the outer mantle of the discharge, where they will again associate in an exothermic reaction. This is a net transport of heat. The calculation of the reactive conductivity require literature data and is very complex.

2.6 Channel model

HID discharges are highly complex, with plasma parameters, such as electron density and temperature, varying with the radius. For high-pressure mercury lamps Elenbaas [22] used a simplified model to analyze the discharge. In this simplification the discharge is viewed as a set of two concentric cylinders, the core and the mantle. where all power is coupled into the hot core of the discharge, which produces all radiation. It is surrounded by a cold mantle, which produces no radiation. It is based on three assumptions:

- The discharge fills a cylinder with an effective radius r_{eff} , which is smaller than the radius of the discharge tube, and which forms the boundary between the core and the mantle. The total volume V_c of this cylinder is then given by

$$V_c = \pi r_{\text{eff}}^2 d, \quad (2.26)$$

with d the distance between the electrodes.

- No current flows outside the cylinder. The electron density in the mantle will be much lower than in the core due to the lower temperature there.
- The temperature inside the cylinder is uniform and shall be referred to as the core temperature T_c . This is called a ‘top hat’ temperature profile.

This simplification will be referred to as the ‘channel model’. It can be used to simplify equation 2.7, which expresses the total power coupled into the discharge discharge P_{dis}

$$P_{\text{dis}} = P_{\text{la}} - P_{\text{el}} = V_c \sigma(T_c) E^2. \quad (2.27)$$

with U_{la} the total voltage drop over the lamp, I_{la} the total lamp current and $\sigma(T_c)$ the electrical conductivity of the channel, which is also a simplified version of equation 2.16:

$$\sigma(T_c) = 0.75 \frac{e^2 n_e k T_c}{m_e p_a Q_{\text{eam}} \langle v \rangle}. \quad (2.28)$$

The collision electron-atom cross section then becomes a function of the mean velocity of the electrons $\langle v \rangle$. This is the average thermal speed of electrons in a Maxwell-Boltzmann distribution, which only depends on T_c :

The electron density n_e can be determined via Saha’s equation (see equation 2.13). The partial pressure of the atomic species p_a is the result of the ideal gas law:

$$p_a = \frac{N_a k T_c}{V_c}, \quad (2.29)$$

with N_a the total number of particles of the atomic species present in the discharge. Therefore, provided that T_c and N_a are known, V_c , and subsequently p_a and r_{eff} can be calculated.

This simplified model is highly suitable for integrating-sphere measurements, because atomic lines measured in the spectral power distribution can often be used to create Boltzmann plots, which in turn result in a temperature and the density of the radiating species. Considering the simplicity of the model, it cannot be expected to very accurately predict the properties of the discharge. It is however very useful to compare the trends in different lamps.

2.7 Elenbaas plots

Elenbaas [22] and Jack and Koedam [14] developed a theory for the flow of power from the charged particles in the center of the lamp to the discharge tube wall. We have so far established that the power in the discharge is either lost via radiation (see section 2.4) or conduction (see section 2.5).

The flows of power are visualized in figure 2.1, which shows the power flows as a function of the radius r in the discharge. The electric input power is absorbed in the hot central core. This core ranges from the center of the discharge to the effective radius

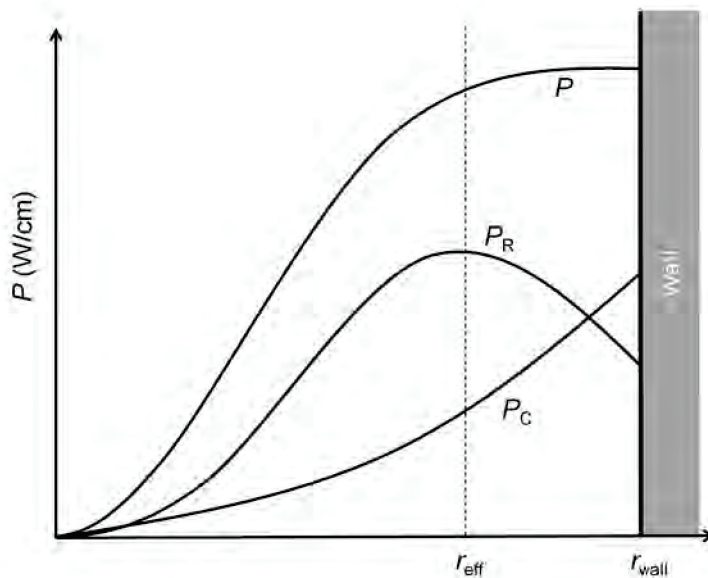


Figure 2.1 Schematic outward power flow in a discharge lamp as a function of the radius.

r_{eff} . This power is then transported towards the wall by radiation and conduction. In the cooler outer mantle part of the radiation is absorbed. A decrease in radiation power flow can be associated with an increase in the conduction power flow, because, due to the absence of the electrons and ions, the electrical conductivity is zero in the cooler outer mantle. This means that no power is dissipated in the mantle.

The total dissipated power in the discharge P_{dis} , i.e. the total lamp power minus the power lost to the electrodes (see equation 2.6), is eventually lost either in the form of radiative power P_{R} or as conduction power P_{C} , so that

$$P_{\text{dis}}(r) = P_{\text{C}}(r) + P_{\text{R}}(r), \quad r_{\text{eff}} < r < r_{\text{wall}}. \quad (2.30)$$

Elenbaas has shown that the radiative power scales with the exponent of the core temperature. Therefore, small changes in temperature result in large changes in radiative power. This makes the conduction losses independent of the input power in the first order, resulting in the following equation:

$$P_{\text{rad}} = \alpha(P_{\text{dis}} - P_{\text{C}}^*), \quad (2.31)$$

where P_{rad} is the radiative power at the wall. This is the radiative power that actually leaves the discharge. The physical interpretation of α and P_{C}^* is less straightforward.

Figure 2.1 the boundary between the hot inner core, where the electrical input power is dissipated, and the cooler outer mantle at r_{eff} . The measured discharge radiation power from equation 2.31 is given by

$$P_{\text{rad}} = P_{\text{R}}(r_{\text{wall}}). \quad (2.32)$$

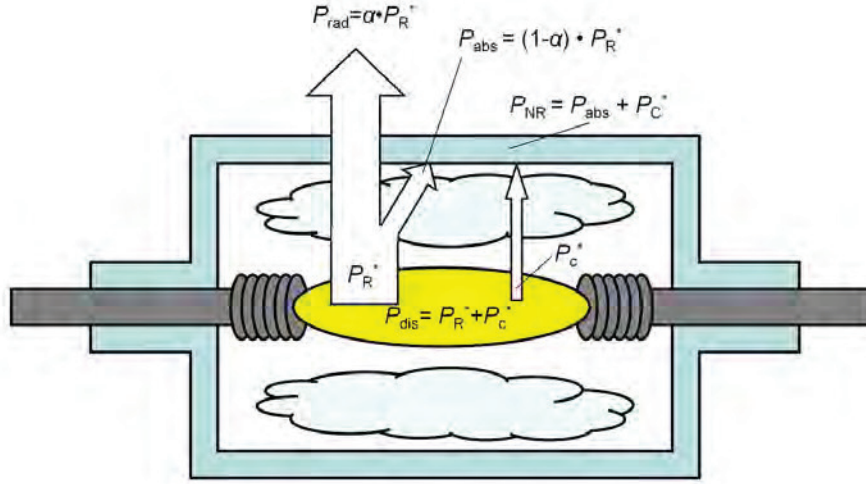


Figure 2.2 The cumulative power in an HID lamp. The Elenbaas theory can be used to determine the non-radiative losses in the discharge.

The radiation power at the wall is proportional to the radiation power at r_{eff} :

$$P_{\text{R}}(r_{\text{wall}}) = \alpha P_{\text{R}}(r_{\text{eff}}), \quad (2.33)$$

so α is a measure for the transmission of the outer mantle and the wall. Combining these equations and allowing for the electrode losses results in:

$$P_{\text{rad}} = \alpha(P_{\text{dis}} - P_{\text{C}}(r_{\text{eff}})) = \alpha(P_{\text{la}} - P_{\text{el}} - P_{\text{C}}(r_{\text{eff}})). \quad (2.34)$$

$P_{\text{C}}(r_{\text{eff}})$ is denoted by P_{C}^* and is a measure for the thermal conduction loss at the point within the arc column where the electrical conductivity drops to zero. Likewise, $P_{\text{R}}(r_{\text{eff}})$ will be named P_{R}^* . The absorbed radiative power can then be calculated:

$$P_{\text{abs}} = (1 - \alpha)P_{\text{R}}^* = \frac{1 - \alpha}{\alpha} P_{\text{rad}}. \quad (2.35)$$

This can then be used to determine the total non-radiative losses in the discharge:

$$P_{\text{NR}} = P_{\text{abs}} + P_{\text{C}}^*. \quad (2.36)$$

These power flows are visualized in figure 2.2.

2.8 Abel inversion

In order to create a deeper understanding of the lamps that were used in this project, the spectral radiances of several lamps were measured at different lateral positions. These

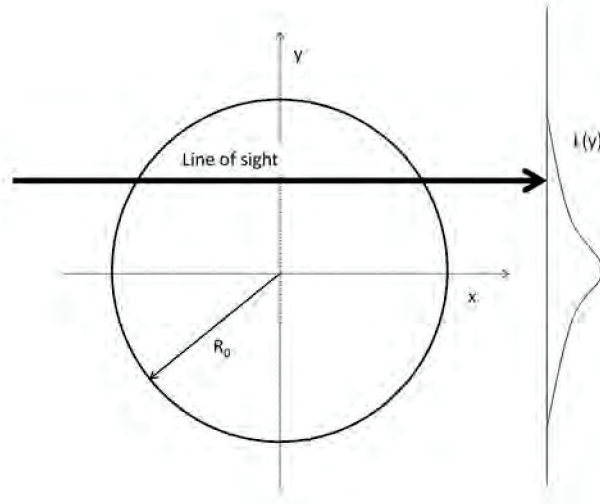


Figure 2.3 By measuring the intensity along a line of sight, it is possible to create a lateral intensity profile $L(y)$.

measurements were a projection of the emissivity along a straight chord through the lamp (see figure 2.3). This is, in essence, a line integral. Under the condition that the discharge is radially symmetric and that the emitted radiation is optically thin, it is possible to obtain radial emissivity, called the emission coefficient j from these lateral measurements of the discharge using the Abel inversion:

$$j(r) = -\frac{1}{\pi} \int_r^\infty \frac{dL}{dy} \frac{dy}{\sqrt{y^2 - r^2}}. \quad (2.37)$$

This expression also has an inverse transform that gives the original radiance L :

$$L(y) = 2 \int_y^\infty \frac{j(r)r \, dr}{\sqrt{r^2 - y^2}}. \quad (2.38)$$

Unfortunately, this inversion is fundamentally unstable [23]. Even very small errors, such as measurement noise, will be translated into large errors with these inversions. Equation 2.37 also presents the difficulty that the intensity of the plasma needs to be very accurately known at the edge of the plasma, especially when the equation is presented in its discrete form. The principle behind the equation can be viewed as the peeling of an onion: the emissivity at r is determined by peeling off the light emitted from layers of the plasma further out. This makes the discrete Abel inversion prone to large errors. Therefore, it was decided that the measured data would be fitted with functions that have an analytical solution to the Abel inversion. This method is called the Gaussian basis-set expansion Abel transform (BASEX) method [24] and was chosen because the lateral profiles of our measurements have a Gaussian-like shape. The radial

curves are described as follows:

$$\rho_k(r) = \left(\frac{e}{k^2}\right)^{k^2} \left(\frac{r}{\sigma}\right)^{2k^2} e^{-(r/\sigma)^2}, \quad (2.39)$$

where the single fitting parameter σ is of the order of the distance between the pixels. This integral over r can be evaluated analytically in equation 2.38, leading to

$$\chi_k(x) = 2\sigma\rho_k(x)\sqrt{\pi} \left[1 + \sum_{l=1}^{k^2} (x/\sigma)^{-2l} \times \prod_{m=1}^l \frac{(k^2 + 1 - m)(m - 1/2)}{m} \right]. \quad (2.40)$$

Chapter 3

Experimental setup and calibration methods

This section focuses on the setup of the experiments. A general overview of the experimental setup is given first. Three parts of the experimental setup will be discussed in-depth: the spectrometers, the integrating sphere and the side-on setup.

3.1 General setup

Figure 3.1 shows a schematic diagram of the experimental setup. In our set-up we can measure lamps with the integrating sphere or with the side-on setup. The setup consists of four parts: the power supply, the FTIR spectrometer, the integrating sphere and the side-on setup.

The integrating sphere is mounted inside a vacuum vessel. It is used to determine the total spectral power distribution of lamps mounted inside of it. Before the lamp is turned on, the vacuum vessel is evacuated. First the vessel is pumped down to a medium vacuum of around 5×10^{-2} mbar with a roughing pump. After that, the turbo pump is switched on, which will bring the pressure inside the vessel down a high vacuum of approximately 1×10^{-5} mbar. This is necessary because the discharge tube is removed from the outer bulb. As a consequence, if the lamp were switched on under atmospheric conditions, the feedthroughs would corrode very rapidly. The vacuum also prevents the absorption of radiation by air, which is especially a problem in the far-infrared part of the spectrum.

The sphere surface is actively cooled by a cooling system (Merlin Recirculating Chiller, ThermoNESLAB Instruments), which keeps it at a constant temperature. A separate cooling system (RTE-5DD, NESLAB Instruments), which also runs at a constant temperature, is used for the large baffle and the lamp holder. The cooling water flows through the baffle along the bottom of the holder legs, with the lamp attached to their tops, which can be seen in figure 3.1.

Two spectrometers are connected to the sphere. A fiber optic spectrometer (Avantes AvaSpec-HS1024×58/122) is connected to the integrating sphere via a glass fiber cable,

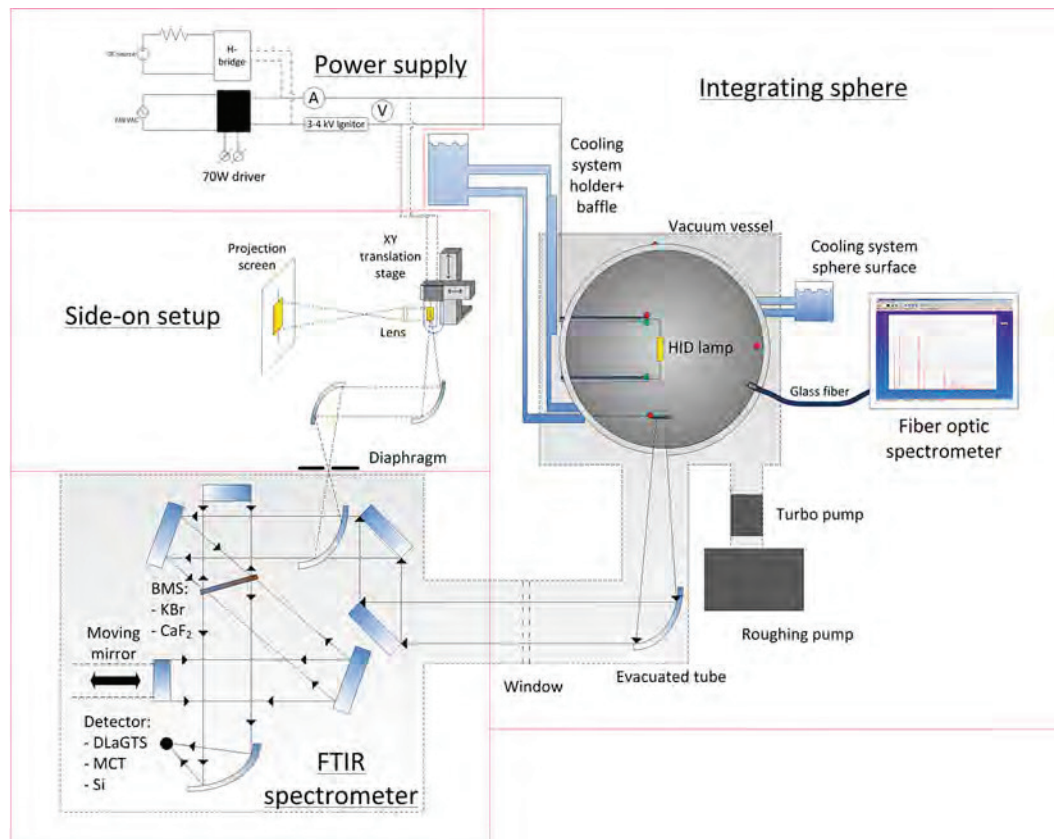


Figure 3.1 A schematic diagram of the experimental setup.

which passes through the vacuum vessel. A part of the vessel has a window, which is used to connect the optical path of one of the input ports of the FTIR spectrometer (Vertex 80v, Bruker) and the sphere. The pressure in the FTIR spectrometer is brought down to 5 mbar to reduce the absorption of radiation by air to negligible levels.

Insulation material is used to built a box around the FTIR spectrometer. Inside this box a heating system is placed which regulates the temperature of the air surrounding the FTIR. This will improve the stability of the FTIR temperature and makes it less sensitive to seasonal and day to night variations of the laboratory temperature.

The side-on setup consist of an XY stage with a lamp mounted onto it. It can be used to carry out lateral line-of-sight measurements of the lamp. The side-on setup is placed next to the other input port of the FTIR spectrometer. Since the fiber optic spectrometer is absent, parts of the blue and the UV spectrum cannot be measured in the side-on setup.

The lamps can be operated in two ways in both setups. The first option is to operate the lamps with a modified commercial Philips driver, with which the input power supplied to the lamp can be regulated up to 70 W. The driver delivers a square wave at 125 Hz (see section 1.2.2). However, these standard drivers have a limited

current of 1.5 A. This is sufficient for commercial lamps, but several custom-made lamps used for research purposes require more. To this purpose a DC source (XDC 600-10, Xantrex), which is capable of delivering up to 10 A, was combined with a specially manufactured H bridge. The H bridge is a DC-to-square-wave converter. The H bridge has the added advantage that the frequency of the square wave can be varied. A 50 Ω resistance is mounted in series with the H bridge. The changing of the polarity can cause short fluctuations in the lamp impedance. The resistance serves to prevent damage to the DC source by dampening the relative changes in impedance. The lamp voltage and current are measured with a power analyzer (Norma 3000, LEM).

An ignitor, which can deliver high-voltage peaks to ignite the lamp, is placed between the power source and the lamp. Commercial lamp have the ignitor built in the driver, but this ignitor was disabled in the experiments, since the voltage peaks can damage the power analyzer. The ignitor delivers high-voltage peaks when pressing a button. Once the lamp is ignited, cables can be connected to the power analyzer without the risk of damage to the power analyzer.

3.2 Spectrometers

In the experiments two different spectrometers were used: a fiber optic spectrometer and a Fourier transform spectrometer. The principal behind the fiber optic spectrometer is very straightforward. Radiation from the lamp is collected by a fiber optic. It is projected onto a grating, which splits and diffracts the radiation into beams traveling in different directions. This is then projected onto a CCD. The Fourier transform infrared (FTIR) spectrometer, however, requires a bit more explanation.

3.2.1 FTIR theory

An FTIR spectrometer uses a Michelson interferometer to create an interferogram. A schematic diagram of a Michelson interferometer can be seen in figure 3.2. The incoming radiation beam is split into two beams by a beam splitter. One of the beams travels a constant path length, while the other's path length is dependent on the position of a moving mirror. The two beams then recombine and are projected onto a detector, which measures the total signal strength. The strength of the signal will vary with the position of the moving mirror due to wave interference. A total scan over all positions of the moving mirror will produce an interferogram. The intensity as a function of the path length difference p and the wavenumber $\tilde{\nu} = \frac{1}{\lambda}$ is given by

$$I(p, \tilde{\nu}) = I(\tilde{\nu}) [1 - \cos(2\pi\tilde{\nu}p)], \quad (3.1)$$

where $I(\tilde{\nu})$ is the spectrum to be determined. The wavenumber-dependent intensity can therefore be determined by the Fourier inversion of $I(p)$.

In practice, FTIR spectroscopy is not as straightforward as the theory. During and after acquisition several operations were performed on the data before it is transformed. These will not be discussed in detail, but was described by Griffiths [25].

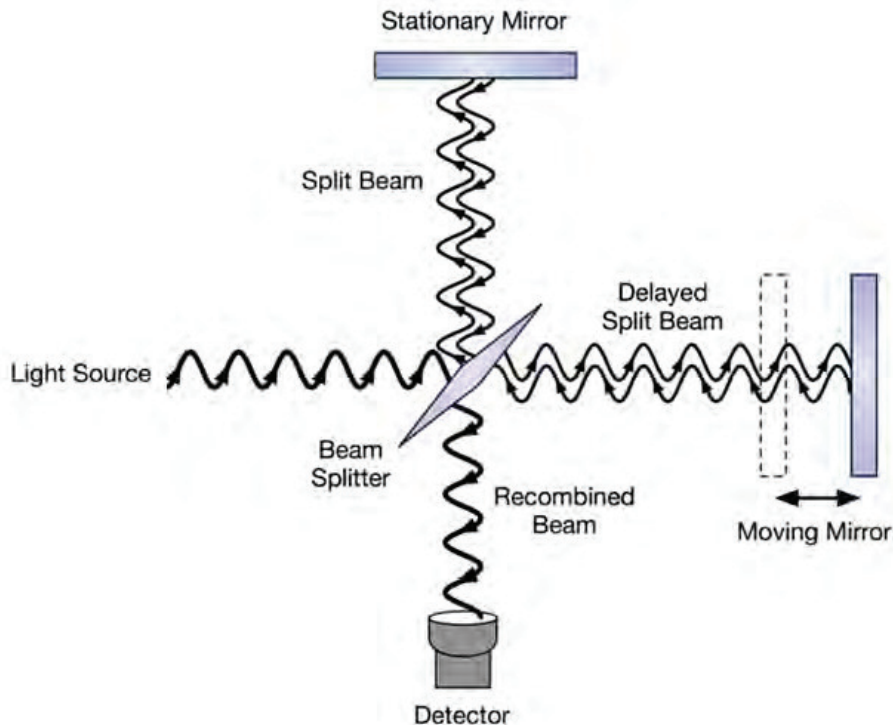


Figure 3.2 A schematic diagram of a Michelson interferometer.

3.2.2 Measurement procedures

Measurements over a spectral range of 300 nm - 20 μm (500 cm^{-1} - $33\,000\text{ cm}^{-1}$) required the combination of different beam splitters and detectors in the FTIR spectrometer. The FTIR spectrometer was used to determine the largest part of the spectral power distribution (420 nm - 20 μm). For the blue and ultraviolet measurements (300 nm - 420 nm) we used the Avantes spectrometer.

The infrared part (20 μm - 780 nm) and part of the visible part of the spectrum (420 nm - 780 nm) were measured with three different beam splitter/detector combinations. The infrared part was split into three parts: the far infrared (20 μm - 2.5 μm), mid infrared (2.5 μm - 1.18 μm) and the near infrared (1.18 μm - 780 nm) part of the spectrum. Each part was measured three times and then averaged. The results were combined into the total lamp spectrum.

Far infrared (20 μm - 2.5 μm) The measurements in the far infrared used a deuterated, L-alanine doped triglycine sulfate (DLaTGS) detector and a KBr beam splitter. The KBr beam splitter is commonly used for infrared transmission. The DLaTGS detector is an infrared-sensitive, pyroelectric detector. Its main component is a thin DLaTGS crystal. When infrared radiation is absorbed by the crystal it is converted into heat by an absorbing coating, which causes the temperature of crystal to increase by fractions of a degree centigrade. As a result of

the pyroelectric effect charges are generated in the crystal, which are a measure for the intensity of the signal. More specifically, the polarization of the dipoles in the crystal changes due to the temperature change. DLaTGS detectors have to be kept at a constant temperature to minimize response changes due to changes in room temperature. Therefore, the DLaTGS detector is cooled with a Peltier element, which keeps it at a constant temperature of 283 K. The detector is kept at such a low temperature because earlier experiments have shown that the strength of the signal profits from a large temperature difference between the detector and the integrating sphere.

The DLaTGS detector is a relatively slow detector, because the signal is inversely proportional to the data collection speed. For that reason the frequency of the mirror of the FTIR spectrometer was minimized when measuring with the DLaTGS detector.

Mid infrared (2.5 μm - 1.18 μm) For the mid infrared part of the spectrum an mercuric cadmium telluride (MCT) detector was used in combination with a CaF_2 beam splitter. The CaF_2 has an overlapping range with the KBr beam splitter, but it is a much more effective beam splitter for shorter wavelengths (the suitability of KBr worsens noticeably for wavelengths shorter than 1.25 μm). The MCT detector is a photoconductive detector, which means that its conductivity increases due to the absorption of electromagnetic radiation, i.e. a semiconductor. The intensity of the signal is determined by measuring the resistance of the MCT. It is most effective in the infrared part of the spectrum (1 μm - 10 μm). The MCT and DLaTGS detector work in overlapping parts of the spectrum. The DLaTGS detector is still preferred in the far infrared part of the spectrum, because the error of DLaTGS measurements in the far infrared was smaller than of the MCT measurement (see section 3.3.3.3).

Because the MCT detector has a relatively constant signal versus data collection speed, it works well with a high mirror frequency. It is possible to average the MCT signal over a relatively high number of scans.

Near infrared and visible (1.18 μm - 420 nm) A combination of the CaF_2 beam splitter and a silicon (Si) detector was used for measurements for the near infrared and part of the visible radiation in the spectrum. The silicon detector is a semiconductor detector like the MCT detector, with the exception that not the resistance, but the current is measured. The band gap of silicon is larger than that of MCT, which means that it works in a part of the spectrum with smaller wavelengths.

Blue and ultraviolet (420 nm - 300 nm) The blue and ultraviolet part of the spectrum were measured with the Avantes spectrometer, because of the signal loss of the FTIR spectrometer in that part of the spectrum. Because the Avantes spectrometer port is positioned at a different position than the FTIR spectrometer port, the range of the spectrum which was measured with the Avantes spectrometer was minimized.

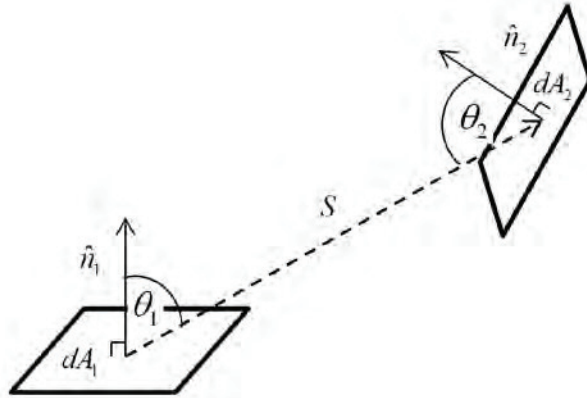


Figure 3.3 Two elements with a Lambertian surface, dA_1 and dA_2 , a distance S apart, exchange radiation. Their surface normals are \hat{n}_1 and \hat{n}_2 .

3.3 Integrating sphere

In this section the theory behind the integrating sphere is given to explain the design, and to show the limitations of our sphere. The FTIR and Avantes signal coming out of the sphere was calibrated for different detector/beam splitter combinations. The method and results of this calibration will be shown. Finally, an in-depth error analysis will be given for spectral power distribution determined with the integrating sphere.

3.3.1 Integrating sphere theory

As was explained in section 1.4, it is important to determine an energy balance in order to understand the lamp. A small amount of the input energy leaves the system in the form of conduction. Most of it however will be converted into radiation. The total radiant energy per unit time of the lamp, the radiant flux can be collected with an integrating sphere, which spatially integrates the radiant flux of the lamp. The sphere needs to be coated on the inside with a diffuse reflecting coating. Before explaining in detail how the sphere was incorporated in the experimental setup, it is important to understand the theory behind the sphere.

An ideal integrating sphere has a Lambertian surface, which means that the radiance L_e of such a surface to an observer is the same regardless of the observer's angle of view. Radiance is the flux density per unit solid angle and is defined by:

$$L_e = \frac{d^2\Phi_e}{dA d\Omega \cos \theta}, \quad (3.2)$$

with Φ_e the radiant flux, θ the angle between the surface normal and the specified

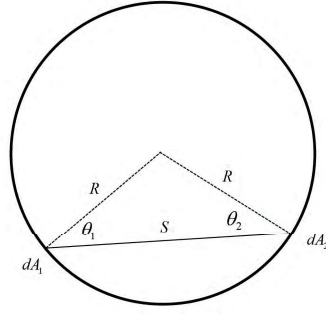


Figure 3.4 Two Lambertian surface elements inside an diffuse surface sphere.

direction, A the area of the surface and Ω the solid angle. Now consider the general case figure 3.3, with an emitting element 1 with surface area dA_1 and a receiving element 2 with surface area dA_2 at a distance S from element 1, and θ_1 and θ_2 the angle measured between the surfaces normals and S . A simple integration in spherical coordinates shows that

$$\Phi_1 = \pi L_e dA_1 \quad (3.3)$$

is the total radiant flux emitted by surface dA_1 .

Considering that the solid angle $d\Omega$ of element 2 from element 1 can be defined as $\frac{dA_2 \cos \theta_2}{S^2}$, the flux that arrives on surface dA_2 can easily be calculated:

$$\Phi_2 = L_e dA_1 \cos \theta_1 d\Omega = L_e dA_1 \cos \theta_1 \frac{dA_2 \cos \theta_2}{S^2}. \quad (3.4)$$

The fraction of the energie leaving dA_1 and arriving at dA_2 is known as the exchange factor $dF_{d_1-d_2}$ and is given by:

$$dF_{d_1-d_2} = \frac{\cos \theta_1 \cos \theta_2}{\pi S^2} dA_2. \quad (3.5)$$

Now consider the same situation, but with element 1 and 2 inside a diffuse surface sphere (see figure 3.4). Since the distance $S = 2R \cos \theta_1 = 2R \cos \theta_2$:

$$dF_{d_1-d_2} = \frac{dA_2}{4\pi R^2}. \quad (3.6)$$

This result is significant since it is independent of viewing angle and the distance between the areas. Therefore, the fraction of the flux received by dA_2 is the same for any radiating point on the sphere surface.

When equation 3.6 is integrated over dA_2 it becomes:

$$F_{1-2} = \frac{A_2}{4\pi R^2} = \frac{A_2}{A_s}, \quad (3.7)$$

where A_s is the surface of the sphere. So the fraction of the radiant flux received by A_2 scales directly with its surface [26].

Now that it has been established that an integrating sphere can effectively gather the complete radiant flux of an object, we review the case where the sphere is illuminated internally by an input flux Φ_i , e.g. by a lamp. From equation 3.2 the radiance can be derived:

$$L = \frac{\Phi_i \rho}{\pi A}, \quad (3.8)$$

where ρ is the reflectance of the surface. The radiance is an important engineering quantity, since it is used to predict the amount of flux that can be collected by an optical system that might view the illuminated surface.

For an integrating sphere, the radiance equation must consider both multiple surface reflections and losses through the port opening, which is needed to view the radiance resulting from input flux Φ_i . The port opening has a surface of A_p . Then the amount of flux incident on the entire sphere surface after the initial reflections is given by:

$$\Phi_s = \rho \Phi_i \frac{A_s - A_p}{A_p} = \Phi_i \rho (1 - f). \quad (3.9)$$

For convenience sake, a factor f is introduced, which describes the ratio between the port surface A_p and the surface of the sphere and port combined (A_s). Considering the fact that the flux emitted by the surface does not undergo one, but an infinite number of reflections, the total radiant flux emitted by the surface can be deduced:

$$\Phi_s = \Phi_i \sum_{i=1}^{\infty} \rho^i (1 - f)^i = \Phi_i \rho (1 - f) \sum_{i=0}^{\infty} \rho^i (1 - f)^i = \frac{\Phi_i \rho (1 - f)}{1 - \rho (1 - f)}. \quad (3.10)$$

This expression indicates that the total flux incident on the sphere surface is higher than the input flux due to multiple reflections inside the cavity. It follows that the sphere surface radiance is given by:

$$L_s = \frac{\Phi_i}{\pi A_s} \frac{\rho}{1 - \rho (1 - f)} = \frac{\Phi_i}{\pi A_s M}, \quad (3.11)$$

where M is a unitless quantity known as the sphere multiplier. It accounts for the increase in radiance due to multiple reflections. Equation 3.11 implies some basic design rules to increase the radiance of the sphere, such as increasing the reflectivity and f . Also notable is the fact that the radiance increases with decreasing sphere surface. However, these rules are deduced for a highly idealized case. An exact analysis of the distribution of radiance inside an actual integrating sphere would depend on the distribution of incident flux, the geometrical details of the actual sphere design, and the reflectance distribution function for the sphere coating. A sphere also contains objects mounted at a port opening or inside the integrating sphere, which also has a large influence on the sphere.

3.3.2 Integrating sphere design

Design parameters Figure 3.5 shows the different parts of the sphere used in our experiments. It is clear that the sphere used in the experiment differs from the idealized case. Different aspects of the sphere will shortly be described as well as its influence on the final results of the experiment.

Baffles Radiation exits the sphere via ports, so that it can be detected by the two spectrometers, which determine the spectral flux of the lamp. In front of these ports two baffles need to be placed in line with the source, because it is important that the detected radiation does not include direct lamp radiation nor a portion of the surface directly irradiated by the lamp. The baffles ensure that any radiation reaching the detectors is reflected at least twice. Both detectors are not focused on the surface of the sphere, but on the surface of the baffles. The introduction of foreign objects violates the principle of constant radiance of the surface as explained in section 3.3.1, especially since the detectors do not focus on the sphere surface, but on the baffles. It is therefore necessary to ensure that the radiation is properly mixed within the sphere.

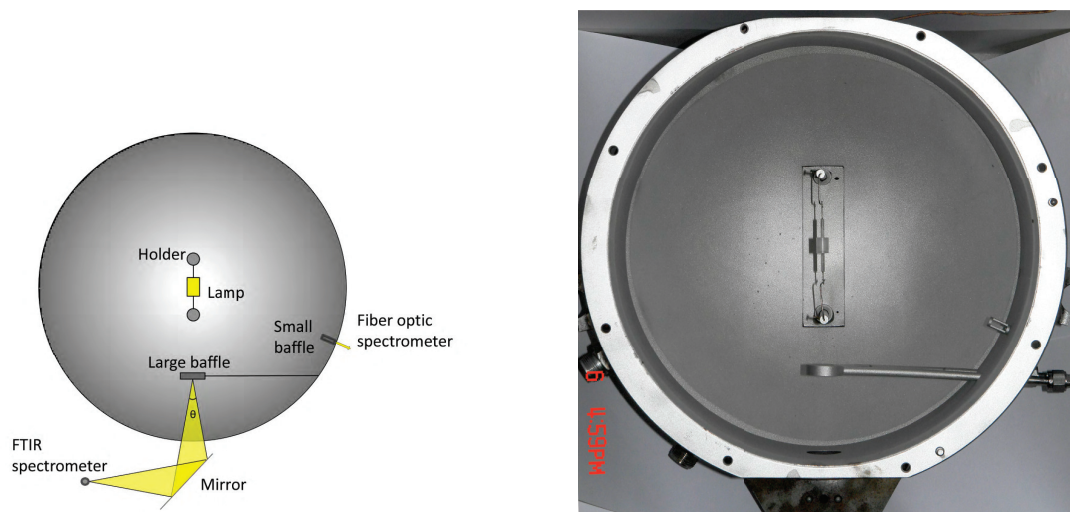


Figure 3.5 On the left is a schematic representation of the inside of the sphere. On the right there is a photo of the actual sphere, with a lamp in the holder.

Holder Beside the baffles, the holder is the other foreign object in the sphere. It can mount the lamp and contains the electrical wiring that provides input power to the lamp. In the experiment, the discharge tube and feedthroughs are removed from the outer bulb and metal casing. Two molybdenum wires are spotwelded to the feedthroughs to fit the lamp into the holder. The lamp in the holder can be seen in the right picture in figure 3.5. The holder is coated with the same material as the surface of the lamp to minimize absorption.

Shape and radius of the sphere The integrating sphere used in the experiments consists of three sections: a cylindrical and two concave sections. Therefore, it is not a perfect sphere. It has a diameter of 280 mm. Ideally, the sphere would have a small radius, since a small radius increases radiance of the surface (see equation 3.11). However, a smaller radius means that the disturbing influence of the foreign objects in the sphere becomes greater. Since there are always foreign objects present, a larger radius is preferred. The cylindrical part contains the large port leading to a FTIR spectrometer. One of the concave sections has a small port for the fiber optic spectrometer, while the other concave part has a slit in which the holder of the lamp fits.

Ports of the sphere As mentioned before, two ports lead to the different spectrometers of the setup. It was established that a higher value of f increase the surface radiance. However, both detectors measure the spectral power, so the radiant flux is a measure of the signal strength of the lamp. It can be established from equation 3.2 that the radiant flux on a detector Φ_d is given by:

$$\Phi_d = L_s A_d \int_{\Omega} \Omega_d(\theta) \cos \theta d\Omega = L_s A_d \pi \sin^2 \theta, \quad (3.12)$$

with L_s the radiance of the baffle (which is equated to the radiance of the sphere), A_d the focus area of the detector on the baffle, Ω_d the solid angle of the radiation that is projected on the detector and θ the maximum angle with respect to the normal of the large-baffle surface.

Coating of the sphere The coating of the sphere determines its reflectivity, the fraction of incident electromagnetic power that is reflected at an interface. The coating must be able to reflect radiation in a range from the deep infrared wavelength of 10 μm to ultraviolet radiation of 350 nm. A high reflectivity, 0.95 - 0.98, is required to reduce the spatial non-uniformity and increase the surface radiance. A drawback of higher reflectivity is the increased sensitivity to self-absorption by foreign objects. Lower reflectance, 0.8 - 0.9, is more stable in the long term, since for these reflectivities the sphere multiplier is less sensitive to small changes in the reflectivity. This sphere multiplier is determined by equation 3.11.

It is clear that the design parameters of the integrating sphere are co-dependent in the experimental setup and that the design rules as deduced in section 3.3.1 are not absolute. The dimensions of the sphere need to be carefully considered. The integrating sphere deviates from the ideal case: the introduction of foreign objects, the fact that the sphere shape is not perfectly rounded and the fact that the detectors are focused on the baffles and not on the sphere. This means that the big advantage of an integrating sphere, measuring a radiant flux independent of the angular and spatial distribution, will not be completely valid, i.e. the spectral radiance of the lamp will not be perfectly mixed within the sphere. It was therefore necessary to calibrate the detectors with a

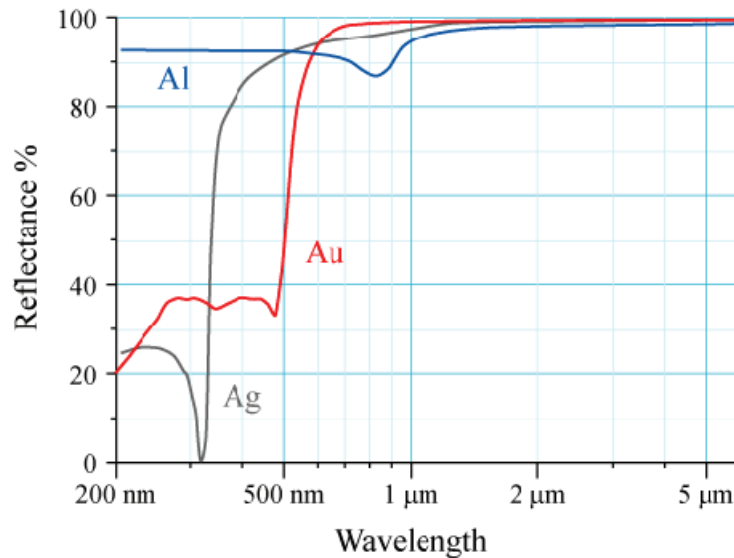


Figure 3.6 The reflectivity for several metals. Gold is an excellent reflector in the infrared range of the spectrum, but it absorbs a large part of the visual and ultraviolet radiation, which is a big drawback. Silver also seems to be a good candidate, since it also reflects a lot of the visible radiation, but its low reflectivity in the ultraviolet range disqualifies it from being a good candidate for the coating. In the end, aluminium was chosen. While it is at a disadvantage in the (near) infrared range compared to gold and silver, it is still able to reflect a lot of the blue and ultraviolet radiation.

source with an angular radiance distribution approximately equal that of the measured lamps.

Technical description As mentioned in the previous section, the sphere consists of a cylindrical and two concave parts made of copper. The cylindrical part has a width of 100 mm and a diameter of 280 mm. It contains a port with a diameter of 24 mm, in front of which a baffle with a diameter of 25 mm is placed, on which the FTIR spectrometer is focused. When the sphere is assembled, this port will be at the bottom. The cylindrical part also contains a smaller hole with a diameter of 6 mm. Its location within the sphere can be seen in figure 3.5. In this port a glass fiber cable is placed, which leads to a fiber optic spectrometer. One of the concave parts contains a wide slit, in which the lamp holder can be placed.

The inside of the sphere is coated with aluminium. Aluminium is an easily available material that has a reflectivity over 90 % in a range from ultraviolet to deep infrared radiation (see figure 3.6). The aluminium was coated onto the inner surface of the sphere. Prior to coating the surface was sandblasted to make the surface more diffusely reflecting.

Since the reflectivity of aluminium is less than 100 % in a wide range of the spectrum, part of radiation is absorbed by the sphere when it is in operation. This will heat up

the sphere. Measurements in the infrared require a setup with a stabilized temperature to properly correct for background radiation. To achieve this the sphere is made of a 4 mm thick wall of copper, which has the second highest thermal conductivity of all metals at room temperature. A series of square tubes is wound around the sphere. The tubes are square-shaped in order to maximize contact with the sphere. Water kept a constant temperature of 302 K is pumped through the tubes, which keeps the sphere at a constant temperature with a margin of 0.2 K. A separate system also cools the large baffle and the holder. The water of this system first flows through the large baffle, which is hollow. It then flows past the ends of the two holder legs, so it can absorb the power that is lost by the lamp via conductive heat transport to the legs. The temperature of the water of this system is the same as the water that cools the sphere, within a margin of 0.5 K.

The sphere contains four thermocouples (iSeries, Omega), which have an accuracy of 0.5 °C and a resolution of 0.1 °C. Two of the thermocouples are connected to the outer surface of the sphere and monitor the temperature of the sphere. One thermocouple is connected to one of the legs of the baffle sticking out of the sphere and monitors the temperature of the baffle. The last one is connected to the top of one of the legs. This one is used to determine the conductive power losses to the holder.

3.3.3 Integrating sphere calibration

3.3.3.1 Theory of the calibration

The calibration procedure of the integrating sphere has been described by Rijke et al. [16]. We will give a short summary.

The spectral power of a lamp is determined with a detector, which needs to be calibrated. To calibrate the detector a source with a known spectral power is placed in the sphere. The measured signal at the detector S_{source} is expressed as

$$S_{\text{source}}(\tilde{\nu}) = t_1(\tilde{\nu})\Phi_{\tilde{\nu}}^{\text{source}} + t_2(\tilde{\nu})\Phi_{\tilde{\nu}}^{\text{sphere}}(\tilde{\nu}, T_{\text{sphere}}) + t_3(\tilde{\nu})\Phi_{\tilde{\nu}}^{\text{other}}(\tilde{\nu}), \quad (3.13)$$

with $\Phi_{\tilde{\nu}}^{\text{source}}$ the spectral power emitted by the source, expressed as a function of the wavenumber $\tilde{\nu}$, $\Phi_{\tilde{\nu}}^{\text{sphere}}$ the spectral power emitted by the sphere and $\Phi_{\tilde{\nu}}^{\text{other}}$ the spectral power emitted by other objects outside the integrating sphere. The transfer function t_i take into account effect such as the integrating quality of the sphere, transmission of the windows and the sensitivity of the detector. The goal of the calibration procedure is to calculate t_1 , whose reciprocal is a calibration function for the measured signal of other lamps. Since the sphere temperature T_{sphere} is kept constant with the cooling system, the spectral flux of the sphere and other objects can be combined in a constant background signal S_{BG} , so that the transfer function t_1 can be expressed as

$$t_1(\tilde{\nu}) = \frac{S_{\text{source}}(\tilde{\nu}) - S_{\text{BG}}(\tilde{\nu})}{\Phi_{\tilde{\nu}}^{\text{source}}(\tilde{\nu})}. \quad (3.14)$$

3.3.3.2 Calibration sources

In the experiments the FTIR spectrometer was used in a spectral range between 20 μm (500 cm^{-1}) and 400 nm ($25\,000\text{ cm}^{-1}$). The FTIR spectrometer can measure larger wavenumbers, but in our experiments its range is limited by the detectors within the spectrometer. The fiber optic spectrometer can measure in a spectral between 190 nm and 750 nm. We used a platinum strip as the source to calibrate the infrared part of the spectrum, while a halogen lamp with known spectral flux was used for the visible and ultraviolet part of the spectrum. The calibration sources were used to create different calibration functions k_i for a different detector/beam splitter combinations.

Platinum strip A platinum strip was used to calibrate the setup as low as the lower wavelength limit of our detector (20 μm) up to the start of the visible part of the electromagnetic spectrum (780 nm). Again, the calibration of the integrating sphere with a platinum strip has been described extensively by Rijke et al. [16], so a summary will be given here.

We sent a current through the strip, which is an ohmic resistor. As a consequence the strip heated up and emitted thermal radiation. Platinum was used as the strip material because of its stability and reproducibility. It is not sensitive to corrosion and has a relatively high resistivity and a low thermal conductivity, which aids in heating up the strip, thus increasing the radiant flux of the strip. The strip has a length of 101 mm, a width of 5.0 mm and a thickness of 22.7 μm . The calibration function for a detector calibrated with the platinum strip is expressed as follows:

$$k_{\text{Pt}} = \frac{1}{t_{1,\text{Pt}}} = \frac{\Phi_{\nu}^{\text{Pt}}}{S_{\text{Pt}} - S_{\text{BG}}}. \quad (3.15)$$

The spectral power of the strip was determined with a one-dimensional model. First the temperature profile was determined, which was then used to calculate the spectral power. The results of the simulation can be seen in figure 3.7.

These profiles were calculated as follows: in the model the strip is divided into 250 control volumes for which the power balance is solved. The power in each control volume is balanced between ohmic heating due to dissipation, heat conduction from and to neighboring volumes and radiative losses. The ohmic heating is calculated using Joule's first law, the conducted heat is calculated using Fourier's law of thermal conduction and the radiant flux is calculated using Stefan-Boltzmann's law. These laws are all coupled to the temperature via the electrical conductivity, thermal conductivity and emissivity of platinum, respectively, so solving this model results in a temperature profile. The validity of this calculated profile was proven by comparing the calculated ohmic dissipation with the measured input power for four different currents, which agreed within 0.6 % for all currents.

The second part of the model calculates the spectral power of the platinum strip from the calculated temperature profile by integrating equation 3.2 over the surface and

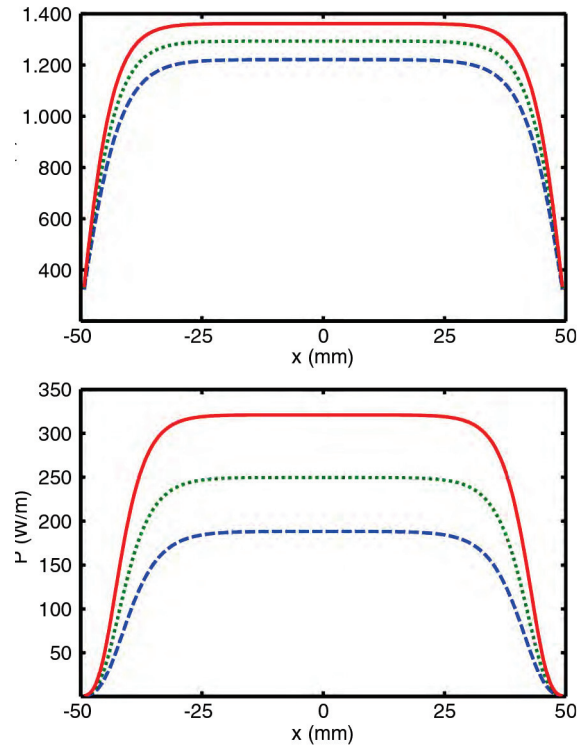


Figure 3.7 The temperature profile (top) of the strip and the resulting radiant flux profile (bottom) for different currents (from top to bottom 10 A, 9 A and 8 A).

over the solid angle of a hemisphere:

$$\Phi_{\bar{\nu}}^{\text{Pt}} = \pi A_{\text{cv}} \epsilon_{\bar{\nu}}(T) B_{\bar{\nu}}(T), \quad (3.16)$$

with A_{cv} the surface area of each control volume, $\epsilon_{\bar{\nu}}$ the spectral effective emissivity of platinum and $B_{\bar{\nu}}$ the spectral radiance of a black body. The validity of this profile was tested by integrating the spectral power over the the complete spectrum for each control volume and dividing it by the radiant flux resulting from Stefan-Boltzmann's law. This results in a scale factor called the effective emissivity. This factor is the ratio of the total amount of radiant flux exiting a black body to that which is predicted by Plancks law. This ideally would be 1, but this can deviate because of uncertainties in the value of the spectral emissivity or the geometry or surface roughness of the platinum strip. The final spectral power of each control volume is therefore multiplied by the effective emissivity.

During the project the sphere and detectors were recalibrated bimonthly by measuring the radiant flux of the strip for three different currents (9 A, 9.5 A and 10 A). Small changes in impedance —the impedance of the strip would go up by $\sim 1\%$ per six months— were corrected by adjusting the thickness of the strip in the model. These corrections were also $\sim 1\%$ (or $\sim 0.2\ \mu\text{m}$), and therefore within the margin of error of the

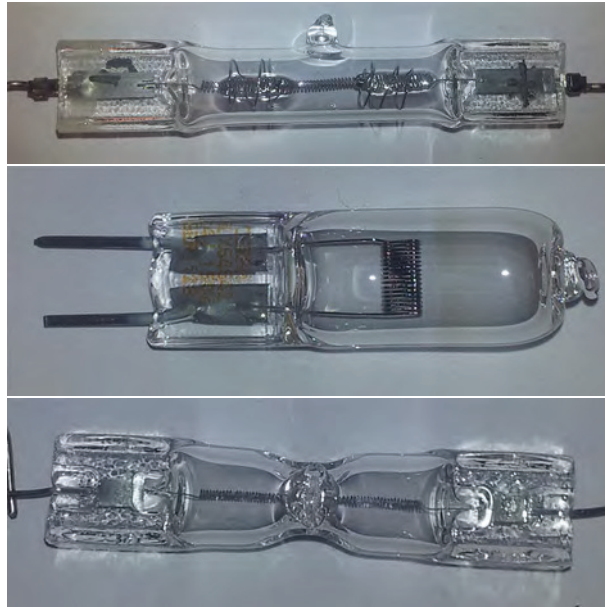


Figure 3.8 Several lamps used for testing. From top to bottom: a 200 W double-ended lamp, a 150 W, 24 V, single-ended lamp and 70 W double-ended lamp. The photos are not to scale. The single-ended lamp is considerably smaller than the others.

measurement of the thickness. The calculated ohmic dissipation depends on the resistance of the strip, which in turn depends on the value for the thickness of the strip in the model. The thickness which resulted in the lowest maximum deviation from the measured input power at the three different currents is inserted into the model calculating the spectral power.

Halogen lamp The visible part of the spectrum was calibrated with a halogen lamp. In order to find a suitable calibration lamp, several lamps were measured (see figure 3.8). It was important to find a calibration lamp whose angular distribution of the radiation matched that of an CMH lamp. Two types of halogen lamps were chosen: longitudinal double-ended halogen lamps, and short, single-ended halogen lamps. Although much larger than an CMH lamp, it shares the basic longitudinal shape as well as radial symmetry with an CMH lamp. Its main drawback, especially in relation to the size of the sphere, is that these lamps are much larger than an CMH lamp. The other type of halogen lamp that we measured was a single-ended halogen lamp. It is the opposite of the double-ended lamp. The filament is folded in the shape of a thin square. Therefore, it does not radiate cylindrically symmetrical. It does have the advantage that its filament is much smaller than that of the double-ended lamps.

The spectral powers of these lamps were first measured in an integrating sphere at Philips, along with a 70 W CMH lamp. After that, the halogen lamps were measured in our integrating sphere. These measurements were combined with the measured data at

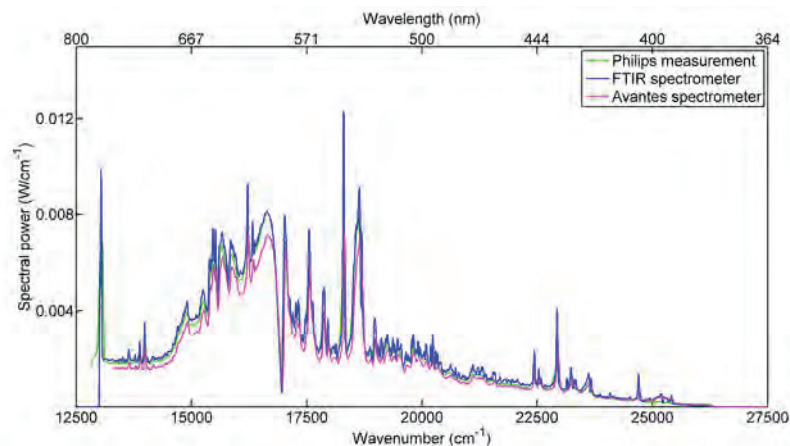


Figure 3.9 A comparison between the spectral power of the 70 W CMH lamp determined at Philips, and the spectral power determined with the integrating sphere. The calibration functions of the 150 W single-ended halogen lamp were used for both the FTIR and the Avantes spectrometer.

Philips into calibration functions for the FTIR spectrometer and the Avantes spectrometer. This was followed by the measurement of the 70 W CMH lamp in the integrating sphere. Its spectral power was then calculated with calibration functions of the different halogen lamps. These spectra were compared to the CMH lamp spectrum measured at Philips to see which spectrum matched the Philips spectrum the most. The lamp whose calibration function gave the best results was chosen as the calibration lamp.

The lamp that gave the best results was the 150 W single-ended halogen lamp (Osram, Halostar, 150 W, 24 V, center of figure 3.8). Figure 3.9 shows the measurement of the 70 W CMH lamp calibrated with this lamp for the Avantes and the FTIR spectrometer along with the spectral power of the HID lamp measured at Philips. The spectrum measured with the FTIR spectrometer matches the Philips spectrum very closely, although the lower resolution of the Philips spectrum mitigates the features of the spectrum. The spectrum of the Avantes detector matches the Philips spectrum in the blue part of the spectrum, but deviates up to 15 % in the red part of the spectrum. This is caused by the way the lamp is positioned within the sphere. The main area of the filament is pointed towards the baffle of the Avantes spectrometer and it is therefore likely that its light is not properly mixed before it reaches the Avantes detector. Deviations from the Philips spectrum are unwanted, because as a result the signal of the halogen lamp is overestimated, resulting in a lower calibration function than expected. All consequent measurements calibrated with that function will thenceforth be underestimations in the range where these deviations are found. This can be seen in figure 3.9.

However, in the area that the Avantes spectrometer is used, beyond $24\,000\text{ cm}^{-1}$ ($<420\text{ nm}$), the measurement of the Avantes matches the Philips measurement. Therefore, the 150 W single-ended halogen was judged a suitable calibration source. The

reason it works well is its small size and the fact that it is a high-power, low-voltage lamp. A low voltage increases the stability over time of the halogen lamp. The high current also leads to a high filament temperature which, combined with the large power, emits a whiter spectrum.

Other lamps that were tested had a significantly lower signal strength. This still made them acceptable calibration sources in the red part of the spectrum, but their calibration functions lead to overestimations up to 20 % in the blue part.

UV Calibration The halogen lamps measured at Philips were only measured in the visible part of the spectrum (380 nm - 780 nm). This meant that there was no calibration data available for the ultraviolet part of the spectrum. As a solution we extrapolated the Philips data of the halogen lamp into the ultraviolet. The power of the calibration lamp $\Phi_{\lambda}^{\text{lamp}}$ in the ultraviolet was calculated as follows:

$$\Phi_{\lambda}^{\text{lamp}} = \mathcal{T}_{\lambda} \epsilon_{\lambda}(T) C B_{\lambda}(T), \quad (3.17)$$

where \mathcal{T}_{λ} is the wavelength-dependent transmittance of the lamp, ϵ_{λ} is the effective emissivity of the tungsten filament, B_{λ} is the spectral power distribution of a black body, and C is a scaling constant, which contains, for instance, the surface of the filament. The exact dimensions of the filament were not exactly known, so C is a normalization factor used to match the spectrum of the model to the spectrum of the Philips measurement. The effective emissivity of a filament folded in a square shape was not known, so for the emissivity the results of De Vos, who measured the emissivity for a tungsten ribbon, were taken [27]. The emissivity had to be extrapolated from this data, since De Vos only measured the emissivity of tungsten up to 2800 K, and halogen lamps have filament temperatures around 3200 K [28].

Finally, there is the issue of the transmittance of the outer bulb. The outer bulb of the lamp was made of quartz. Manufacturers of quartz products list the transmittance of quartz at ~ 93 % for quartz with a thickness of 10 mm for wavelengths larger than 300 nm [29]. The thickness of the bulb wall was estimated at 1 mm, which results in a transmittance of 99.3 %.

First, the burn temperature of the filament was determined by matching the calculated spectral power curve to the measurement. This turned out to be 3250 K. After that the calculated curve for wavelengths smaller than 380 nm was ‘glued’ to the actual measurement (see figure 3.10). This ensured that there would be no discontinuities in the calibration function.

3.3.3.3 Integrating sphere error analysis

A thorough analysis of the errors in the spectral measurements was made for each used detector/beam splitter combination. The platinum strip and halogen lamp that were used to calibrate their respective parts of the spectrum, were also used to determine the error in the measurements. The error was determined by measuring both the halogen

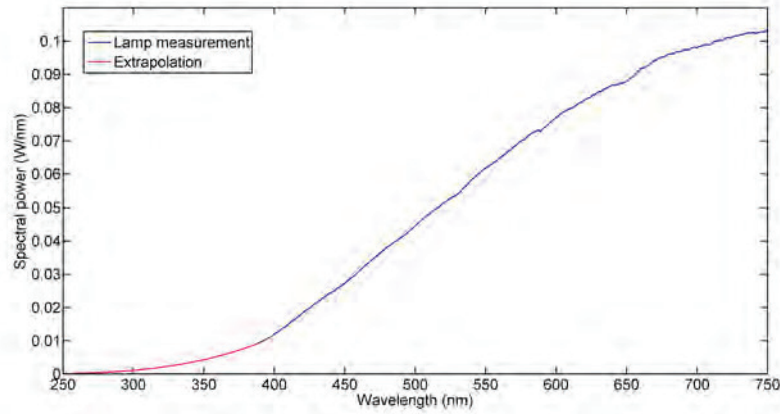


Figure 3.10 The figure shows the extrapolation of the calibration into the UV part of the spectrum.

lamp and the platinum strip on four different days, and determining the difference between these measurements. The results can be seen in figures 3.11-3.12. Three different errors could be quantitatively deduced: the reproducibility of the signal (*measurement error*), the error in the calibration function (*calibration error*) and the error due to the background radiation and heating of the sphere and lamp holder (*temperature error*). Added, they give the wavelength-dependent error of the spectral power measurements.

Measurement error The *measurement error* is defined as the error in the reproducibility of the signal. This can be determined by measuring same source with the same settings at different points in time. Each source was measured three times in a row. These three measurements were then averaged to give S_{λ}^i , in line with the measurement procedure that was used throughout the project. This was repeated several days in a row. The error ϵ_{ν} for n sets of measurements, n being the number of days, was then determined with the following formula:

$$\epsilon_{\nu} = \frac{\max(S_{\nu}^1, \dots, S_{\nu}^n) - \min(S_{\nu}^1, \dots, S_{\nu}^n)}{2\overline{S_{\nu}^i}}. \quad (3.18)$$

To determine the error curves seen in figures 3.11-3.12, a (smoothed) line was drawn through the local maxima of ϵ_{ν} , because it was a very noisy function.

Overall, all detector/beam splitter combinations show a base error between 0.2 and 1.5 %, depending on the wavenumber. Part of this error is noise, which is part of every measurement. This is the only error that completely disappears in the energy balance. The second part of the base error is the difference in sets of measurements acquired on different days, which can be ascribed to variations in the spectrometers and/or detectors. Several factors can negatively influence the reproducibility of the measurements. For instance, between sets of measurements the beam splitter has often been changed, which

3.3 Integrating sphere

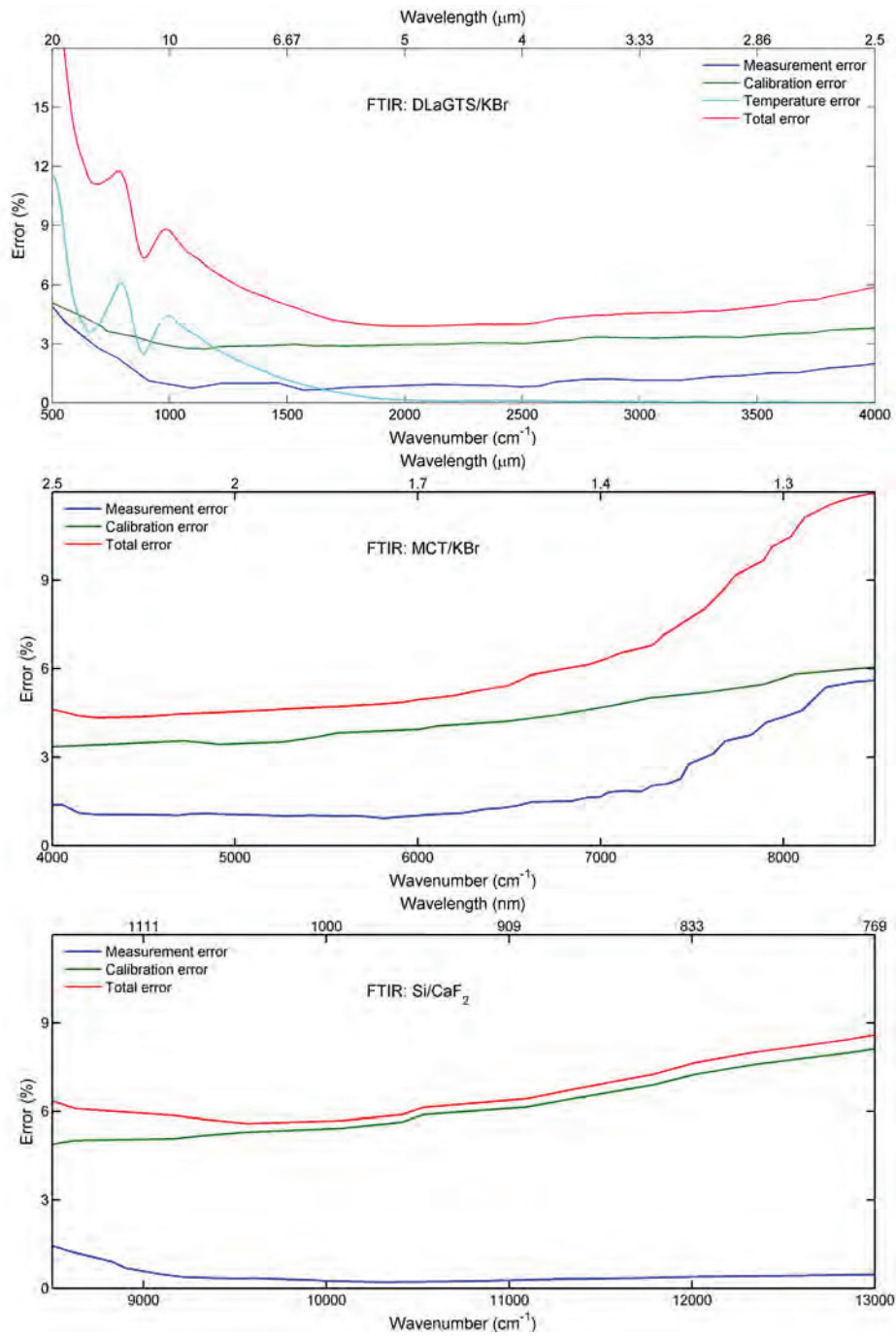


Figure 3.11 The error in the spectral power distribution for the different parts of the spectrum that were calibrated with the platinum strip.

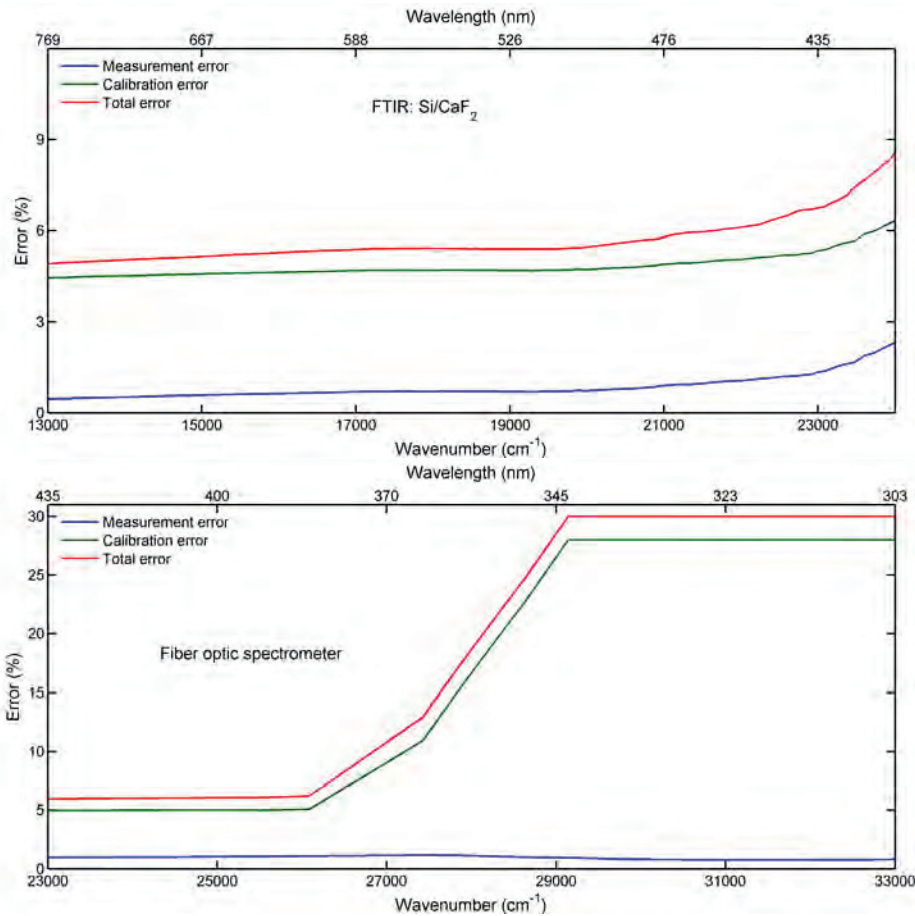


Figure 3.12 The error in the spectral power distribution for the different parts of the spectrum that were calibrated with the halogen lamp.

can cause very slight differences in the alignment of the FTIR spectrometer. Also, both the MCT and the DLaGTS detector are very sensitive to small temperature differences.

Increases in the measurement error, such as for the DLaTGS/KBr detector/beam splitter combination for wavenumbers below 1000 cm^{-1} , for the MCT/KBr detector/beam splitter combination for wavenumbers larger than 7000 cm^{-1} and for the CaF_2/Si detector/beam splitter combination for wavenumbers larger than $23\,000\text{ cm}^{-1}$, can be attributed to the loss in sensitivity of the detectors.

For wavenumbers below 1000 cm^{-1} and above $23\,000\text{ cm}^{-1}$ the use of the FTIR is limited because of the beam splitters and detectors. This is also the case in the range around 8000 cm^{-1} . At 7500 cm^{-1} the sensitivity of the MCT detector starts to rapidly decrease. However, the silicon detector will not detect much below 8500 cm^{-1} , which is directly related to the width of the band gap. Therefore, there is an ‘error spike’ in that range of the spectrum.

Because the measurement error is essentially a random error, it influences the absolute values of the spectral power curve. To acquire the energy balance of the lamps, the spectral power curves are integrated. This means that the noise does not influence the energy balance and should be subtracted from the error due to the noise. However, because this contribution is relatively small, it is not shown separately in figures 3.11-3.12.

Calibration error The *calibration error* of a curve is caused by the error in the calibration function. The first part of the calibration error is directly linked to the measurement error. This is because the calibration curves are determined from sets of measurements of the halogen lamp and of the platinum curve, and these sets are, of course, subject to measurement errors. Therefore, the measurement error becomes a systematic error once a set of measurements is used to determine the calibration function. The extent of this error is mitigated by the fact that each point in the calibration function is smoothed by the moving average method.

The second part of the calibration error comes from the uncertainty in the spectral power of the calibration source. This is straightforward for the halogen lamp. The lamp is measured in an integrating sphere at Philips, which has an error of 4 % over the complete range of the measurement, i.e. the visible part of the spectrum. The error in the spectral power of the platinum strip is less straightforward, because its spectral power is calculated from a model. Errors in the calculated spectral power can be the result of uncertainties in the spectral emissivity of the strip or uncertainties in the temperature. The total uncertainty in the spectral power of platinum strip can be found by taking the derivative equation 3.16 with respect to its variables:

$$\frac{d\Phi_{\tilde{\nu}}^{\text{Pt}}}{\Phi_{\tilde{\nu}}^{\text{Pt}}} = \frac{dB_{\tilde{\nu}}}{B_{\tilde{\nu}}} + \frac{d\varepsilon_{\tilde{\nu}}}{\varepsilon_{\tilde{\nu}}} \simeq \frac{100hc\tilde{\nu}}{k_B T} \frac{dT}{T} + \frac{d\varepsilon_{\tilde{\nu}}}{\varepsilon_{\tilde{\nu}}} \quad (3.19)$$

It is a combination of a temperature error, which is proportional to the wavenumber, plus the error in the values for the emissivity. The temperature error increases linearly from around 0.5 % at 1000 cm^{-1} to 5 % at $13\,000\text{ cm}^{-1}$.

The emissivity of the platinum by interpolating platinum emissivity measurements from Rolling [30], who measured the emissivity of platinum strips with different roughnesses at different temperatures. Roughness measurements showed a small deviation between the roughness of the strips measured by Rolling and the strip used in the experiments. There was also a difference between the temperature of the strips of Rolling and the experiment. Difference in emissivity is most pronounced in the far infrared part of the spectrum. To quantify this difference, an error was estimated at 2 % at 1000 cm^{-1} . This error decreases linearly to a constant value at 0.5 % at 4000 cm^{-1} and higher wavenumbers.

Temperature error The source inside the sphere is not the only object that radiated in the far-infrared part of the spectrum. The holder, baffle and sphere radiate as well. Most of this radiation could be compensated by a background measurement. However, some of the radiation emitted by the source is absorbed by the holder, the baffle and the sphere. As a consequence they warm up, even though they are actively cooled. This leads to a systematic error in the measurements. Thermocouple measurements showed that the temperature of the sphere and the holder increases when the source is turned on. The temperature of the baffle remained stable. Therefore, it is assumed that absorption by the baffle does not influence the measurements.

The temperature of the sphere consistently rose with 0.2 K when measuring a 70 W HID lamp and with 0.1 K when measuring the platinum strip. The influence of the rise in temperature of the sphere by a lamp was partly compensated by the heating up of the sphere by the platinum strip, because the extra signal of the sphere leads to an overestimation of the signal. As a result the calibration function will be lower. The influence of the heating of the sphere could be obtained by measuring the radiation of the sphere at different temperatures.

The sphere, which is normally cooled at $29 \text{ }^\circ\text{C}$ (see section 3.3.2), was cooled at four different temperatures between $25 \text{ }^\circ\text{C}$ and $32 \text{ }^\circ\text{C}$ and its spectrum was measured. The change in signal as a function of the temperature was then fitted linearly over the width of the spectrum to get a , which is the change in signal per Kelvin, as a function of the wavenumber. The systematic error due to the heating of the sphere is then given by:

$$\epsilon_{\text{sphere}} = 1 - \left| \frac{1 - \frac{0.2a(\tilde{\nu})}{S_{\text{lamp}} - S_{\text{BG}}}}{1 - \frac{0.1a(\tilde{\nu})}{S_{\text{Pt}} - S_{\text{BG}}}} \right| \quad (3.20)$$

with S_{lamp} the signal of the lamp, S_{Pt} the signal of the platinum strip and S_{BG} the background signal of the sphere when the source is turned off. Since $A_{\text{source}} \ll A_{\text{sphere}}$, it is assumed that the background signal for the lamp and the platinum strip is equal.

The influence of the holder temperature could also be calculated. The temperature at the top of legs of the lamp holder was measured with a thermocouple, while the ends of the legs were cooled. A linear temperature profile over the legs was assumed. The spectral power of the holder when a source i was operating in the integrating sphere is

given by:

$$\Phi_{\bar{\nu}}^{\text{holder},i} = 4\pi^2 R_{\text{leg}} \varepsilon_{\text{leg}} \int_0^\ell B_{\bar{\nu}}(T_i(x)) dx, \quad (3.21)$$

with R_{leg} the radius of the leg, ε_{leg} the emissivity of the leg, ℓ the length of the leg, $B_{\bar{\nu}}$ the black body spectral radiance of the leg and T_i the temperature profile over the leg as a result of source i . The relative error of the holder can then be expressed as:

$$\epsilon_{\text{holder}} = 1 - \left| \frac{1 + \frac{\Phi_{\bar{\nu}}^{\text{holder,lamp}}}{k(S_{\text{lamp}} - S_{\text{BG}})}}{1 + \frac{\Phi_{\bar{\nu}}^{\text{holder,Pt}}}{k(S_{\text{Pt}} - S_{\text{BG}})}} \right|, \quad (3.22)$$

with k the calibration function and S the detector signals.

We used equations 3.20 and 3.22 to calculate the temperature error for a typical lamp measurement. This can be seen in figure 3.13. Of course, this error depends heavily on which lamp is measured and the emissivity of the holder surface. The exact emissivity of sandblasted aluminium is not known. Touloukian et al. [31] showed that the emissivity of aluminium roughened by carbide paper is around 0.25 in the far-infrared region of the spectrum, while polished aluminium has an emissivity near 0. We therefore estimated the emissivity of the holder legs at 0.15.

Figure 3.13 shows that the temperature error is largest for the holder, and that its influence increases for lower wavenumbers. It is evident from equation 3.22 that the holder error approaches zero signal strengths of the platinum strip and the lamp are approximately equal. Overall, the lamp signal strength is much larger than the platinum strip signal strength, but it experiences a dip in the spectral range between 500 and 1000 cm^{-1} . This is because the emissivity of the burner wall material, PCA, also has a dip in that part of the spectrum. This reduces the error in that part of the spectrum. Unless mentioned otherwise, all lamps that were measured during this project have PCA burners.

The sphere's thermal radiation creates only a small error in the spectral range between 500 cm^{-1} and 1000 cm^{-1} . Its influence is almost non-existent for wavenumbers higher than 1000 cm^{-1} . The shape of the sphere's error curve can be explained by equation 3.20, which showed that sphere error is minimized when the lamp signal strength is twice the signal strength of the platinum strip.

Other lamps showed similar error curves. Of course the unknown emissivity of the holder legs is a limiting factor, as is the limited resolution of the thermocouples on the sphere, but it is evident that the cooling of the sphere and holder is important for the reliability of the measurements in the far infrared. Due to our extensive effort of temperature stabilization of the entire setup these errors are limited.

Other errors Several other factors that add uncertainty to the measurements cannot be determined quantitatively. As explained before, it is necessary that the radiation of

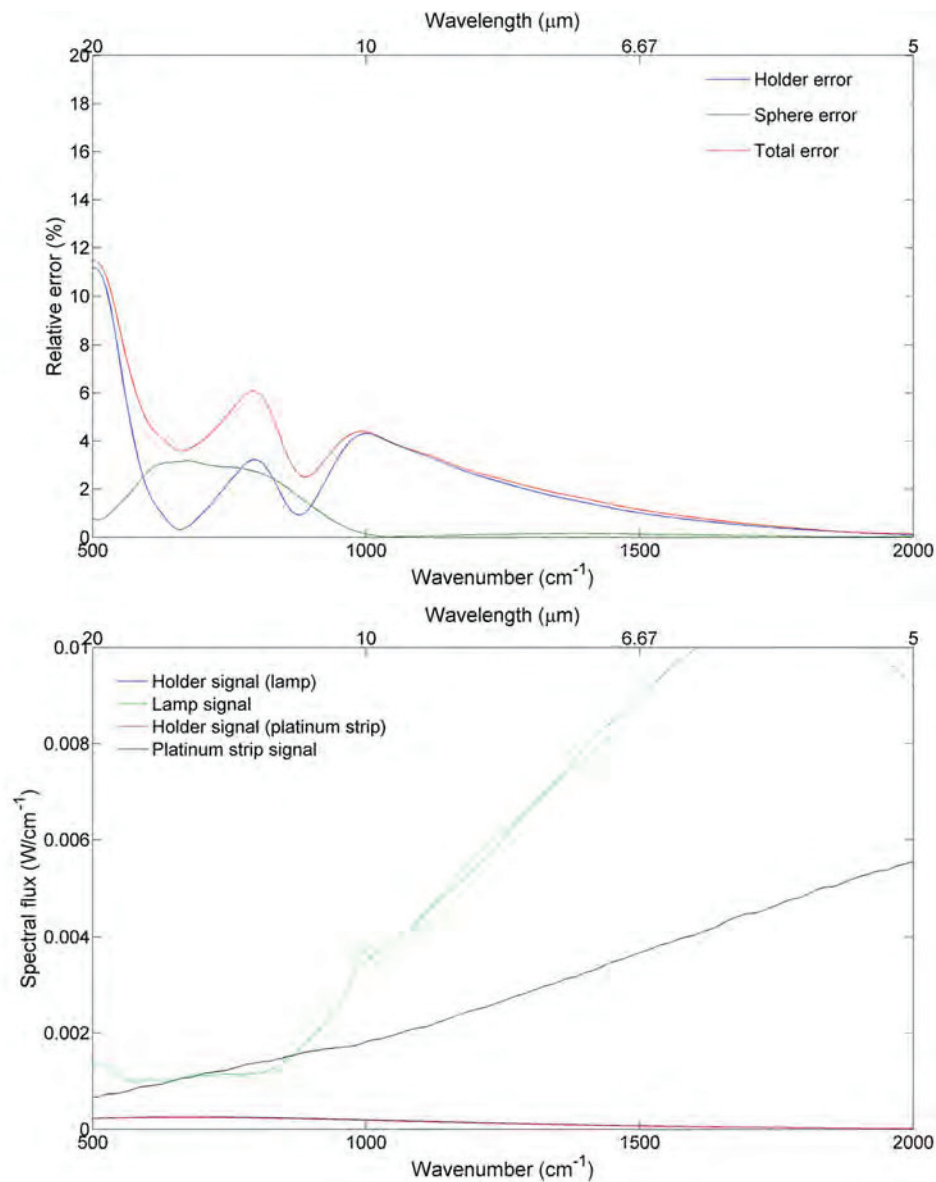


Figure 3.13 The relative error of a typical HID lamp measurement. The dip in the spectral range between 500 and 1000 cm^{-1} is caused by the lower transmittance of the PCA burner in this range. This limits the error of the radiative output.

the source is mixed properly over the area of the integrating sphere in order to perform comparable measurements on different sources. The baffles in the sphere are vital in this respect, because they ensure that the radiation reaching the detector will be reflected at least twice. Unfortunately, the introduction of foreign objects in the sphere destroys the sphere's symmetry. As a consequence the final result of the measurements will depend on the angular distribution of radiation of the source. This can be mitigated by choosing a calibration source with a similar angular distribution of radiation to that of the HID lamps. This problem can never be fully fixed, though, because of variations in the angular distribution of radiation of the HID lamps themselves. Because the reflectance of aluminium is larger in the infrared part than in the visible part of the spectrum, it is to be expected that the error is larger in the latter part of the spectrum.

The spectral powers of the lamps measured during this project were also measured at Philips in a spectral range between 380 nm and 780 nm. It would be possible to compare these with our results, but the conditions at Philips (atmospheric pressure, burner still in outer bulb) were different than the condition of our experiments (high vacuum, burner removed from outer bulb). The spectral powers could therefore not be compared vis-à-vis. Therefore, the integrating quality of the sphere could best be determined by the energy balance of the lamps. The total power output of a lamp can be calculated by adding the total radiant flux of the lamp, determined from the spectrum, to the power lost through the holder legs via conduction.

The reproducibility of the experimental setup has been determined with very stable source, but because most HID lamps are experimental, their long-term behavior is not known. This is also true for commercial lamps to a lesser extent, but this does create some uncertainty in the measurements. Some of the lamps measured suffered from blackening, which means that they do not have a fully developed halogen cycle and that their electrodes are too hot. Therefore, tungsten was slowly deposited on the burner wall, decreasing its transmittance and increasing its absorbance. The result is less plasma radiation and more thermal radiation.

Finally, there is an error in the calculation of the conduction losses. The legs of the lamp holder are also capable of absorbing part of the lamp radiation, while the calculation of the conduction only includes a conduction term. The emitted power of the holder is very small compared to the calculated power for the conduction losses, but its absorbance accounts for an overestimation of the conduction losses. It is assumed that the luminance of the sphere holder is equal to that of the sphere. In this case the fraction of the power that is absorbed by the holder legs will be determined by the fraction between surface area of the holder legs and the surface area of the sphere. This results in an absorbed power by the holder of 0.06 W. This leads to an error in the conduction losses of 1.5 % - 3 %, depending on the lamp, or 0.07 % of the total input power.

3.4 Side-on setup

3.4.1 Side-on setup design

Technical description The side-on setup was used to measure the spectral radiance of HID lamps by focusing the FTIR locally inside the lamp. A schematic diagram of the side-on setup can be seen in figure 3.14. While most of the lamps measured in the experiments had burner made of PCA (see section 1.2), several lamps had a YAG (yttrium-aluminium-garnet) burner. The advantage of YAG is that it is transparent, in contrast to PCA, which is only translucent. Transparent lamps could be measured in the side-on setup, i.e. to measure the laterally-dependent spectral radiance of the lamp. With the help of Abel's inversion it is then possible to deduce the radiance as a function of the radius.

A setup of the side-on experiment can be seen in figure 3.1. In order to perform the side-on measurements, a lamp was placed on an XY linear translation stage. The discharge tube was kept inside the outer bulb. The FTIR spectrometer was focused on the lamp with the help of two parabolic mirrors. This was necessary, since the focal point of the spectrometer is only 27 mm from its exit window. Parabolic mirrors were used instead of lenses, because of and the limited size of the table and because parabolic mirrors have no chromatic aberrations. As it can be seen in the figure, a diaphragm was placed in the focal point of the spectrometer in order to reduce the lamp signal and prevent overexposure as well as unwanted signal from entering the spectrometer. The diaphragm was a 0.3 mm \times 10.0 mm slit. The slit acts as a collimator, so it makes it possible to carry out line-of-sight measurements. In front of the slit another slit of 0.8 mm was placed horizontally, effectively creating a (rectangular) pinhole of 0.3 mm \times 0.8 mm. In order to check whether the discharge is axially homogenous, an image of the lamp was projected on a white screen, by placing a lens next to the lamp. All lateral measurements were performed with the spectrometer focused in the axial center of the lamp. The XY translation stage had a range of 50 mm in both directions, with an accuracy of 0.1 mm. The spatial resolution of the side-on measurement is mostly determined by the size of the slit. A slit of 0.3 mm was chosen, since it allowed for a reasonable accuracy without causing the signal to lose too much strength.

Side-on measurements Several side-on measurements were carried out on lamps with a transparent YAG burner. The lamps were laterally scanned with a step size of 0.1 mm. The goal of these experiments was to obtain the temperature in the lamps and to determine where the atomic and molecular radiation in the lamp originated.

It was vital that the measurements were performed relatively rapidly, because the discharge arc in the lamps was not perfectly stable. This had a lot of influence on the final measurements. The measurements were performed with the MCT/CaF₂ detector/beam splitter combination, because most optically thin atomic lines for indium can be found in the range of 4000 cm⁻¹ - 8000 cm⁻¹. The measurements were combined into a set of lateral measurements for different wavenumbers. Since the lamp is no longer in an integrating sphere, it is not possible to measure its spectral power. Rather, the lamp's

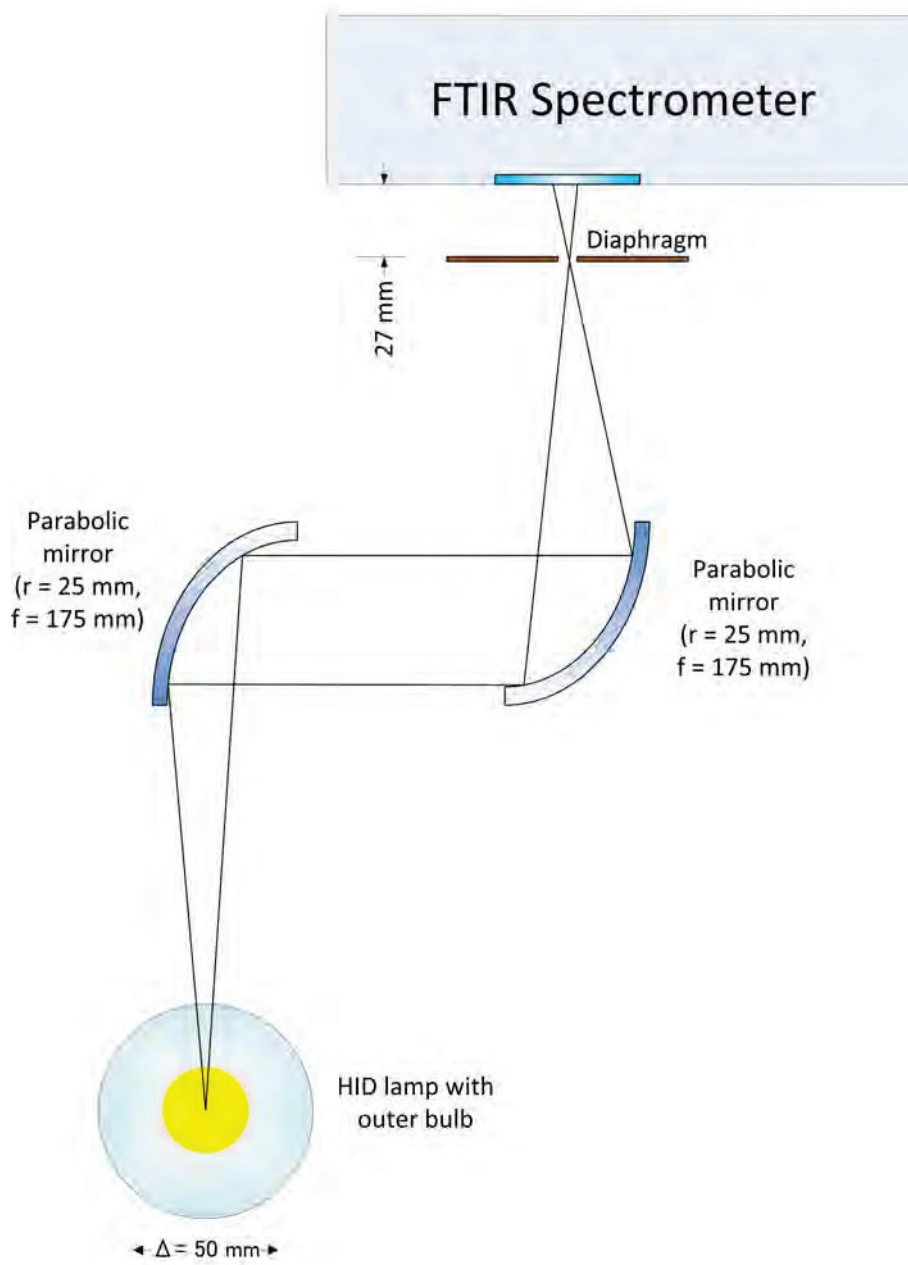


Figure 3.14 Schematic diagram of the side-on setup.

spectral radiance is measured. From these measurements a wavelength-dependent radial profile can be determined with the help of the Abel inversion (see section 2.8).

3.4.2 Calibration of the side-on setup

For measurements on the side-on setup only the FTIR spectrometer could be employed. A tungsten ribbon lamp was used to calibrate the side-on setup. The tungsten ribbon lamp consisted of a small tungsten ribbon of 19 mm \times 2 mm inside an outer bulb, which had a flat window towards the spectrometer. It had a special shape to keep the temperature over the surface of the ribbon as constant as possible. The FTIR spectrometer was focused on the center of the tungsten ribbon. The current through the ribbon was set at 10.24 A, which corresponded to a tungsten ribbon radiating at 2200 K, according the calibration sheet of the lamp. Unfortunately, this calibration was done over forty years ago. A more recent calibration was not available, however, so the final calibration functions of the side-on setup were, most likely, an underestimation, since it is to be expected that the resistance of the tungsten ribbon will have increased over time.

3.4.3 Side-on setup error analysis

Lateral measurements in this setup are presented with some problems. Abel theory assumes an infinitely thin, completely straight line of sight. This can present additional problem in experiments, where the plasma is contained within a 1 mm thick ceramic discharge tube, which deflects the line of sight. Secondly, the line of sight is not infinitely thin. Rather, it is a beam of light, whose rays are not completely parallel. This can be seen in figure 3.14.

First, the problem with the burner wall will be addressed. Figure 3.15 shows that for all lateral measurement for $y = 0$ the line of sight will be deflected due to refraction at the discharge tube. The unperturbed line of sight can be defined by y , which is the shortest distance of the line to the center of the lamp. The line, however, is deflected when it enters the tube. The shortest distance of the center the lamp to this line is defined by h . If $y = h$ the lateral scan remains valid, under the condition that the discharge in the lamp is radially symmetrical. Under this assumption we can define y and h using Schnell's law:

$$\begin{aligned} y &= R_2 \sin \alpha_1 = \frac{n_{\text{tube}}}{n_{\text{out}}} R_2 \sin \alpha_2, \\ h &= R_1 \sin \beta_2 = \frac{n_{\text{tube}}}{n_{\text{in}}} R_1 \sin \beta. \end{aligned} \tag{3.23}$$

A very useful relation is found in two different expressions for the length d , namely

$$d = R_1 \sin \beta = R_2 \sin \alpha_2, \tag{3.24}$$

such that

$$h = \frac{n_{\text{out}}}{n_{\text{in}}} y. \tag{3.25}$$

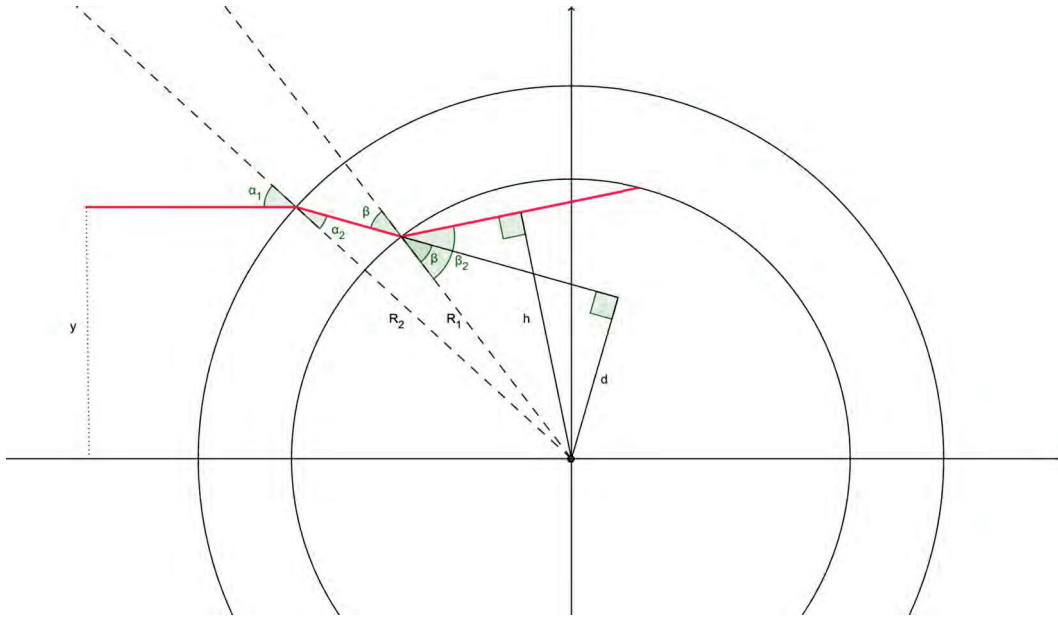


Figure 3.15 A schematic overview of a line-of-sight measurement on a cylindrical object with a wall. It can be proven that $y = h$ and that therefore, under the condition that the discharge is radially symmetrical, a lateral profile $L(y)$ remains valid.

So if the refractive indices inside and outside the tube are approximately equal, the lateral measurements will remain valid.

Secondly, the problem of a non-infinitely small, non-parallel line of sight will be addressed. The slit in the setup acts as a collimator, but it does have a finite width, so part of the radiation leaves the lamp at an angle, therefore influencing the measurement.

A schematic drawing of the setup is shown in figure 3.16, which is an extension of figure 3.14. The mirror is focused on the central axis of the lamp. However, the diaphragm does not have an infinitely small slit. Therefore the mirror is focused in a spot. The radiation that leaves the lamp and is projected on the mirror has the form of a beam. The fact that this beam is not straight, but diverging, requires a closer look. After all, a lateral scan requires that the lines of sight of the measurements are parallel. To investigate this problem, we imagine the beam that falls onto the mirror to be a collection of infinitely small rays.

It was just shown that the presence of a burner wall does not influence the final measurement. However, as can be seen in the figure, the outer lines of the beam have a different distance to the center of the lamp than the center rays. It can be deduced that these rays represent a line integral of an infinitely thin ray that transverses the lamp at a distance $h = \frac{y_0}{\cos \theta}$, with θ the angle of the ray with respect to the center of the line of sight. Actually, for the top ray in the figure the real value for h is $\frac{y_0 + r_{\text{spot}}}{\cos \theta}$, but this is compensated by a ray that enters at a similar angle with a value of $h = \frac{y_0 - r_{\text{spot}}}{\cos \theta}$, under the condition that the line integral function $L(y)$ is approximately linear in the domain

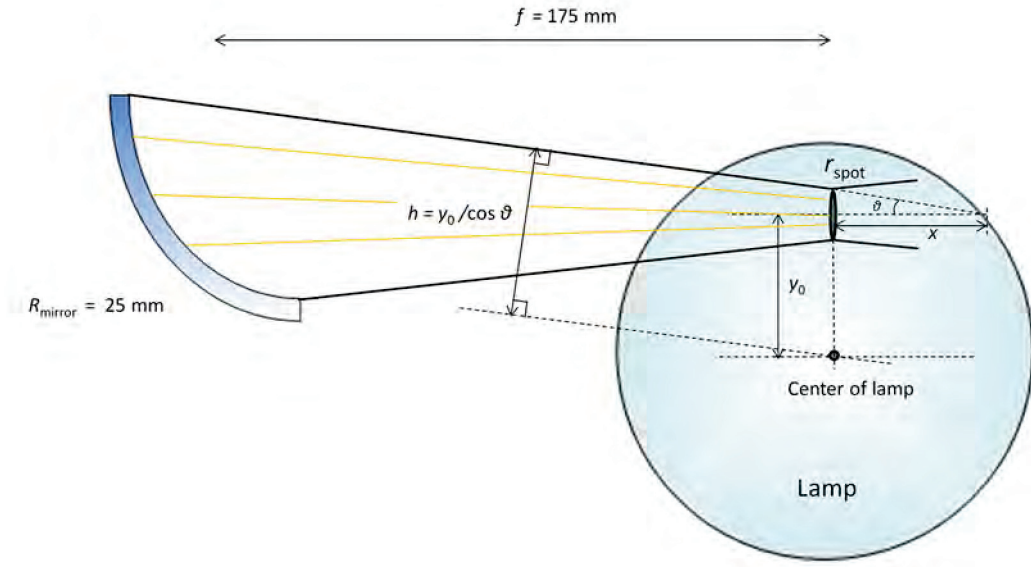


Figure 3.16 A schematic drawing of the side-on measurement. It can be shown that the error is sufficiently small to validate the lateral measurements.

$[y_0 - r_{\text{spot}}, y_0 + r_{\text{spot}}]$. The two rays then average out to $L(y_0)$. Since r_{spot} is relatively small, and since we expect $L(y)$ to be a monotonic function, this simplification is valid. So, as long as the beam is symmetrical around y_0 , this discrepancy can be ignored.

It has been determined that the radius of the mirror R_{mirror} is 25 mm, f is 175 mm and r_{spot} is 0.2 mm (see figure 3.16). From these values it can be determined that outer rays of the beam of sight leave the lamp at an angle $\theta_{\text{max}} = 8^\circ = 0.14$ rad. Normally, this angle is only valid for the center point of r_{spot} , while the points at the edge of r_{spot} have a slightly different radiating angle θ . However, because $r_{\text{spot}} \ll R_{\text{mirror}}$, this difference is very small. It is therefore assumed that the radiating angle is 8° for all points on r_{spot} . This eliminates the dependency on y from the error $\epsilon_{\text{side-on}}$. This can therefore easily be determined at:

$$\epsilon_{\text{side-on}} = \frac{1}{2\theta_{\text{max}}} \int_{-\theta_{\text{max}}}^{\theta_{\text{max}}} \frac{d\theta}{\cos \theta} = 1.0033. \quad (3.26)$$

To clarify this number, a measurement at y is actually a measurement at $1.0033y$. This is such a small difference that measurement errors due to the shape of the beam can safely be ignored.

It has just been established that the setup can be used to carry out side-on experiments on HID lamps, but a closer look should be given to other errors of the side-on setup. Since it is not possible to measure the far-infrared part of the spectrum with the side-on setup, it is evident that it does not suffer any of the temperature errors. Of course, the measurement and calibration error, determined in section 3.3.3.3 for the integrating sphere measurements, still apply. Side-on measurements do suffer a lot more from

arc instability than integrated sphere measurements. During operation, the discharge of the lamp can be subject to small changes, especially in the case of experimental lamps. For instance, many lamps have a cathode that operates in spot mode, which means that the arc forms a bright spot some distance from the emitter (as opposed to the diffuse mode of the cathode, which is self-explanatory). The location can shift during operation, causing the arc to become unstable. This has little influence on the radiant flux of the lamp, but is a big problem when carrying out side-on measurements, since these measurements demand that the arc is very stable. However, more specific errors in the side-on measurements are more comprehensible in combination with the actual measurements and will therefore be saved for the discussion of the results.

Chapter 4

Experimental procedures

4.1 Determining the energy balance

The energy balance could be determined by mounting the lamp in the integrating sphere. Its spectral power was then determined with the spectrometers and the conduction losses with the thermocouple attached to one of the holder legs. From the integrating-sphere measurements the plasma radiation, non-radiative losses and conduction losses could be determined. The electrode losses were determined from simulations.

4.1.1 Plasma radiation

The plasma radiation power was determined from the integrating sphere measurements. The complete spectral power distribution of a lamp was measured between 250 nm and 20 μm . The power of the ultraviolet radiation was determined by integrating this spectral power distribution between 250 nm and 380 nm, the power of the visible radiation by integrating the spectrum between 380 nm and 780 nm and the total infrared radiation by integrating the spectrum between 20 μm and 780 nm. The infrared plasma radiation had to be separated from the thermal radiation of the burner. For this we used switch-off measurements.

4.1.2 Thermal radiation

In the previous chapter we showed that it is possible to measure the complete spectral power of a lamp. In order to create a deeper understanding of the discharge it is preferable that the infrared radiation emitted by the lamp is split up into plasma radiation and thermal radiation. The latter can be used to calculate the non-radiative losses in the energy balance (see figure 1.4). Knowing power lost to the non-radiative processes is also necessary to utilize the Elenbaas theory (see section 2.7). To this end, a so-called switch-off measurement was carried out on each lamp.

A switch-off measurement was executed as follows: when the lamp was switched off, a signal was sent to the FTIR spectrometer. This started a series of low-resolution spectral measurements with the MCT detector in rapid succession. These measurements

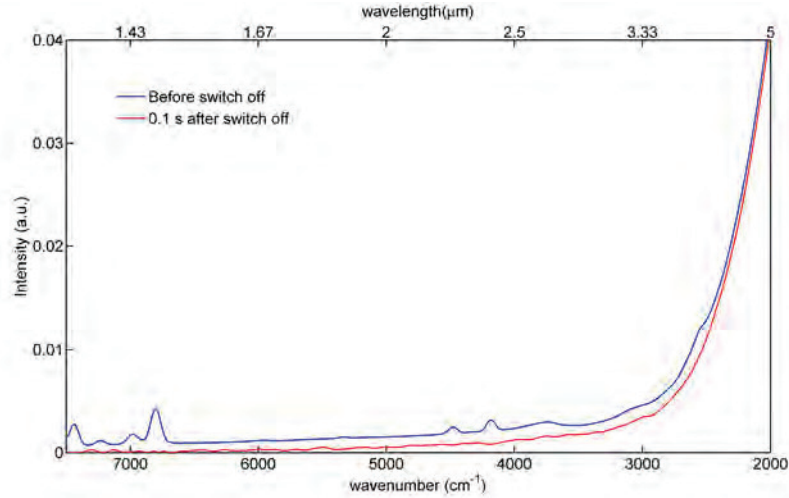


Figure 4.1 The figure shows two spectra: one spectrum that was measured while the lamp was still on and one that was measured 0.13 s after the lamp was switched off. The difference between the two curves is radiation that can be attributed to the plasma. The rest of the radiation is thermal radiation of the burner wall and of the electrode.

were combined to show the (exponential) decay of the intensity as a function of time between 1000 cm^{-1} and 7500 cm^{-1} . Figure 4.1 shows the (low-resolution) spectrum of the lamp while it is still on and the first switch-off measurement, after 0.13 s. Integrating the first switch-off measurements give the total power lost to thermal radiation. However, both the thermal radiation from the discharge tube and the thermal radiation from the electrodes was detected in these measurements. It is necessary to separate them to create Elenbaas plots. Fortunately, the electrode radiation decays much faster than the burner radiation, since the electrodes are in direct contact with the actively cooled legs of the lamp holder. It is therefore possible to determine the burner radiation by extrapolating the decaying intensity curve from $t = 3\text{ s}$, the moment we are certain that the contribution of the electrodes to the switch-off spectrum is negligible, back to $t = 0\text{ s}$, the moment of switch-off. This can be seen in figure 4.2.

The result of the extrapolation is then integrated over the wavelength. This results the thermal burner radiation power in the spectrum in the spectral range below $20\text{ }\mu\text{m}$.

The detector rapidly loses sensitivity for wavelengths larger than $20\text{ }\mu\text{m}$. To make sure that all lamp output was included in the energy balance, this part of the spectrum had to be simulated. For wavelengths larger than $20\text{ }\mu\text{m}$ the discharge wall was assumed to be a black-body radiator at 1200 K with 100% emissivity. In the fashion of the UV calibration (see page 41) the black-body curve was ‘glued’ to the measured curve in order to get a full spectrum. The extrapolated part of the thermal radiative power curve typically contained $\sim 0.5\text{ W}$. Uncertainties in the emissivity of the discharge tube and the wall temperature would therefore not significantly alter the energy balance. The integrated power of this curve $P_{\text{far-IR}}$ was then added to the thermal radiative power

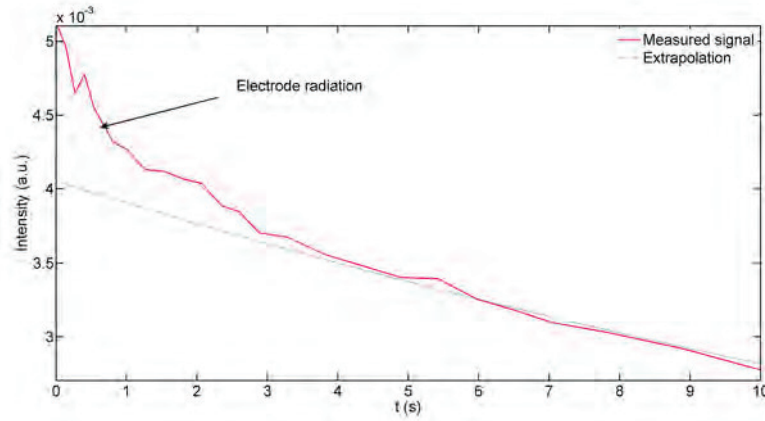


Figure 4.2 The electrode radiation is separated from the thermal radiation of the discharge tube by extrapolation the decaying intensity curve from $t = 3$ s back to $t = 0$ s.

to get the power of the burner wall radiation P_{therm} . $P_{\text{far-IR}}$ is also added to the total radiant flux of the lamp spectrum to get P_{spectrum} , the total radiative output of the lamp. The total power of the lamp's radiation P_{rad} can then be calculated as follows:

$$P_{\text{rad}} = P_{\text{spectrum}} - P_{\text{therm}}. \quad (4.1)$$

4.1.3 Conduction losses via holder legs

The lamp loses part of its energy via conduction through the legs of the holder. These conduction losses consist of conduction losses of the electrodes $P_{\text{el,cond}}$ and conduction losses of the burner $P_{\text{bur,cond}}$.

The losses by conduction can be calculated by assuming a constant temperature gradient over each leg of the holder. The bottom end of each leg is kept at a constant temperature T_{sphere} by the temperature regulation system of the holder and the baffle, which is set at the same temperature as the sphere. The temperature T_{top} is also measured at the top end of one of the legs with a thermocouple. From these temperatures the conduction losses P_{cond} can be calculated:

$$P_{\text{cond}} = -2\lambda_{\text{Cu}} \frac{T_{\text{top}} - T_{\text{sphere}}}{\ell} \pi R_{\text{leg}}^2, \quad (4.2)$$

with λ_{Cu} the thermal conductivity of copper, ℓ the length and R_{leg} the radius of one of the legs. P_{cond} is made up of conduction losses of the electrode and conduction losses to the electrode at the point of contact between the burner wall and the electrodes.

4.1.4 Electrode losses

To use the Elenbaas theory it is necessary to determine the electrode losses. The electrode losses were therefore simulated with the Eldes 2 program, a program developed

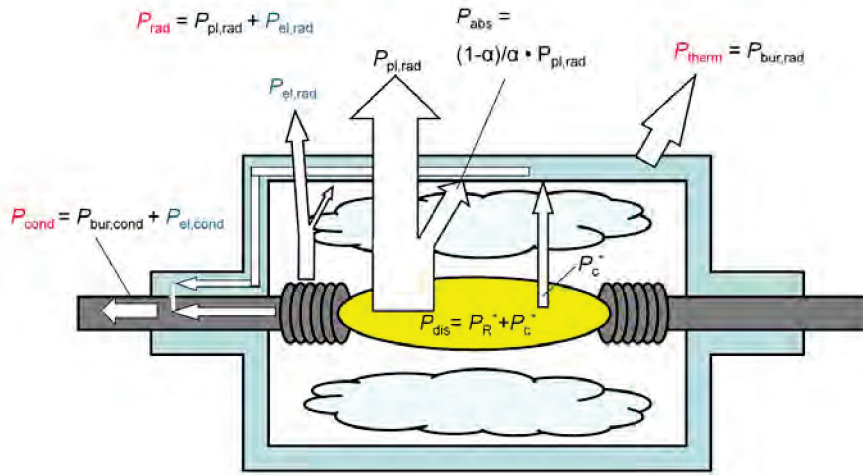


Figure 4.3 The power flow in a discharge lamps. The powers in red can be determined by measurements, while the powers in blue are simulated. With these it is possible to calculate the powers in black.

at Philips Lighting to simulate electrode behavior in HID lamps. A detailed description of the Eldes 2 program was written by Nijdam [32]. In the Eldes 2 program, the heat balance equations are solved numerically for a two-dimensional, rotational symmetric electrode body that is divided into small elements. The shape of the electrodes can be seen in figure 4.4. The program simulated both the radiative and the conductive power output of the electrodes. It requires many input parameters, such as the cathode model, anode fall, the presence of gas phase emitter effects, anode and cathode spot size, et cetera. However, a technological description of electrode theory is beyond the scope of this project. It suffices to say that the result of the simulations depended on three discharge parameters: the arc current, the arc field strength and the pressure of the major ion source in the discharge. During experiments the current was measured, as well as the voltage, which can be used to determine the field strength. The major ion source in most lamps was indium. The same pressure determined in the channel model was used in these calculations.

4.2 Determining Elenbaas plots

By measuring the thermal radiative power it is possible to create Elenbaas plots, which are useful to determine conductive losses and absorption by the mantle. An overview of the different power flows in the system is seen in figure 4.3.

According to the theory (see section 2.7, Elenbaas plots depends input power of the lamp $P_{\text{la}} = U_{\text{la}} I_{\text{la}}$ and P_{el} the power lost to the electrodes, via both radiative and conductive losses. The electrode losses are quite significant, as can be seen in figure 4.4.



Figure 4.4 The figure shows the electrodes of a lamp shortly after extinction. Switch-off measurements will group electrode radiation with the thermal radiation of the burner wall. This is separated by extrapolating the switch-off data.

The power lost to the electrodes P_{el} is simulated (see next section).

However, rather than using $P_{\text{la}} - P_{\text{el}}$ on the x -axis of the Elenbaas plot, we used $P_{\text{out}} - P_{\text{el}}$, with P_{out} defined as

$$P_{\text{out}} = P_{\text{rad}} + P_{\text{therm}} + P_{\text{cond}}. \quad (4.3)$$

A mismatch between the input power P_{la} and the output power P_{out} , e.g. due to an error in P_{rad} , would have serious influences on the Elenbaas plot, making both α and P_{C}^* unreliable. This influence will be mitigated if the output power is taken, because P_{out} will contain the same error.

Each lamp was measured at three different powers (usually 50 W, 60 W and 70 W). An Elenbaas plot is created by plotting $P_{\text{plasma,rad}}$ against $P_{\text{out}} - P_{\text{el}}$. This results in the values for α and P_{C}^* . These serve as a measure for the absorption by the mantle and the conduction losses in the core. They are also used to determine the accuracy of the simulation of the electrode losses or the Elenbaas plot itself, because the non-radiative losses P_{NR} (see also equation 2.36) can be determined in two ways:

$$P_{\text{NR}} = P_{\text{C}}^* + P_{\text{abs}} = P_{\text{therm}} + P_{\text{bur,cond}} \quad (4.4)$$

4.3 Determining discharge parameters

Core temperature and neutral particle density Most of the lamps that we measured contain indium, which has some strongly radiating atomic lines. These lines are listed in table 4.1, along with their properties. The transition coefficients were calculated by Safronova et al. [33]. These lines can be used to create a Boltzmann plot, from which a core temperature and an atomic indium density can be determined, provided that the lines are optically thin. Due to the higher temperature in the core and the fact that most InI molecules will be dissociated in the core, it is reasonable to assume that most atomic line radiation will be generated there and that the calculated temperature and densities are an estimate for conditions in the core. These values can be used with the

λ (nm)	$\tilde{\nu}$ (cm^{-1})	E_u (eV)	$A_{ul}(10^7 \text{ s}^{-1})$	g_u
1291.61	7742.29	3.982	1.57	4
1343.36	7444.03	3.945	1.43	2
1382.83	7231.55	4.841	0.735	4
1432.02	6983.13	4.848	0.912	6
1467.27	6815.36	4.923	1.32	6
1472.31	6792.05	4.923	1.42	8
2229.71	4484.88	4.501	0.348	2
2388.57	4186.61	4.501	0.636	2

Table 4.1 The properties of the indium spectral lines that were used in the analysis of the discharge. The transition coefficients were the result of calculations by Safronova et al. on atomic indium transitions [33].

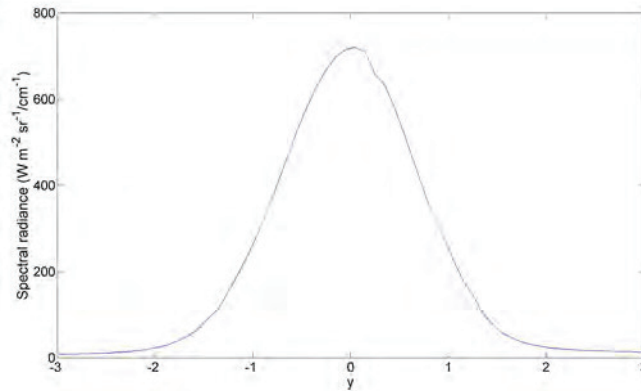


Figure 4.5 The figure shows the spectral radiance at 6983 cm^{-1} (1432 nm). Although the discharge tube has an inner diameter of 7 mm , it is clear that almost all radiation is emitted from a core with a width of approximately 4 mm .

channel model (see section 2.6) to calculate the electron density, partial atomic indium pressure and effective radius.

To test whether these lines were optically thin, a lamp with 1.5 mg InI filling was mounted into the side-on setup. This way it was possible to measure a line of sight through the center of the lamp. Radiation along this line of sight has to traverse the largest distance through the lamp and is therefore best for detecting self-absorption of the line. Besides detecting self-absorbance, a lateral scan can also be used to confirm the concept of a radiating core with a non-radiating mantle.

The spectral radiance distribution was measured in the YAG lamp as a function lateral position. The spectral radiance at 6983 cm^{-1} (1382 nm) as a function of lateral position can be seen in figure 4.5. The YAG discharge tube has an inner diameter of 7 mm , but almost all radiation is produced in a core of approximately 4 mm . This confirms the model of Elenbaas in which he splits the HID lamp into a radiating core

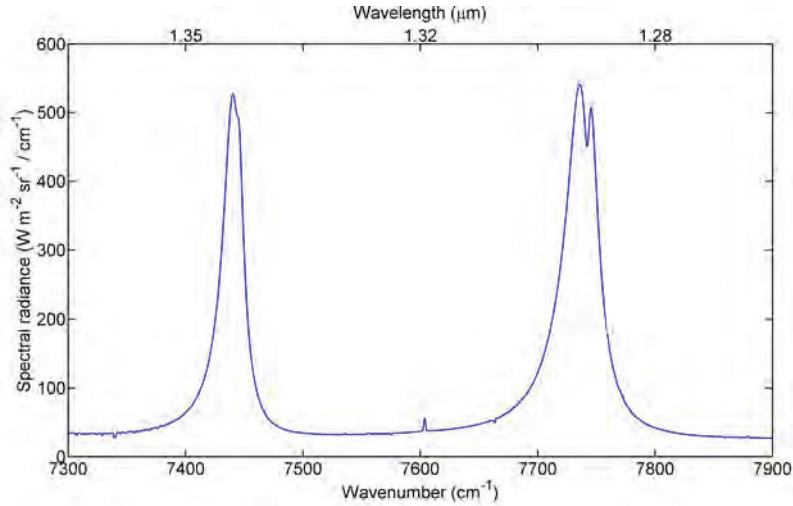


Figure 4.6 The 7742 cm^{-1} (1292 nm) and 7444 cm^{-1} (1343 nm) lines clearly show self-absorption in the line of sight measurement. This renders them unsuitable for use in a Boltzmann plot.

surrounded by a non-radiating mantle. Moreover, high-resolution measurements (resolution 1 cm^{-1}) through the center of the lamp clearly show self-inversion of the two most intense infrared lines of indium (see figure 4.6). This self-inversion was not detected in the other infrared lines. Therefore, the 7742 cm^{-1} (1292 nm) and 7444 cm^{-1} (1343 nm) lines were omitted from the Boltzmann plots of the InI lamps measured in the integrating sphere.

The emitted power per atomic line was determined by subtracting the continuum radiation from the line radiation. The continuum radiation was determined by measuring the first local minimum to the left and to the right of the atomic line curve. First the total radiative power was determined between these boundaries. Then the average of the spectral power of the left and the right boundary was multiplied by the width of the curve and subtracted from the total power of the curve. This resulted in the atomic line power P_{line} .

For each line $\frac{P_{\text{line}}}{h\nu A_{ul} g_u}$ was calculated, in line with equation 2.19. These values were then plotted against upper energy level $11604 E_u [\text{eV}]$ for each line. Because we assume that the discharge is in LTE these points should lie on one line. A linear fit of this curve results in a slope with a value of $-1/T_c$, while the intersection results in $N_a/Z(T)$, with N_a the total number of particles of the radiating species that are present in the discharge. An example of such a plot can be seen in figure 4.7.

The measured data points do not lie in a straight line, as is to be expected for Boltzmann plots. Rather, the two center points of the plot, belonging to the 6983 cm^{-1} (1432 nm) and 7232 cm^{-1} (1382 nm) lines, lie below the fit, while the rightmost point, belonging to the 6792 cm^{-1} (1472 nm) line, lies above it. This distribution was consistent in all Boltzmann plots created with indium lines, both in side-on measurements as in

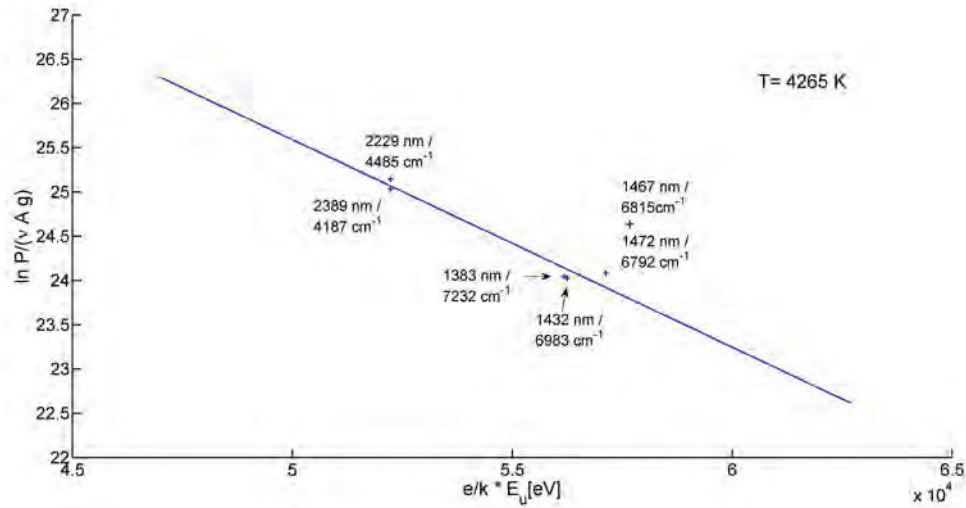


Figure 4.7 An example of a Boltzmann plot. The slope of the fit is $-1/T_c$, while the total number of atomic indium particles in the discharge can be determined from the intersection of the slope with the y -axis and r_{eff} .

integrating sphere measurements, which rules out that the uncertainty in the side-on calibration is responsible for this deviation. Systematic measurement errors could also be responsible for the distribution between the points. The 6792 cm^{-1} , 6983 cm^{-1} and 7232 cm^{-1} are line deviate most from the fit, but they lie in a relatively narrow part of the spectrum. It does not seem likely that there is a systematic measurement error in the spectrum that systematically underestimates the spectral power around 6983 cm^{-1} and 7232 cm^{-1} while at the same time the spectral power around 6792 cm^{-1} is overestimated. Therefore, the deviation between the points could indicate a non-Boltzmann distribution, but uncertainty in the transition probabilities seem more likely.

Unfortunately, Safronova et al. did not specify the errors in their calculations, but an error of 20 % for the value of the transition coefficient is not uncommon in these sorts of simulations. The influence of this error on the outcome of the Boltzmann plots was tested. It was assumed that this error is uniformly distributed for all transition coefficients. Tests showed that the temperature of the fit could easily deviate 400 K and even up to 1000 K for more extreme deviations. These extreme variations would occur if the transition coefficients of the lines with a lower upper energy level were underestimated by 20 %, while the transition coefficients of lines with a higher upper energy levels were overestimated by 20 %, or vice versa. This effect is even more profound for the atomic indium density, since it is calculated from the intersection of the Boltzmann fit with the y -axis: $\ln(N_a/Z(T))$. This means that variations in the fit affect the calculated density exponential. Hence it can differ up to a factor 20 for the more extreme variations in the coefficients. Consequently, this influences the final core pressures and effective radii, which can vary up to 50 %. The error in the transition coefficients therefore limits the

λ (nm)	$\tilde{\nu}$ cm^{-1}	E_u (eV)	$A_{ul}(10^7 \text{ s}^{-1})$	g_u
818.55	12 216.72	3.617	4.29	4
819.70	12 199.52	3.617	0.857	4
819.71	12 199.47	3.617	5.14	6
1138.46	8783.82	3.191	0.880	2
1140.69	8766.62	3.191	1.76	2

Table 4.2 The properties of the sodium spectral lines that were used in the analysis of the discharge [34].

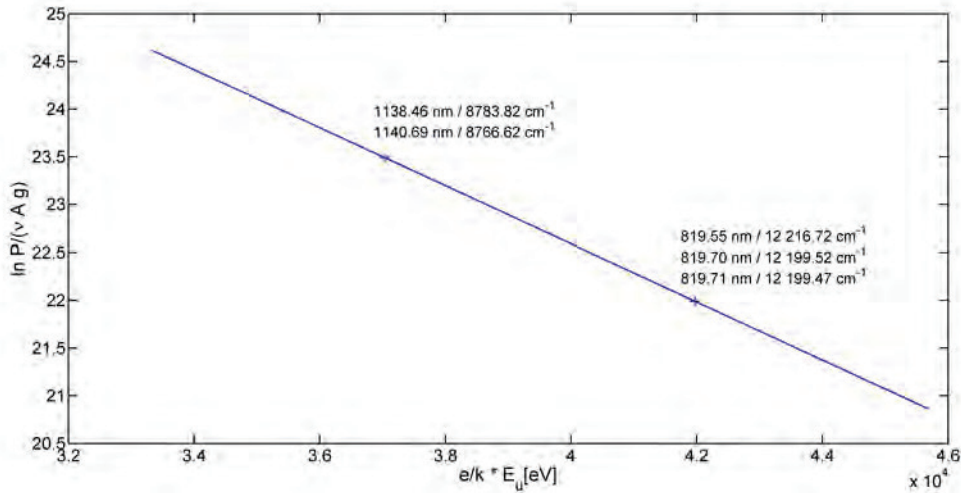


Figure 4.8 An example of a Boltzmann plot with sodium lines. The graph consists of only two data points, because of overlap between atomic lines.

possibility for Boltzmann plots to very accurately predict conditions in the discharge. Because these are errors in the fundamental properties of the atomic lines, they will not influence the trends between lamps.

Of course, Boltzmann plots are not limited to indium. It is possible to create a Boltzmann plot whenever an atomic species has multiple optically thin atomic lines with different upper levels in the spectrum, as long as the transition coefficients of the lines are known. The other species that was sometimes used to create Boltzmann plots is sodium. The lines used for sodium are listed in table 4.2.

An example of a Boltzmann plot with sodium lines can be seen in figure 4.8. The lines in the table overlap and will show up in the spectrum as only two lines. This makes the properties determined from Boltzmann plots of sodium lines less reliable than those from indium lines.

Effective radius and partial pressure The channel model was explained in section 2.6. In the channel model the arc column is viewed as a cylindrical core with

volume V_c (see equation 2.26). By representing the arc column as a cylinder, it is possible to determine the effective radius. This way, we can use the integrating-sphere measurements to get a qualitative estimate for the contraction of the core, without directly observing the discharge.

The amount of power that is dissipated in the discharge is known P_{dis} , by subtracting the electrodes losses P_{el} from the total lamp power P_{la} . The electric field in the discharge is also known, since it can be determined from the lamp voltage and electrodes distance (see equation 2.8). The total power that is dissipated in the cylindrical core is then given as

$$P_{\text{dis}} = V_c \sigma(N_a, T_c, V_c) E^2. \quad (4.5)$$

The core temperature T_c and N_a can be determined using a Boltzmann plot, and the electrical conductivity depends only on T_c , N_a and V_c , as can be seen in equation 2.28. The expression for P_{dis} can then be expressed as:

$$P_{\text{dis}} = 0.75 \frac{n_e V_c}{m_e N_a Q_{\text{eam}} \langle v \rangle} V_c E^2, \quad (4.6)$$

with n_e determined by Saha's equation:

$$n_e^2 = 2 \left(\frac{2\pi m_e k T_c}{h^2} \right)^{3/2} \frac{g_i}{Z(T_c)} \frac{N_a}{V_c} \exp\left(-\frac{E_i}{kT}\right). \quad (4.7)$$

$\langle v \rangle$ can be determined with T_c , while the average electron-atom collisional cross-section Q_{eam} at T_c was determined using the calculations of Felfli et al. [35]. Subsequently, it is possible to determine the volume V_c of the cylindrical core and hence the effective radius r_{eff} (equation 2.26). The partial pressure of atomic indium can be calculated from V_c with the ideal gas law (see equation 2.29).

The fact remains that the channel model is a highly simplified model, but it is very useful in determining trends between lamps.

Bremsstrahlung and recombination radiation Once T_c and $n_a = N_a/V_c$ are determined, it is also possible to estimate the contributions of bremsstrahlung and recombination radiation to the spectrum. The expressions for spectral emission coefficients of all three processes are given in section 2.4.3. It can be seen that these expressions only depend on the electron temperature T_e , electron (and ion) density n_e and atom density n_a . We equate T_e to T_c , since we assume LTE. For the Biberman factors ξ^{rec} and ξ^{ei} in these expressions we took 1 and 4, respectively. These were the same values Lawler et al. [36] used for continuum calculations on a variety of discharge lamps. This way it was possible to calculate the spectral emission coefficients for all three processes. The spectral emission coefficients were then integrated over ν was then multiplied by V_c . This results in the total power output for each process.

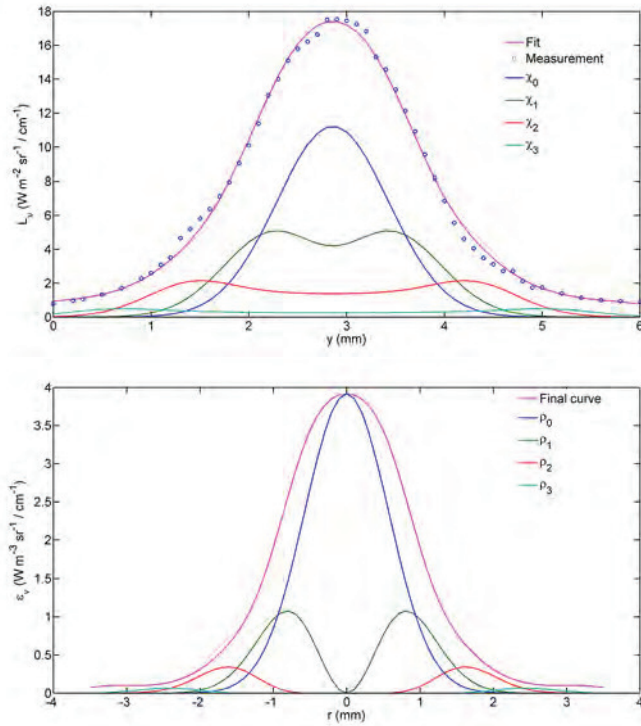


Figure 4.9 An example of fitting the measurements with the BASEX set. On the left there is a lateral spectral radiance profile at a certain wavelength. The fit has been split up in its separate χ_k components. The value of σ remains the same for all curves. On the right the result of the fit is shown, combined with the resulting ρ_k curves.

4.4 Abel inversion of the side-on measurements

As explained earlier, we measured spectra over the complete lateral width of the lamp with a resolution of 0.1 mm. A lateral profile was created for each separate wavelength. Each profile was then fitted with a linear combination of the BASEX set of equations (see equation 2.40). The number of terms would rapidly expand if higher-order equations of the BASEX set were used (χ_4 has already 32 terms), so the set of fitting functions was limited to $k_{\max} = 4$. The value of σ was kept constant for each curve of χ_k to reduce the number of variables. Too little variables resulted in unreliable fits, but too many could result in unreliable radial curves as well. For instance, the higher-order functions of χ_k would sometimes dominate the lateral fit, which naturally resulted in physically incorrect radial profiles. Therefore, the radial profiles had to be carefully reviewed after fitting. An example of the fitting of a lateral profile with the BASEX function can be seen in the top graph of figure 4.9, while in the bottom graph the resulting radial profile is shown.

The Abel inversion resulted in the spectral emission coefficient distribution $j_{\bar{\nu}}(r)$

for different radial position r in the lamp. It was possible to create Boltzmann plots with these distributions, in order to create radially-dependent temperature and density profiles. The calculated temperature will not be perfectly accurate due to uncertainties in the transition coefficients (see section 4.3). Yet it was also shown in that section that any trends between Boltzmann curves would remain valid. Hence it remains possible to create temperature curves from the side-on measurements.

These temperature curves are used to determine contraction of the arc. Arc contraction occurs because the outer area of the core and mantle cool down, due to the emission of optically thin radiation. Because of this radiation, the temperature in the mantle decreases and the core shrinks. A contacted discharge therefore has a thin, hot core, with a large, cool mantle surrounding it with respect to a non-contracted, parabolic temperature profile.

Chapter 5

Experimental results

The goal of this project is to investigate alternatives for mercury in an HID lamp. In section 1.3 the many advantages of mercury were already mentioned, together with the difficulty of finding a suitable alternative. Several alternatives were tested during this project, but indium iodide (InI) as a replacement for mercury was the focus.

All the lamps that were measured during this project contain 350 mbar xenon as a starter gas. The reasons for having a noble gas as a starter gas have already been explained in section 1.1.1.1. Xenon is the heaviest of the stable noble gases, and therefore has the advantage of having a low thermal conductivity in comparison to the other noble gases. This makes xenon very suitable to reduce thermal losses. The discharge tube was made of PCA, unless mentioned differently.

5.1 Indium iodide

During this project several sets of lamps with InI filling have been measured, with differences in vapor pressure, presence of additives and burner type. First, the results of the integrating sphere measurements will be shown and discussed. After that, the results of the side-on measurements will be shown. A final conclusion about the workings of InI will then be given.

In the search for a replacement for mercury as a buffer gas we looked at elements that share (some of) the properties of mercury. The goal of the buffer gas is to make the plasma more resistive, so as to prevent large currents in the discharge. Indium seemed an attractive choice as a buffer gas, because its elastic electron-atom scattering cross section [35] is even higher than that of mercury (cf. [37]) in the energy range where metal halide lamps typically operate (0.1 eV - 1 eV). This has the advantage that the discharge requires a lower indium density to obtain the same potential drop. Like xenon and mercury, it has a relatively large atom weight, which helps to limit the thermal losses.

Unfortunately, like most metals pure indium has a high boiling point at 2345 K at 1 bar, which is far above the typical cold spot temperature of 1200 K. In order to introduce a sufficiently large amount of indium into the discharge, it will have to be

Lamp name	InI(mg)	U_{la} (V)
<i>Low InI</i>	1.08	54.0
<i>Medium InI</i>	2.34	80.7
<i>High InI</i>	5.04	122.5

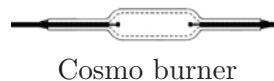


Table 5.1 Each lamp contained 350 mbar xenon as the starter gas. All lamps were driven at 70 W.

bounded into a metal halide. With a boiling point of 985 K at 1 bar indium iodine will be able to obtain high enough vapor pressures, plus the iodine helps contribute to the tungsten cycle and prevent blackening. The excitation and ionization levels of iodine are far above those of indium. Iodine line radiation will therefore be absent from the spectra. Iodine is the heaviest of the stable halogens, and therefore a more suitable partner to indium than, for instance, bromine or chlorine. The latter also suffers from strong reactivity with the electrodes or the wall. For these reasons the choice was made to investigate indium iodide.

One of the central goals of this project was to investigate the buffer gas properties of InI. To this end, the spectra of a set of three lamps with varying indium iodide content were measured in the integrating sphere. The filling of the lamps and the lamp voltage is shown in table 5.1. The burner type that was used was the so-called Cosmo burner. A Cosmo burner is cylindrical burner with its electrodes relatively far apart, which aids in building up voltage. However, its small radius results in larger temperature gradients, which, according to Fourier's law, leads to increased thermal losses. Table 5.1 also shows the excellent voltage-building qualities of indium iodide. Typical commercial metal-halide lamp operates at voltages around 85 V, which is a good reference value. The electrical properties of the lamps affirm the possibility for the use of InI as a buffer gas. Moreover, the *medium InI* lamp provides a good benchmark for the amount of InI needed to get enough resistivity.

5.1.1 Lamp spectrum

The spectral power distributions of the InI lamps can be seen in figure 5.1. Many CMH lamps, such as the Philips CDM-T lamp, are typically operated at 70 W (although other powers are also available). Therefore, all the lamp spectra that are compared in this report are measured of lamps operating at 70 W.

Most of the line radiation can be attributed to atomic indium. The intensity of the infrared lines is especially notable. Trace amounts of sodium and potassium are also visible. Because the second energy levels of sodium (2.10 eV) and potassium (1.61 eV) are relatively low in comparison to indium (3.00 eV), even a small amount of these elements will produce enough radiation to be detected in the spectrum. Not labeled, but also visible in a part of the spectrum (500 nm - 600 nm) are trace amounts of dysprosium in the form of small amounts of line radiation. Finally, there are small traces of aluminium line radiation. Aluminium particles enter the discharge via corrosive processes with the burner wall. The spectra of lamps with PCA burners will therefore always show small

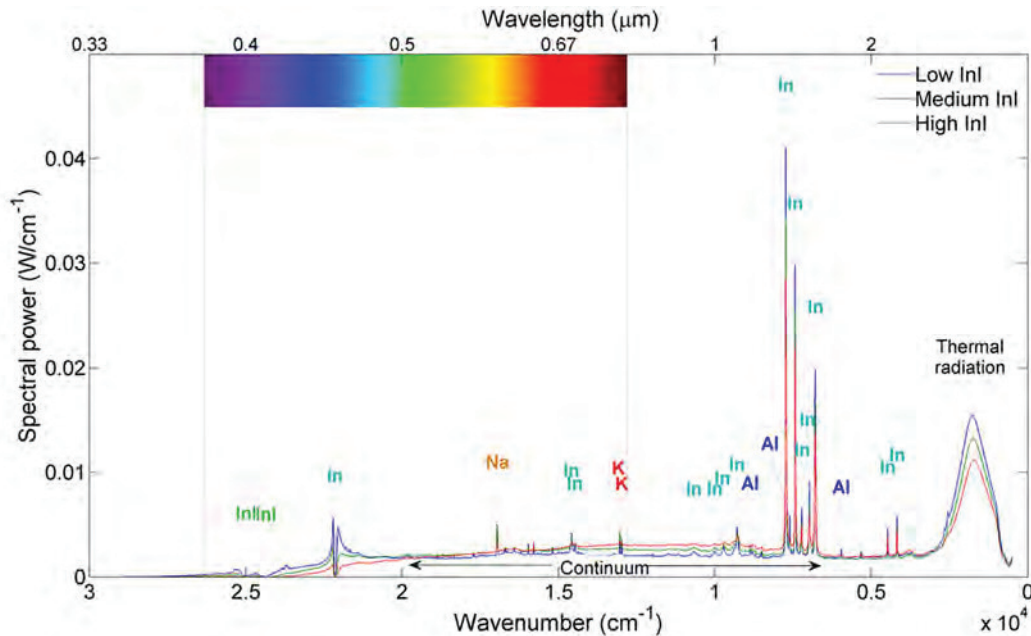


Figure 5.1 The spectral powers for three lamps with various amounts of InI fillings (see table 5.1). Most notable is that for an increase in InI there is an increase in red/infrared radiation at the expense of the radiative output in the blue part of the spectrum.

amounts of aluminium line radiation.

The thermal bump in the infrared is thermal radiation emitted by the discharge tube. The Stefan-Boltzmann law states that the emitted power by the discharge tube wall scales with T^4 , so the height of thermal bump can be used as a measure for the relative wall temperature between lamps, under the condition that the wall emissivity and surface are the same. For instance, figure 5.1 shows that the *low InI* lamp has a relatively hotter wall than the *high InI* lamp.

Very noticeable is the complete absence of UV radiation and the presence of a large, broad band continuum that ranges from the infrared to the blue part of the spectrum. The continuum and the thermal bump dominate the spectrum of all three lamps. The continuum starts at approximately 400 nm, but its right end is more difficult to determine.

The broad spectral range of the continuum is especially notable. Switch-off measurements can be used to separate the thermal radiation of the burner from the plasma radiation and the electrode radiation, as explained in section 4.1.2, by subtracting the thermal radiation spectrum of the burner from the total spectrum. The result can be seen in figure 5.2.

It is difficult to separate the electrode and plasma radiation in the spectrum (this is the reason why the electrode radiation power needs to be simulated). However, electrodes have a typically temperature between but around 2.7 μm there is a sudden decrease in radiation for larger wavelengths in all three lamps. It is not certain if this due to an

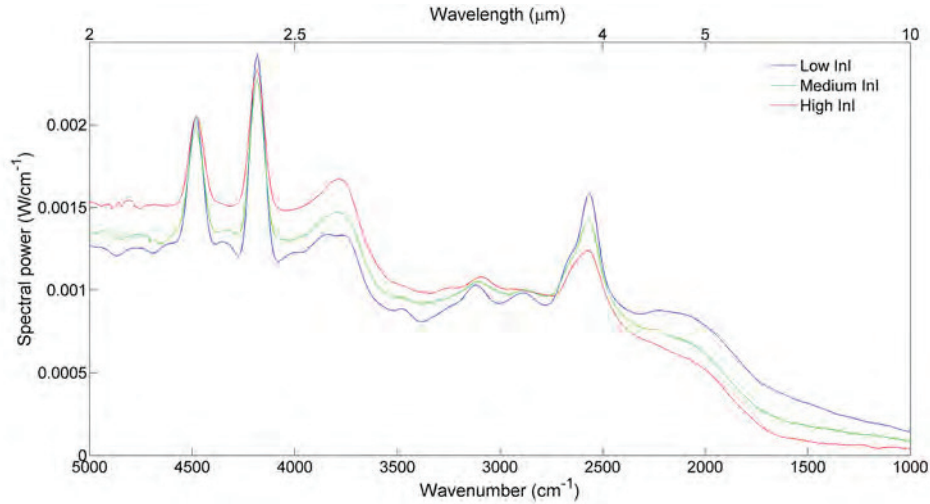


Figure 5.2 The spectrum of the thermal radiation of the burner is subtracted from the total spectrum. The results is a combination of the plasma radiation and electrode radiation.

increase in continuum radiation. There also is the fact that the transmittance of the PCA decreases for wavelengths larger than 4 μm : from almost 0 % at 4 μm to almost 100 % at 6 μm . It is therefore not possible to exactly determine the exact boundaries of the broad band continuum, but we know that it runs at least up to 5 μm .

It appears that most of the radiant flux is emitted as the a continuum. This can be tested by fitting a curve through the local minima in order to estimate the atomic line power, except near the self-inverted 451 nm line. Its contribution to the atomic line radiation was estimated by continuing the trend of the continuum to the left and to the right of the 451 nm line, and integrating the spectral power that lay above this trend. This resulted in an atomic line power of 5.7 W, 4.8 W and 3.5 W for the *low*, *medium* and *high InI* lamps, respectively. This raises the question which process is responsible for the continuum, as the line radiation does not contribute much to the radiant flux of the lamps.

In summary, the increase in InI has three effects in the spectrum: it lowers the amount of thermal radiation from the burner wall, it lowers the intensity of the atomic lines and it increases the amount of continuum radiation. Finding the source of this broad band continuum is one of the main research goals of this study.

5.1.2 Radiative processes in InI lamps

The discharge produces three types of radiation: atomic line radiation, molecular radiation and continuum radiation, which in its turn consists of three processes: recombination radiation, e-i bremsstrahlung and e-a bremsstrahlung. Their contributions to the spectrum will be investigated. To this end the simplifications of the channel model will be used, i.e. the top hat temperature profile.

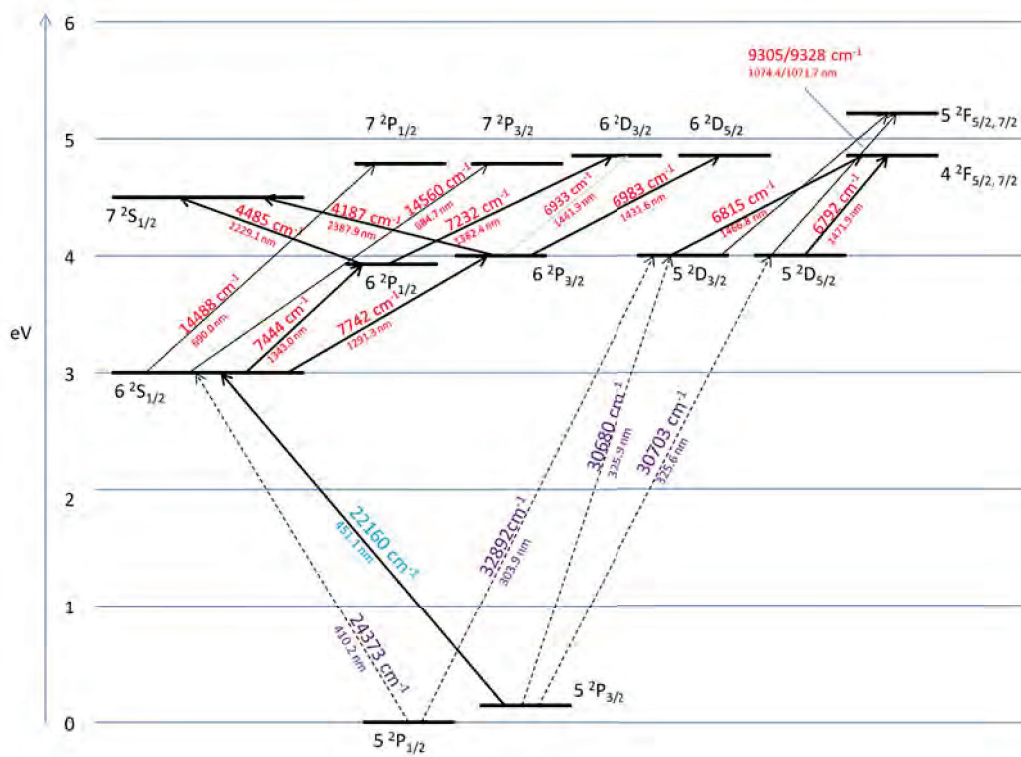


Figure 5.3 The energy diagram of atomic indium [34]. While the transitions between higher excited states are visible in the spectrum, all UV resonance lines remain absent.

5.1.2.1 Atomic line radiation

Figure 5.3 shows the energy diagram for atomic indium, which lists most of the atomic lines that are present in the spectrum. Of the resonance lines in the diagram, only the 451.1 nm line is visible in the spectrum. The $5^2P_{3/2}$ state is a metastable state, so technically its lines are not resonance lines, but we shall ignore this slight distinction. It can be seen that the most heavily radiating lines of the spectrum, the 1343.0 nm, 1291.3 nm and the 1466.8/1471.9 nm lines, are lines whose lower level is an upper level of a resonance line. However, since these higher excited states radiate intensely, there a large amount of UV line radiation should be produced within the plasma. Because this radiation does not leave the lamp, these lines have to be reabsorbed within the discharge and are therefore responsible for radiation transport within the discharge. The contributions of atomic line radiation to the radiant flux are relatively small and are limited to losses in the infrared and the self-inverted 451.1 nm line.

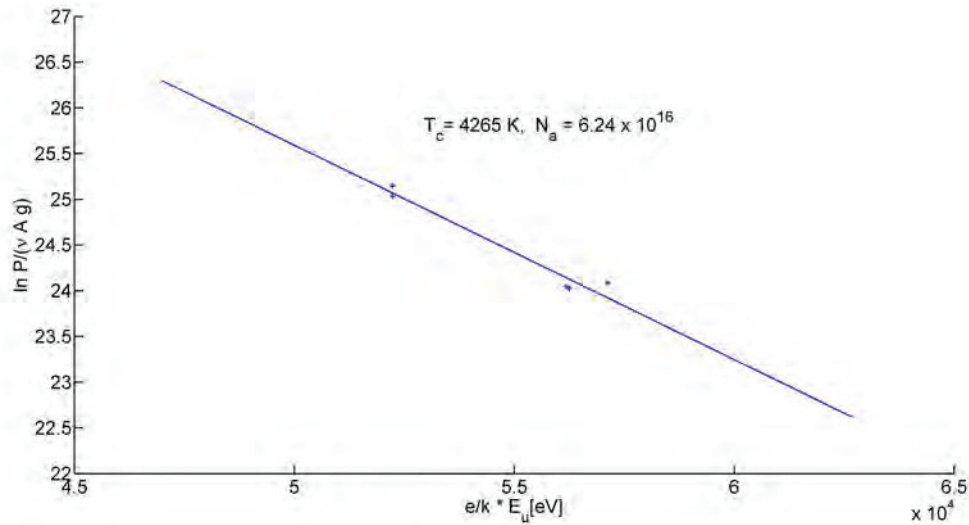


Figure 5.4 The Boltzmann plot of the *medium InI* lamp.

5.1.2.2 Bremsstrahlung and recombination radiation

Recombination radiation, e-a bremsstrahlung and e-i are three processes that can generate a continuum. Conventional mercury lamps often have a considerable radiative output due to continuum processes, so it is logical to determine if these processes are the source of the continuum. The expressions for the radiative output of these processes can be found in section 2.4.3. These expressions show that, aside from several species-dependent properties, these processes only depend on the neutral and electron densities and the temperature. The fact that all three processes require the presence of electrons means that their radiation will be produced in the core of the discharge, hence the channel model is suitable to estimate their influence on the spectrum.

Boltzmann plots were created for all the lamps that were measured (see section 4.3) and their results are used in the channel model. In section 5.1.3 these calculations will be used to draw comparisons between lamps. In this section, the *medium InI* lamp will be used to estimate the radiant flux of the bremsstrahlung and recombination radiation processes. In order to calculate these we need to estimate the core temperature, atomic indium density and electron density.

Therefore, the powers of the infrared atomic indium lines were calculated from the spectrum in *medium InI* lamp in order to create a Boltzmann plot. This plot can be seen in figure 5.4.

The core temperature that was determined from this plot was 4265 K. From intersection of the fit with the y -axis the total number of indium atoms in the discharge N_a was also determined. To determine the contributions of bremsstrahlung and recombination radiation both the density of atomic indium and the electron density must be known. We used the channel model to determine these. In the channel model the discharge is

represented as a cylindrical core with a constant temperature and constant densities into which all power is coupled (see section 2.6). Power is only dissipated in the area of the discharge where electrons are present. Likewise, both bremsstrahlung and recombination radiation require the presence of electrons. The densities calculated in the channel model are therefore suitable to get an estimate of the radiant flux of the bremsstrahlung and recombination radiation. In section 4.3 it was shown that both the electron density and atomic indium density in the core could be determined from the channel model, if T_c and N_a were determined with a Boltzmann plot. The density of atomic indium can be used to determine the electron density from Saha's equation, because it is expected that the ionization of indium is the dominant process that produces electrons. The reason for this is that the ionization level of indium (5.79 eV) is much lower than the other atomic species present in the discharge, iodine (10.45 eV) and xenon (13.43 eV).

Inserting the T_c and N_a from the Boltzmann plot of figure 5.4 into the calculations of the channel model results in a core with an atomic indium density of $2.63 \times 10^{24} \text{ m}^{-3}$ and an electron density of $1.16 \times 10^{22} \text{ m}^{-3}$. These are typical values that were found for all the InI lamps, and which will be used to determine the contribution of the continuum radiative processes.

The expressions for these processes can be found in section 2.4.3. For the electron-atom collisional cross section Q_{eam} of atomic indium the calculations of Felfli et al. [35] were used. Although the particle density of atomic iodine is approximately equal to that of atomic indium, its the column temperature of $\hat{T} = 0.37 \text{ eV}$ is very close to the Ramsauer minimum of the electron-atom cross section of iodine [38]. The cross section is therefore more than ten times smaller than the e-a cross section of indium, so e-a bremsstrahlung due to interactions with atomic iodine is disregarded.

The expressions for continuum radiation given in section 2.4.3 return to total power output of the processes as a function of volume. Finally, we are able to estimate the power that is lost to these continuum radiative processes.

The calculated power output of the continuum radiative processes with respect to the total lamps spectrum can be seen in figure 5.5. The processes have been grouped together. The total power lost to these processes is very small: 1.18 W, most of which is emitted in the infrared part of the spectrum by bremsstrahlung. This leads to the conclusion that these continuum radiative processes have little influence on the radiative output of the InI lamps. This is not surprising. Lamps with significant continuum output typically have a broad core and a considerable mercury pressure (up to 20 bars). The effective radius of 0.319 indicate a relatively contracted lamp. Also, the pressure of atomic indium is approximately a factor 10 lower than the mercury pressure in mercury lamps. So while indium has a significant electron-atom collisional cross section, the fact that these lamps are more contracted and the fact that indium pressure is relatively low severely hampers the output of the continuum processes. Evidentially, bremsstrahlung and recombination radiation processes are not able to produce the spectral flux of the observed broad band continuum.

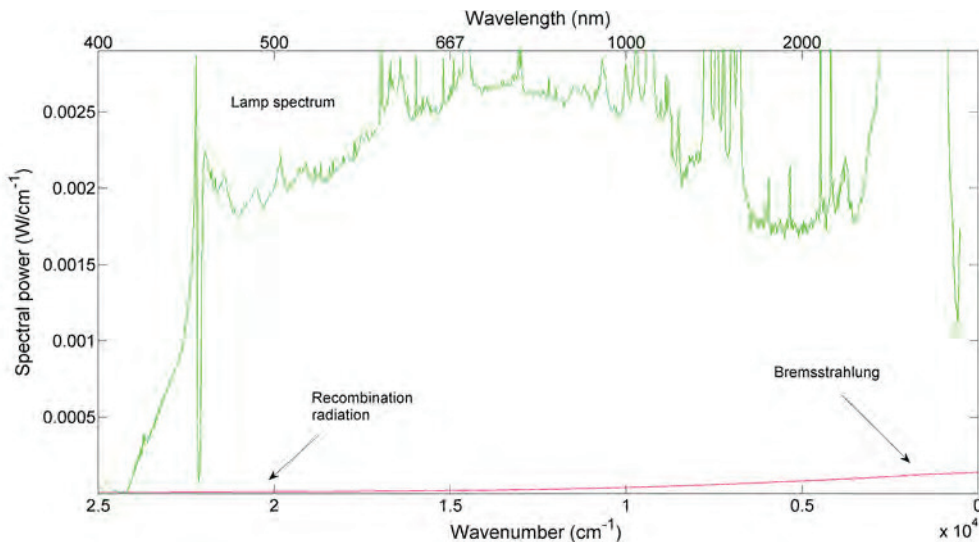


Figure 5.5 The three continuum processes mostly radiate in the infrared part of the spectrum. The recombination radiation and e-i bremsstrahlung have been grouped together into e-i radiation. Very little power is actually lost to these processes: 0.79 W to electron-atom interactions and 0.39 W to electron-ion interactions.

5.1.2.3 Molecular radiation

The iodine vapor pressure in these lamps will be much higher compared to CMH lamps with mercury. This will increase the creation of molecular species in the discharge. The presence of InI can be seen in the spectrum, especially in the tooth-like absorbance band around 400 nm. This band was also observed by Riyves et al. [39], who measured absorbance and emission spectra of low-pressure, low-temperature InI discharges. The tooth-like band is actually a combination of two absorption bands, the X-A (~ 410 nm) and the X-B (~ 400 nm) electronic transition of InI. The 410.2-nm resonance line of indium is located in the center of the X-A absorption band, which can explain its absence. The same article also shows that the InI X-C absorption band is centered around 325 nm and it is therefore able to absorb the $5^2D_{3/2,5/2} \rightarrow 5^2P_{3/2}$ radiation. The findings of Riyves et al. are backed up by Banerjee and Das [40], who performed a theoretical study on the electronic structure of InI. The calculated molecular structure InI is able to not only absorb the resonance lines in the bands measured by Riyves et al., but also all shorter wavelength resonance lines in the ultraviolet range of the spectrum, such as the $5^2D_{3/2} \rightarrow 5^2P_{1/2}$. It seems therefore likely that the absence of ultraviolet (resonance) radiation can be attributed to absorption by InI. However, in order to validate this hypothesis a complex and elaborate model would have to be created, because the electronic structure of InI is very complicated. This is beyond the scope of this work, which focused on experimental work.

It seems plausible that most of the resonance line emission of indium is absorbed by InI. However, it remains the question whether InI is able to produce the (infrared)

continuum radiation. The height of the continuum does increase with an increased InI dosage. The continuum in the spectrum is especially broad, which means that, for molecular radiation to be a likely candidate, one of the two energy levels of the transition has to be either in a repulsive state, or needs to have a relatively flat energy potential energy curve. The A–X transition of InI is good candidate.

The potential curve of the X and A state of InI can be seen in figure 5.6. The energy difference depends on the intermolecular distance between the atoms of the molecule. The actual shape of the continuum depends on several factors, such as the temperature-dependent energy level population, the densities and the transition moment. The larger the distance between the two states at a certain intermolecular distance, the larger the transition moment. The figure shows that the A–X transition is capable of emitting a continuum in the spectral range between 400 nm and 5 μm , approximately the range of the continuum in the spectrum in figure 5.2. Simulations of this discharge by Gnybida et al. [41] have indeed confirmed that the A–X transition is responsible for a large part of the continuum, as can be seen in figure 5.7. The process that dominates the transition is radiative recombination, according to Gnybida et al. The A state of InI dissociates in the ground state of iodine and $5^2\text{P}_{3/2}$, the excited state of indium at 0.27 eV. Likewise, when an iodine atom in the ground state and a $5^2\text{P}_{3/2}$ indium atom meet, they can form a quasi-molecule in the A state, which immediately falls back to an InI molecule in the X state. The bottom graph of figure 5.6 shows that the A–X band can emit a continuum between 400 nm and 6 μm , which is the same range as the broad band continuum that was measured in the *InI* lamps. Gnybida et al. also showed that an increase in indium pressure leads to an increase of the infrared/visible continuum radiation, which is in accordance with our measurements. There remains a difference between the simulations and the experimental data. In these simulations, only the A state and an the lowest energy repulsive state of InI have been taken into account. The model therefore still shows considerable UV emission, but this can be attributed to the absence of other molecular transitions in the model. In fact, further simulations within the EPG have already calculated the spectrum with the 33 energy states of InI taken into account. These simulations showed a sever decrease in the emission of the ultraviolet radiation. More importantly, the model validates the theory that the continuum is indeed a molecular band.

5.1.3 Boltzmann plots

In section 5.1.2.2 we already used the Boltzmann plot of the *medium InI* lamp to estimate the influence of bremsstrahlung and recombination radiation on the spectrum of the lamps. These results of these plots can also be used with the channel model to estimate the contraction of the arc column in the lamps. Contraction is an undesired effect of the buffer gas, since it limits the amount of additives that can be added to the lamp filling.

In order to get insight in the conditions inside the discharge, several infrared atomic indium lines were used to create Boltzmann plots of the InI lamps. The Boltzmann plot of the *medium InI* lamp can be seen in figure 5.4. The values T_c and N_a that result from Boltzmann plots can be used in the channel model. The resulting discharge properties

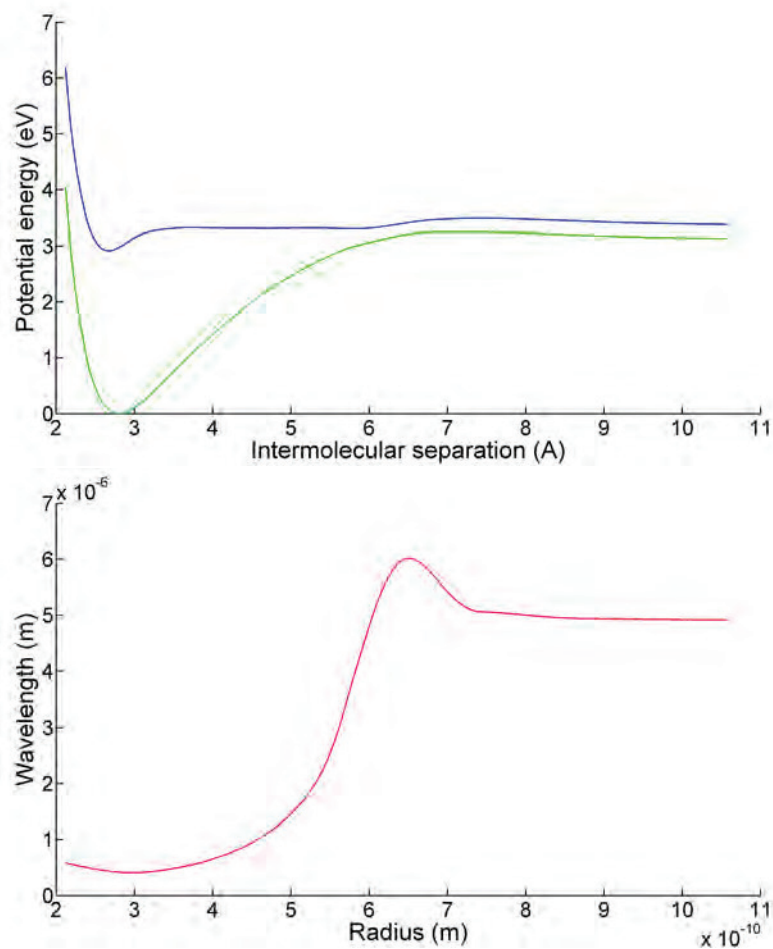


Figure 5.6 The potential energy for the A and X states of InI is plotted as a function the intermolecular separation between the two atoms of the molecule in the top figure. The wavelength of the photon that is emitted as a results of a transition from the A state and the X state depend therefore also depends on the the intermolecular separations, which is shown in the bottom figure. This shows that transitions between the A and X states of InI can emit a continuum (400 nm - > 5 μ m) that is in the range of the continuum that is seen in the spectral power distribution.

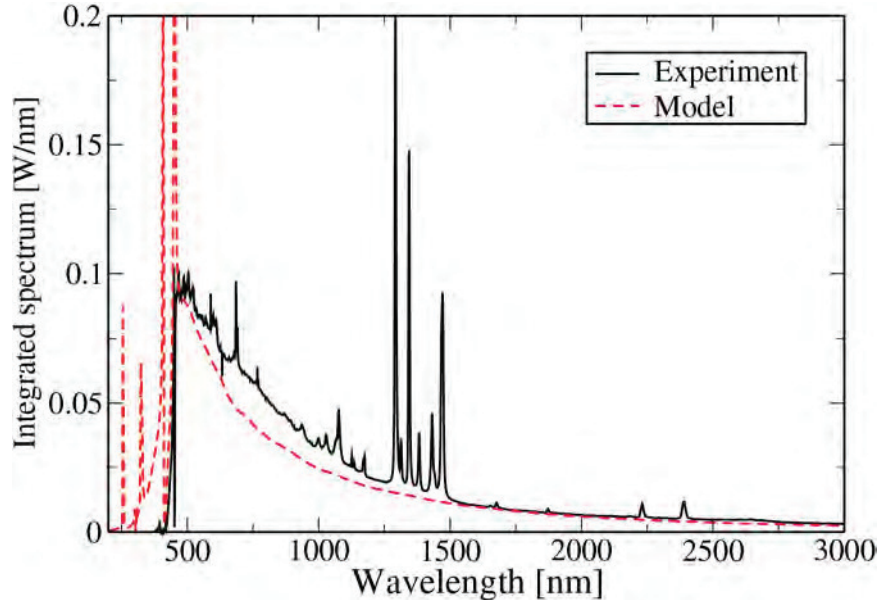


Figure 5.7 Gnybida et al. [41] simulated an XeInI_3 discharge. For molecular radiation they only took the A–X and an unnamed repulsive transition into account. A large part of the continuum appears to be caused by the molecular radiation.

Lamp	T_c (K)	n_a (10^{24} m^{-3})	n_e (10^{22} m^{-3})	p_a (bar)	r_{eff} (R)
<i>Low InI</i>	4266	1.70	0.93	1.00	0.441
<i>Medium InI</i>	4265	2.63	1.16	1.55	0.319
<i>High InI</i>	4109	4.50	1.10	2.55	0.276

Table 5.2 The results of the Boltzmann plots for the InI lamps. Most noticeable is the fact that the core of an InI lamps seems to contract by adding InI. The *high InI* lamp has a lower core temperature than the other two. A possible explanation is that the core of this lamp is more effectively cooled by the emittance of optically thin molecular radiation.

can be seen in table 5.2.

The most important result of the calculations is the fact that adding InI to the discharge appears to lead to contraction of the arc. It seems that contraction is responsible for the voltage building qualities of indium, despite its large electron-atom collisional cross section. This is also caused by the relatively low indium pressure in the core of the lamp. Although not a problem per se, too much arc contraction can lead to arc instability.

The atomic indium pressure in the core is another point of interest. The InI dose in the salt pool more than doubles for the *medium InI* lamp and more than quadruples for the *high InI* lamp with respect to the *low InI*. However, the total number of indium particles N_a in the discharge, which results from the Boltzmann plots, is between 6×10^{16} and 8×10^{16} for all three InI lamps. The lamps operate in saturated mode, i.e. the salt pool is not fully evaporated. The number of species in the discharge is therefore not di-

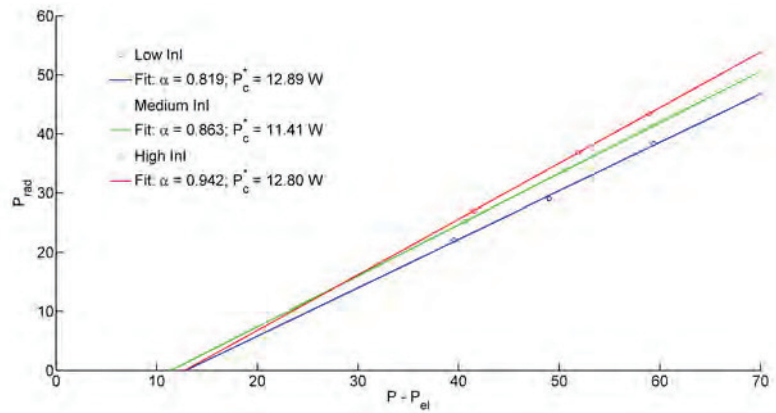


Figure 5.8 The Elenbaas plots for the InI lamps.

rectly related to the content of the filling, but the cold spot temperature. Unfortunately, the Boltzmann plots can only be used to determine the density of atomic indium. The density of the indium iodide and atomic iodine remains unknown.

The relatively low core temperature is also surprising. A core temperature around 4200 K is considered very low, for instance, in comparison to mercury discharge lamps, which have a core temperature of 5600 K [21]. However, we already showed in section 4.3 that a 400 K error is not unrealistic for these Boltzmann plots. Also, the top hat temperature profile of the channel model is simplified compared to the actual temperature profiles.

5.1.4 Elenbaas plots

Elenbaas plots give further insight into the non-radiative losses. The lamps were measured at three powers: approximately 70 W, 60 W and 50 W. The plasma radiation power was determined at each power and plotted against the discharge power. We then fitted a line through these data points. From the fit parameters we are able to determine the absorption and the core conduction power losses (see section 4.2). Figure 5.8 shows the Elenbaas plots of the InI lamps. The plasma core conduction losses can be determined from the crossings of the fit with the x -axis of the plot. The plasma core conduction losses are 12.9 W, 11.4 W and 12.8 W for the *low InI*, *medium InI* and *high InI* lamps, respectively. The absorption losses, calculated with equation 2.35 are 8.5 W, 6.6 W and 2.7 W, respectively.

Absorption losses are either caused by absorption by the mantle of the discharge or absorption by the wall. The absorption losses decrease when the InI dose in the lamps is increased. This is counterintuitive, since r_{eff} decreases when the InI content is increased, therefore increasing the size of the mantle. We would therefore expect an increase in the absorbed power for lamps with a larger InI dose.

A possible explanation for this discrepancy may be due to the nature of the radiation.

The Elenbaas theory was developed for lamps where much of the radiation is atomic in nature. These broad atomic lines are emitted from the core and partly absorbed in the mantle, which causes lines to become self-inverted or even absorbed. This is a process is a balance between absorption and emission and is determined by LTE theory. This absorption contributes significantly to P_{abs} . In the spectra this is visible for the 451 nm resonance line of indium, which is the strongest for the *low InI* lamp. The line's intensity decreases as the InI dose in the lamps increases, limiting its contribution.

However, the *InI* lamps have much more molecular species present in the discharge. These are also strong absorbers of indium atomic line radiation. However, the excited states of InI are often very weakly bonded or even repulsive in nature. We showed in the section 5.1.2.3 that the X–C transition of is capable of absorbing 325 nm resonance radiation of atomic indium. However, the C state is a repulsive state, so the InI molecule will immediately split up in a (ground-state) indium atom and a (ground-state) iodine atom. The InI molecules in the C state are not able to emit the 325 nm radiation, and therefore destroy the balance. Moreover, the resulting ground-state iodine atom can recombine with indium atom in the (quasi-) ground state $5^2P_{3/2}$ and emit A–X radiation, the transition that is responsible for much of the continuum emission. This mechanism could explain why less radiation is absorbed in lamps with a smaller core and wider mantle, because the InI pressure will be larger in these lamps.

The *low InI* shows higher core conduction losses than the *medium InI*. Conduction losses can be described in the first order as $P_c^* = \lambda \Delta T / \Delta r \approx \Delta T / (R - r_{\text{eff}})$. Table 5.2 shows that the atomic indium density increases with the InI lamp. Translational conductivity is independent of the heavy particle density, however, so this has no influence on the conductivity. By definition there will be no electrons present at r_{eff} , so electrons will not contribute to the thermal conductivity. All three lamps contain the same species, so reactive conductivity will not vary much between lamps. We can therefore assume that the thermal conductivity coefficient does not vary much in the different cores of the lamps. This means that P_c^* will be determined by $\Delta T / (R - r_{\text{eff}})$.

Difference in the core conduction losses can then be estimated as $(T_c - T_{\text{wall}}) / r_{\text{eff}}$. The core conduction losses of the *medium InI* lamps will be smaller with respect to the *low InI* lamp, because its effective radius is smaller. The same is true for the *high InI* lamp, which has an even more contracted core. The temperatures in the cores of the *low* and *medium InI* lamps are the same, according to the Boltzmann plots (see table 5.2). Because $R - r_{\text{eff}}$ is larger for the *medium InI* lamp, P_c^* will be smaller. This, however, is not in line with the *high InI* lamp, and requires an explanation.

The *high InI* lamp is a special case. The absorption coefficient α is very high for this lamp, especially compared to Elenbaas plots of commercial lamps [8], which have an absorption coefficient of approximately 0.85. Its core conduction losses do not seem in line with the other two lamps. In lamps with similar indium pressures arc instability due to contraction has been witnessed. A result of this instability is the ‘bending’ of the arc. This is elaborated on in section 5.3.1. It is possible that the bended arc will be relatively close to the wall. This reduces the size of the mantle locally, which explains why the absorption losses in the *high InI* lamp were much lower than in the other lamps.

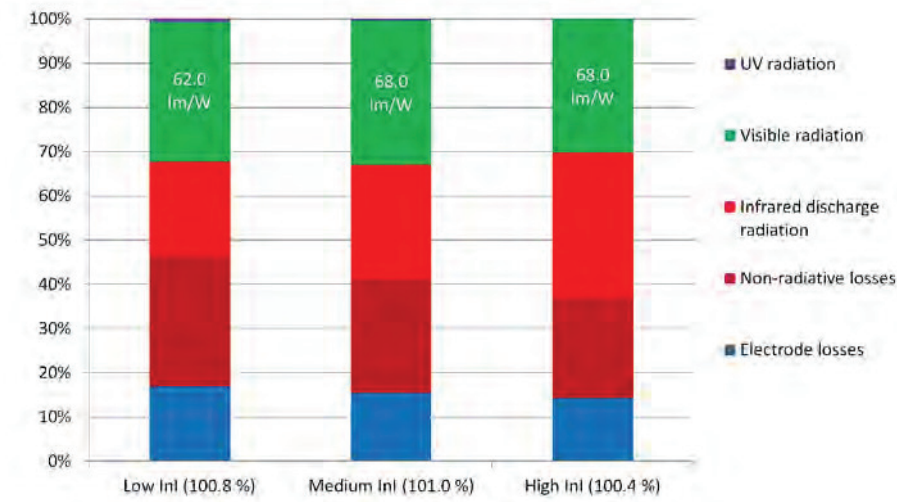


Figure 5.9 The different parts of the energy balance are shown as a percentage of the total power output. The ratio of the lamp output power, calculated by adding the different power flows, and the lamp input power, calculated from the voltage and the current, is shown between brackets. The energy balance shows the different loss processes of the lamps relative to the power input for the three InI lamps. An increase in InI concentration shift the loss balance in the lamps from non-radiative and electrode losses to infrared discharge radiation. The total visible radiation power output remains mostly unaffected.

It also explains why the core conduction losses are larger. The core will be closer to the wall, which increases the temperature gradient over the mantle and therefore increase the core conduction losses.

5.1.5 Energy balance

The energy balance for the three InI lamps can be seen in figure 5.9. The plasma radiation was determined from the spectra and the switch-off measurements. The non-radiative losses could be determined in two ways (see equation 4.4): from the Elenbaas plot or directly from the switch-off and conduction measurements. The difference between the two methods was less than 3 %. The total output power was calculated by adding the different power flows of the energy balance. This can be compared to the input power of the lamp, which is calculated with the lamp current and voltage. The difference is very small, which confirms the accuracy of the setup and the calibration.

The most significant consequence of increasing InI is that it increases infrared plasma radiation at the expense of the non-radiative losses. This can also be seen in the spectrum, where an increase in InI content leads to a lower thermal bump, but an increase in the broad band continuum. Most of this continuum lies in the infrared part of the spectrum and has relatively little influence in the visible radiative power output. The efficacy of the *InI* lamps is still considerably lower than commercial mercury containing CMH lamps, and their CCT considerably higher, but this may be improved by adding

Lamp name	InI (mg)	NaI-DyI ₃ (mg)	U _{la} (V)
<i>Low InI + NaI-DyI₃</i>	1.08	1.49	63.5
<i>Medium InI + NaI-DyI₃</i>	2.34	1.49	85.9

Table 5.3 A small amount of NaI-DyI₃ was added to two lamps of the InI set. Each lamp contained 350 mbar xenon as starter gas was driven at 70 W. The discharge tube was again a Cosmo burner.

salt additives to the lamp filling. This is covered in section 5.2.

It shows that InI is an efficient light source, with an efficiency over 30 %. When comparing visual output the *medium InI* lamp has the best performance, although varying the indium iodide content does not have much influence on the visible radiative output of the lamp. It does have some influence on the efficacy: this is 5 lm/W lower for the *low InI* lamp compared to the other two lamps. This can be attributed to the increase in red and green light emission at the expense of the blue light, to which the eye is less sensitive. This is also visible in the correlated color temperature, which decrease from 6800 K for *low InI* lamp, via 5300 K for the *medium InI* lamp to 4400 K for the *high InI* lamp. Adding InI therefore has a (limited) positive influence on the radiative output of the lamp. Due to the lower currents, increasing InI also helps to reduce electrode losses.

5.2 Indium iodide lamps with additives

In commercial metal-halide lamps additives are added to the lamp filling to increase the efficacy of the lamp, because the metals in general have a lot of atomic lines in the visible part of the electromagnetic spectrum. Commonly used metal halides are sodium iodide and thallium iodide, while rare-earth iodides, such as dysprosium, holmium, scandium and thulium, are also used [3]. We chose to add sodium iodide (NaI) and dysprosium iodide (DyI₃) to two lamps with the same InI filling as the *low* and *medium InI* lamps. Their metals radiate mostly in the red and yellow part of the visible spectrum, so it could possible lower the CCT and at the same time raise the efficacy of the lamp. The exact fillings can be seen in table 5.3, along with the lamp voltage. It should be noted that especially the *medium InI + NaI-DyI₃* lamp behaved relatively unstable during measuring, with currents varying between 0.81 A and 0.86 A. This could indicate arc instability.

5.2.1 Lamp spectrum

The spectral power distributions of *InI + additives* lamps can be seen in figure 5.10. The effect of the additives can be seen clearly in the visible red part of the spectrum, where there is a significant increase in the radiative output of the lamps. The relative increase is larger in the *low InI* lamps than in the *medium InI* lamps. The main contribution of sodium is its D line at 589 nm, which is self-inverted and heavily broadened. The broadened, ‘spiked’ continuum can be contributed to the dysprosium, which has many

low-energy atomic states, and dysprosium iodide. A similar continuum for an HID lamp filled with DyI_3 was witnessed by Käning et al. [42].

As a result of the addition of NaI-DyI_3 in the *low InI + NaI-DyI₃* lamps the line radiation of indium and molecular radiation of InI are reduced, although the latter very limited. For the *medium InI+NaI-DyI₃* lamp, the atomic indium lines are still reduced, but less strongly with respect to the *low InI + NaI-DyI₃* lamp. The molecular radiation is not reduced in this lamp.

It is not surprising that the atomic indium lines are reduced. The energy levels of dysprosium and sodium lie at lower energies than those of indium. Because sodium and dysprosium which makes them efficient emitters of radiation, the outer regions of the core are cooled, which leads to arc contraction. The reduction of the core most likely limits the emission of indium line radiation. There is also the possibility that the salts extra iodine into the discharge which shifts the $\text{In} + \text{I} \leftrightarrow \text{InI}$ balance towards InI , although we would expect this to have an effect on the emission of the molecular radiation.

The salts also reduce the wall temperature, which is deduced from the height of the thermal bump. This indicates that the non-radiative losses are reduced by the addition of NaI-DyI_3 . The emission of optically thin radiation by the additives is the main reason for this effect.

The added salts also increase the resistivity of the lamps. The reason for this is that the contraction of the the arc. This limits the amount of additives with which the lamp can be filled, because too much contraction can cause arc instability.

5.2.2 Boltzmann plots

Determining r_{eff} for the InI lamps with additives is considerably more complex than for the lamps with just InI as filling. In the lamps with additives, multiple species can be ionized, because, unlike iodine and xenon, dysprosium (5.94 eV) and sodium (5.14 eV) have ionization levels of a similar energy as indium (5.79 eV). The electron density therefore depends on the particle density of these species. Also, the electron-atom collisional cross section of sodium is of the same order of magnitude as that of indium, so it cannot simply be ignored [43]. In order to calculate r_{eff} , the densities of indium, sodium and dysprosium should all be known, as well as their cross sections. The density of indium can be determined in the same way as in the lamps with just InI filling. For sodium, only two lines are available to create a Boltzmann plot, at $12\,199\text{ cm}^{-1}$ (819 nm) and at 8767 cm^{-1} (1141 nm), with the latter being relatively weak. The reliability of Boltzmann plots decreases greatly if the number of points is reduced. Several lines of dysprosium are visible, but these are relatively weak and hard to separate from the continuum. Besides that, dysprosium has a very complicated electronic structure, hence the corresponding energy states or the transition coefficients are not known for many lines. Therefore, no Boltzmann plots could be created for dysprosium. Since the conditions in the discharge depended on three different species, whose exact parameters could not be determined, it was not possible to calculate partial pressures of the different atomic species or the effective radius.

5.2 Indium iodide lamps with additives

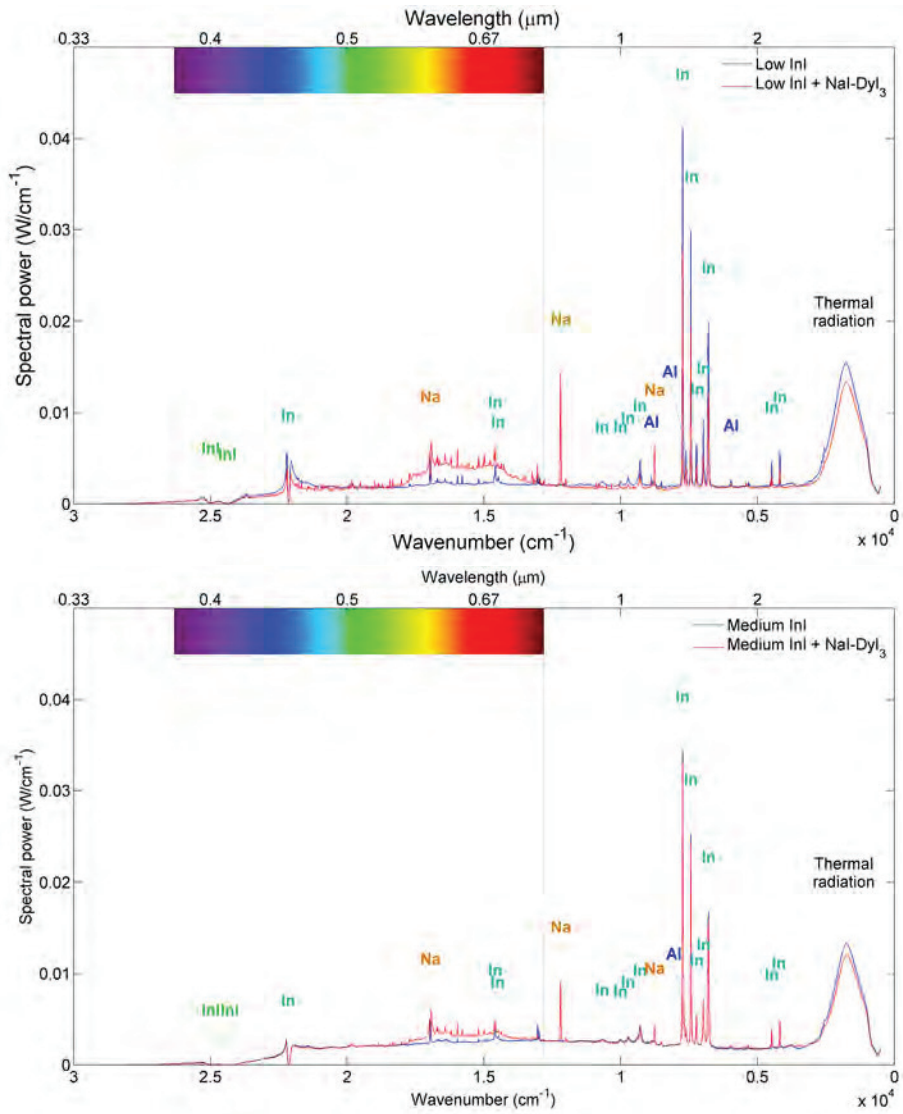


Figure 5.10 A comparison between the spectral power distributions of the lamps filled with just InI and their counterparts, which have NaI-DyI₃ added to their fillings.

Lamp	Indium T_c (K)	Sodium T_c (K)	$N_{\text{In}}/N_{\text{Na}}$
<i>Low InI + NaI-DyI₃</i>	4880	3291	2
<i>Medium InI + NaI-DyI₃</i>	4550	3873	74

Table 5.4 The results of the Boltzmann plots for the InI + NaI-DyI₃ lamps.

It does remain possible to create two Boltzmann plots with the atomic lines of indium and sodium, and deduce a temperature from both plots. It is not possible to determine the density of both atomic species from these plots, because the core volume cannot be calculated as we explained above. However, the Boltzmann plots do result in the absolute number N_i of each species in the discharge, so the relative density of the indium and sodium atoms with respect to each other can be calculated. The results can be seen in table 5.4.

There is a discrepancy between the temperatures of the indium Boltzmann plots and those of the sodium Boltzmann plots. This may be the result of de-mixing. In section 1.1.2.3 we explained that the active species are more likely to leave the core of the plasma than the buffer gas. Hence sodium may on average radiate from a cooler region in the core than indium. The indium and sodium lines also follow a different trend. The core temperature determined from the indium lines is more reliable, since the Boltzmann plots for indium are created with more lines than for sodium.

There also is the fact that the 1138.46 nm/1140.69 nm line has a relatively low intensity, especially in the *medium InI + NaI-DyI₃* lamp (see figure 5.10). The figure also shows that the line lies on an uneven part of the continuum, i.e. the radiation on the left side of the line has a higher spectral power than the radiation on the right side of the line. On top of that the measurements were taken with a relatively low resolution of 16 cm^{-1} . This makes it difficult to accurately separate this line from the continuum. This line has a lower upper energy level (3.19 eV) than the 819 nm line (3.61 eV). Its underestimation will therefore lead to an overestimation of the temperature. This could explain why the Boltzmann plot of the sodium lines shows a higher core temperature for the *medium InI + NaI-DyI₃* lamp than for the *low InI + NaI-DyI₃* lamp.

The difference in $N_{\text{In}}/N_{\text{Na}}$ between the lamps is also notable. While we expect this to increase because the InI content increases, an increase from 2 to 74 seems very large, as the InI content in the filling is only doubled. However, the same reasoning applies as for the core temperature, only in this case the underestimation of the 1140.69 nm line leads to an underestimation of N_{Na} . The value of 74 is therefore most likely an exaggeration.

The estimation of the core temperature with the indium lines is more reliable than the estimate with the sodium lines. In this case the core temperature appears to increase with respect to the indium iodide lamps without additives, which is most likely an effect of contraction of the arc. From the relative densities it can be deduced that in the *medium InI + NaI-DyI₃* lamp indium is much more dominant than in the *low InI + NaI-DyI₃* lamp, which could explain why the addition of NaI-DyI₃ has much less impact on the spectrum of the lamp with higher InI content. However, the relative densities are

subject to discussion due to the large uncertainties in the Boltzmann plot of the sodium lines in the *medium InI + NaI-DyI₃* lamp.

5.2.3 Elenbaas plots

Elenbaas plots were created of both lamps. The *low InI+NaI-DyI₃* lamp had an absorption coefficient of 0.873 and core conduction losses of 12.3 W, while the values for the *medium InI+NaI-DyI₃* lamp were 0.885 and 10.5 W. The resulting absorption losses are 6.0 W and 5.8 W, respectively. It is interesting to see that the reduction of non-radiative losses is mostly gained due to the reduction of the core conduction losses.

The core conduction losses decrease for an increased InI dose, just as in the *InI* lamps. The core conduction losses for these lamps are also reduced with respect to their counterparts without additives: 0.5 W for *low InI+NaI-DyI₃* lamp and 0.9 W for the *medium InI+NaI-DyI₃* lamp. This is not very significant, but it appears that the lamps with additives have a larger core temperature. The gradient $(T_c - T_{\text{wall}})/(R - r_{\text{eff}})$ is therefore only reduced if the core contracts significantly.

Also notable is the fact the absorption losses again decrease with an increased InI dose, just like in the *InI* lamps, thereby reinforcing the idea that the increased presence of (quasi-)molecular species reduces absorption losses. The absorption losses of both lamps also decrease with respect to the *low* and *medium InI* lamps. The reduction is 2.1 W for *low InI+NaI-DyI₃* lamp and 0.8 W for the *medium InI+NaI-DyI₃* lamp. The reduction is less in the *medium InI+NaI-DyI₃* lamp. A possible reason for this is that the additives are less dominant in the *medium InI+NaI-DyI₃* lamp.

5.2.4 Energy balance

The energy balance of the *InI+NaI-DyI₃* lamps can be seen in figure 5.11. For comparison, the energy balances of the lamps without salt additives have been given too. The addition of NaI-DyI₃ is positive, as it helps reduce infrared, non-radiative and electrode losses and boosts the visible output. It also gives a significant boost to the efficacy of the lamps, which is 87 lm/W and 82 lm/W for the *low* and *medium InI+NaI-DyI₃* lamp, respectively. This is an improvement, but still significantly below the efficacy of commercial lamps.

The possible explanation that the efficacy of the *medium InI+NaI-DyI₃* is lower than the *low InI+NaI-DyI₃* is that the relative amount of additives is less in this lamp compared to the *InI* lamp, which is unfortunate, as the *medium InI* showed a resistivity that was comparable to commercial lamps. A possible solution would be to increase the amount of NaI-DyI₃. However, we know that both InI and NaI-DyI₃ cause contraction of the arc, so we are limited in the amount of NaI-DyI₃ that can be added to the discharge, since too much arc contraction is undesired.

It can be concluded that NaI-DyI₃ improves the efficacy of the lamp, although the improvement is not as large as in mercury CMH lamps [14]. However, it adds to the contraction of the arc, due to the emission of optically thin radiation by NaI and DyI₃. Especially the variations in lamp current during operation indicate that the arc might

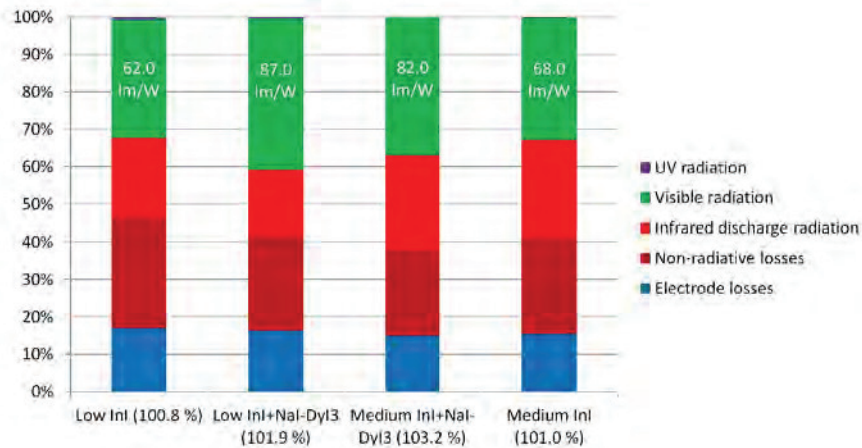


Figure 5.11 The energy balance of the InI + NaI-DyI₃ lamps are compared to the energy balance of the InI lamps. The different parts of the energy balance are shown as a percentage of the total power output. The ratio of the lamp output power, calculated by adding the different power flows, and the lamp input power, calculated from the voltage and the current, is shown between brackets. The additives have a positive influence on the visible radiation power, but this effect is less significant for the *medium InI + NaI-DyI₃* lamp.


Lamp name	InI(mg)	U_{la} (V)	
<i>Low InI YAG</i>	1.5	40.7	 YAG burner
<i>High InI YAG</i>	4.5	57.4	

Table 5.5 Each lamp contained 350 mbar xenon as a starter gas. The lamps were driven at 70 W. Both lamps were mercury-free.

be unstable, which would mean that the amount of NaI-DyI₃ is limited if these lamps are to become commercial products. Unfortunately, its beneficial effects on the efficacy are diminished for higher concentrations of InI.

5.3 Side-on measurements on InI lamps

We have shown so far that lamps with high InI doses emit large amounts of optically thin molecular radiation. Boltzmann plots determined from the integrating-sphere measurements indicate that this can cause contraction. To confirm this, additional measurements were wanted. Unfortunately, the lamps used in the integrating-sphere experiments could not be used, because their discharge tube was removed from its outer bulb and therefore could not be operated under atmospheric conditions. The fact that their discharge tube was made of PCA would provide an additional challenge, because PCA is translucent, not transparent. Therefore, we obtained two different lamps with similar filling, so without mercury filling, in a burner made of YAG. The specifications of the lamps can be seen in table 5.5. The filling is comparable to the *InI* lamps of section 5.1. The voltage

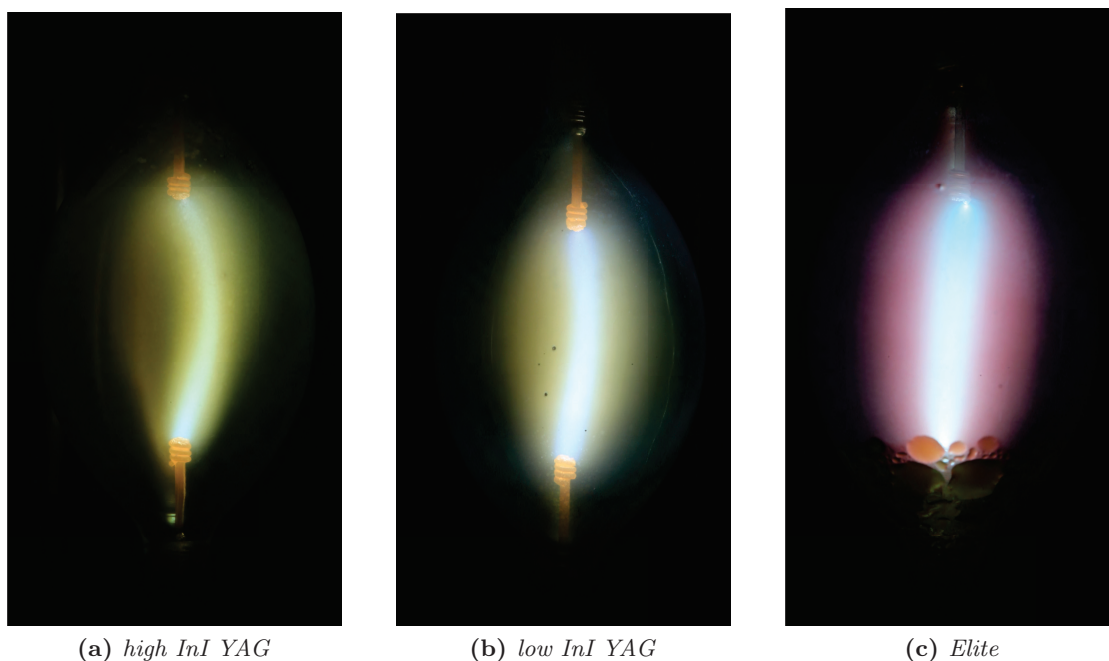


Figure 5.12 The photos of the lamp show that the InI lamps are contracted compared to the *Elite* lamp.

over the lamp is lower, though, because the electrode distance these lamps is only 7 mm compared to 14 mm for the PCA lamp. This is also an important reason why the H bridge was designed during this project (see section 3.1), since ordinary lamp ballast were incapable of driving these lamps.

5.3.1 Photos

Both lamps were photographed using a cross polarized filter. These photos were compared to those of a commercially available CDM-T *Elite* lamp, an CMH lamp filled with mercury and additives. The goal of the photos was to see if contraction of the arc could be confirmed visually. The results can be seen in figure 5.12.

The discharge consists of a strongly radiating channel in the center of the discharge, surrounded by a yellowish glow for the *InI YAG* lamps and an reddish glow for the *Elite* lamp. This glow could be molecular radiation. The radiating channel is the broadest in the *Elite* lamp. It looks thinner for the *low InI YAG* and the thinnest for the *high InI YAG* lamp.

This can be visualized more clearly if we look at the horizontal cross section of each lamp. The cross section is defined as the pixel count of a horizontal line through the center of the lamp. To acquire this cross section the RGB images were converted to grayscale. RGB-to-grayscale conversion ensures that the luminance of the photo is conserved. The cross section is acquired by plotting their relative intensity of the pixel

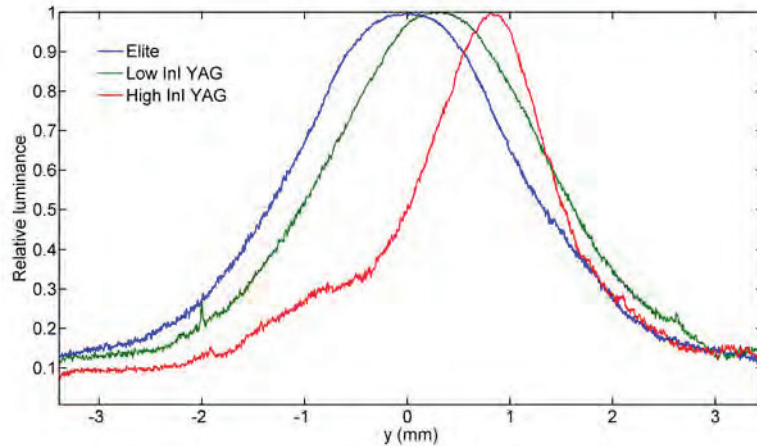


Figure 5.13 The relative intensity of pixel count of a line through the center of each lamps as a function of the radius.

counts against the radius of the lamps. The results can be seen in figure 5.13. The figure shows that the *Elite* lamp and the *low InI YAG* lamp have a broader profile than the *high InI YAG* lamp. The curves of the *low InI YAG* lamps and *Elite* lamp both have a FWHM of 2.40 mm, while the *high InI YAG* lamp has a FWHM of 1.38 mm. The difference between the FWHM *low InI YAG* lamp and that of the *high InI YAG* lamp shows that adding InI to the discharge contracts the arc.

The photos also brought to light some issues that severely complicated the lateral measurements in the side-on setup. The arcs of *InI YAG* lamps were bended, especially the arc of the *high InI YAG* lamp. The *high InI YAG* was also unstable. Bending is the result of the contraction of the arc. The more contracted the discharge is, the higher the self-induced magnetic field is. The magnetic field will increase because the current density increases. The Lorentz force resulting from this magnetic field will be oriented towards the axis and give rise to a small increase in gas pressure along the axis. This changes when the arc is curved. Curvature can be the result of small instabilities in the arc, caused by convection flows in the discharge or electrode effects. In the case of the *YAG InI* lamps the electrodes have been identified as a reason the arc is curved. Figure 5.14 shows a photo of one of the electrodes of the *high InI YAG* lamp. The electrode is heavily eroded, most likely due to the high currents in the lamp. High currents will heat up the electrodes and accelerate the evaporation rate of the tungsten. This leads to eroded electrodes, which can result in a curve in the discharge. Any curvature of the discharge will be increased by the magnetic field of the discharge, since the magnetic field, and hence the Lorentz force, will be greater on the inside of the curvature than on the outside. This results in a more bended discharge and can even lead to unstable behavior, such as a sudden shift of the arc.

Erosion of the electrodes is a process that takes place over time, so instability of the arc increases over time. The *YAG lamps* were part of a experiment conducted a year prior



Figure 5.14 One of the electrodes of the *high InI YAG* lamp.

to the side-on measurements, and were therefore measured extensively before they were used in the side-on setup. This had an adverse effect on their stability. Unfortunately, it was not possible to create a ‘fresh’ set of YAG lamps, and we were limited to the lamps that were in our possession.

We aimed the bend of the arc towards the camera to test whether it was possible to scan a bended arc laterally. We took a series of photos approximately 10 s apart, which were then compared to see changes in the arc over time. During a lateral scan it takes approximately 30 minutes to measure the spectral radiance at 60 lateral points, which accounts for 30 s per measured spectrum, so the series of photos will indicate what the influence will be of arc instability on the side-on measurements.

The photos show that the arc could remain stable for times in the order of minutes, but also that the location of the arc could change suddenly and abruptly. Figure 5.15 shows the cross section of two photos taken in succession, 10 s apart. The figure shows that the center of the arc has shifted 0.1 mm between photos. The relative difference in pixel counts between the two curves at a certain lateral position varies up to 15 %. This difference lies at the lateral positions $y = 2.8$ mm and $y = 4.0$ mm, approximately 0.6 mm from the center of the arc. This is the point where the gradient of the pixel counts with respect to y is the largest. This makes the lateral measurements of the spectrum less reliable at these positions.

The stability measurements on the *low InI YAG* lamp showed the same shift of the center of the arc: 0.1 mm. The maximum difference in intensity is less than in the *high InI YAG*: 7 %, because the intensity profile of the *low InI YAG* is broader. The maximum difference again lay at approximately the same lateral location as for the *high InI YAG*: 0.8 mm from the center of the arc.

However, shifts in the order of 0.1 mm should not completely rule out the lateral measurements. The drifts in the arc can lead to under- or overestimations of the radiance at a certain lateral position. One of the goals of the lateral measurements is to Abel invert the data, in order to determine the local temperature. We noted earlier that the

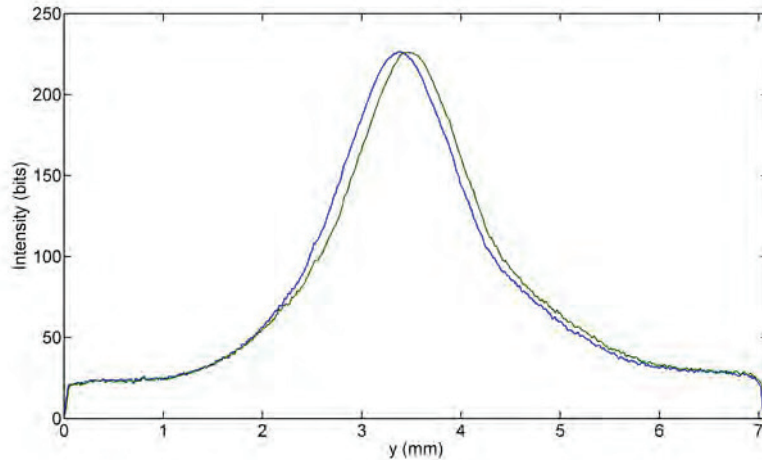


Figure 5.15 The horizontal cross section of two photos of the *high InI YAG* lamp, taken 10 s apart.

Abel inversion technique is fundamentally unstable, and that small errors in the lateral data will strongly influence the Abel inverted radial profiles. This is an important reason why the data should be fitted with functions that have an analytical solution to the Abel inversion, in our case the BASEX set. Fitting diminishes the influence small changes in the discharge on the Abel inverted radial profiles. However, as we can see in the next section, large shifts in the arc can still pose a problem.

5.3.2 Side-on measurements

We measured the *InI YAG* lamps in the side-on setup. The goals of these measurements were to confirm the measured temperatures of the InI lamps in the integrating sphere (see section 5.1.3), to find out from what areas in the lamp the line and molecular radiation originated and to create temperature profiles.

Unfortunately, we were not able to measure the *high InI YAG* lamp of the previous section due to instabilities, caused by the arc suddenly and abruptly shifting position. This affected the lateral measurements, which can be seen in figure 5.16. The figure shows that the center of the arc has shifted 1 mm in the lateral direction during the side-on measurement. The fact that the *high InI YAG* also had a bended arc means that accurate lateral measurements of this lamp were not possible.

Lateral profiles The *low InI YAG* lamps was stable, and could therefore be used for side-on measurements. The lamps was measured at different lateral positions in the spectral range between 4000 cm^{-1} ($2.5\text{ }\mu\text{m}$) and 8000 cm^{-1} ($1.25\text{ }\mu\text{m}$). This range of the spectrum features the atomic lines of indium used to determine the temperature. In the lateral measurement it was not possible to exactly determine the position of the line of sight with respect to the wall. We therefore placed the center of the arc $y = 0.0\text{ mm}$ at

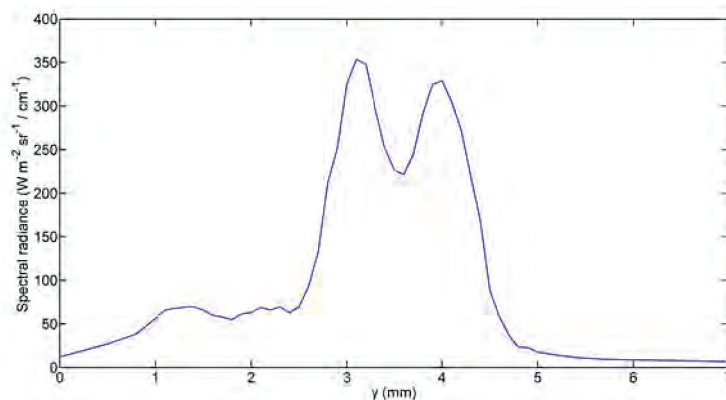


Figure 5.16 A lateral scan of the *high InI* YAG lamp at $\tilde{\nu} = 6792 \text{ cm}^{-1}$.

the lateral position where the total integrated radiance of the spectrum was the largest. Figure 5.17 shows the spectra measured at three different lateral positions: through the center of the arc ($y = 0.0 \text{ mm}$) and 1.0 mm and 2.0 mm outside the center.

As expected, the spectrum looks very much like the spectrum of the *InI* lamps measured in the integrating sphere (see figure 5.1). It shows that the continuum radiation actually decreases for smaller wavenumbers, something that was already deduced in section 5.1.1. The spectra show that the radiance of the atomic lines in the discharge decreases more rapidly outside the center than the radiance of the continuum. At $y = 2.0 \text{ mm}$ hardly any line radiation is detected. This means that the Boltzmann plots can only be used to determine the temperatures in the core of the discharge, as Boltzmann plots further outside the core will become less reliable.

The lateral scans can be used to compare the radiance of line emission versus continuum emission. The line radiance was separated from the continuum with the same method that was used to determine the Boltzmann plots (see section 4.3). The resulting curves were integrated between 4000 cm^{-1} ($2.5 \mu\text{m}$) and 8000 cm^{-1} ($1.25 \mu\text{m}$) in the spectral range. This resulted in figure 5.18.

The figure shows that the radiances of both the line radiation and the continuum radiation are the largest in the center of the lamps and then gradually reduces towards the wall. The line radiance almost completely disappears beyond $y = 1.5 \text{ mm}$. This decrease is slower for the continuum radiation. At $y = 3.0 \text{ mm}$, the continuum radiance is still 10 % of its maximum at $y = 0.0 \text{ mm}$. This figure shows that most atoms exist in a core, which also contains molecules. This core is surrounded by a molecular mantle, whose radiative output decrease towards the wall, in conjunction with the decrease of the temperature. There remains the fact that the center of the line radiance curve seems slightly shifted with respect to the continuum radiance curve, which results in an asymmetrical relative radiance profile. The continuum radiation profile is clearly asymmetrical. This is less obvious of the line radiation profile, although the figure shows that the ‘base line’ of the radiance is slightly higher right of the center than left of the

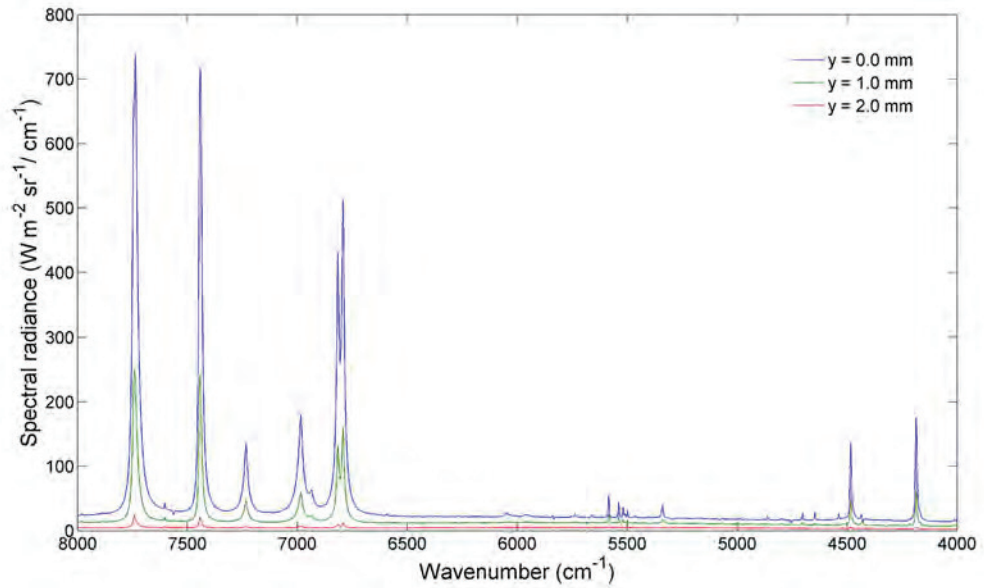


Figure 5.17 The spectrum of the *low InI* YAG lamp at three different lateral positions.

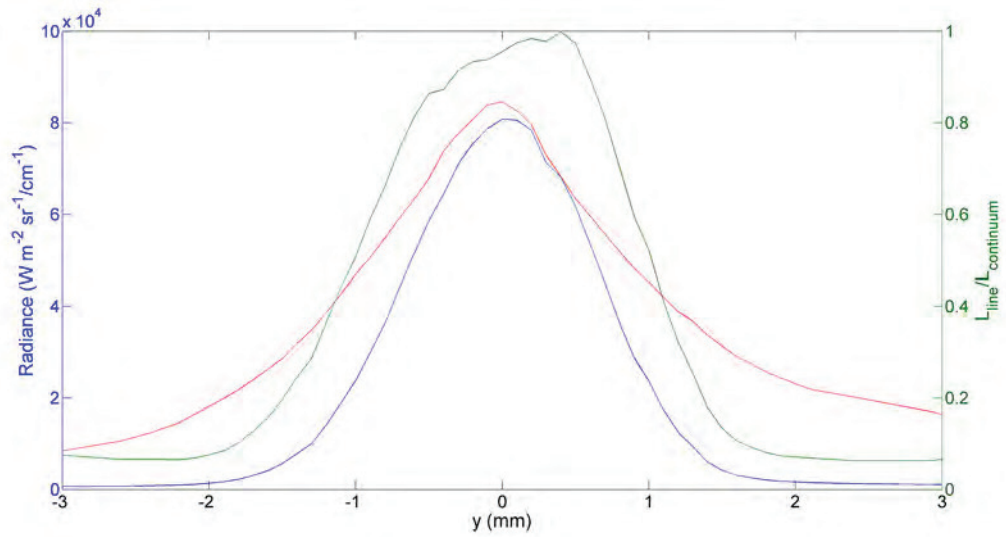


Figure 5.18 The lateral profiles of the line radiance and the continuum radiance spectrally integrated between 4000 cm^{-1} ($2.5\text{ }\mu\text{m}$) and 8000 cm^{-1} ($1.25\text{ }\mu\text{m}$), as well as the line radiance relative to the continuum radiance.

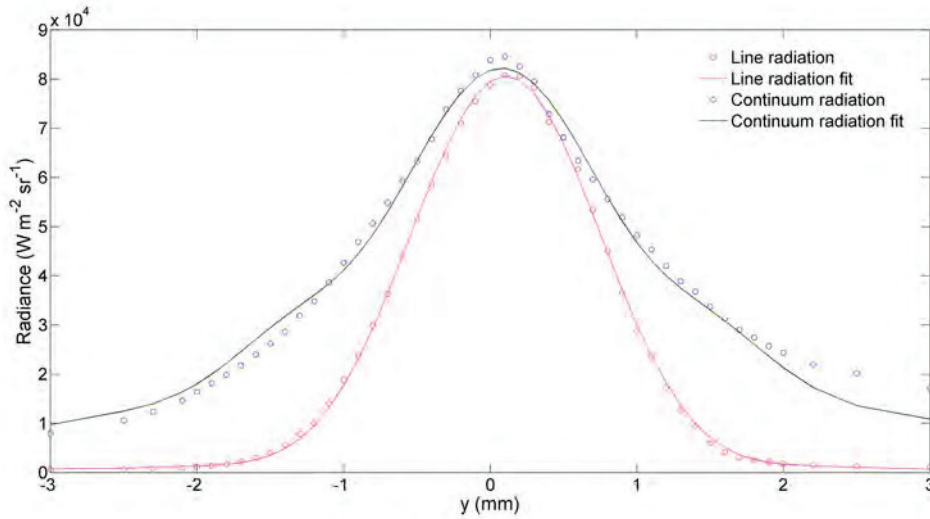


Figure 5.19 The lateral profiles of the line and continuum radiation were fitted with the BASEX set.

center. The fact that centers of the profiles are shifted with respect to each other an effect of the bending of the arc. This causes the center of the core to be slightly shifted with respect to center of the lamp. Now remember that lateral measurements are line of sight integral, whose line of sight decreases for $|y| > 0$. This will not matter for the line radiation, since it is emitted from a core with a finite length which is smaller than the length of the line of sight integral. The lateral profile of the continuum radiation will be affected, however, since it is emitted over the complete width of the lamp. The exact effect depends on the distribution of the continuum emission within the lamp.

The lateral profiles of the line and continuum emission were Abel inverted. Both profiles were therefore fitted with the BASEX set. This is shown in figure 5.19. This results in an almost perfect fit for the line radiation profile. The reason for this is that the line radiation profile has a very Gaussian form, and the equations of the BASEX set are Gaussian in nature. This fit of the continuum radiation profile is less precise. First of all, it was asymmetric, which was solved by averaging the left and the right side of the profile. Even then the continuum radiation profile was more ‘pointed’ than the line radiation profile, making it difficult to fit with the set of equations that we used. The fit could be more accurate if higher-order expressions of the BASEX set of equations were used, but this has its drawbacks. This is explained in section 4.4.

The resulting radial profiles are shown in figure 5.20. The graph confirms that the line radiation is emitted from a core with a radius of approximately 1.5 mm. The profile of the continuum radiation also shows continuum is both emitted from the core and from the mantle. The latter is especially interesting. In the original Elenbaas model, all radiation is emitted from the core. In this case, however, there is significant emission of continuum radiation in the mantle, especially the inner region of the mantle. A radial

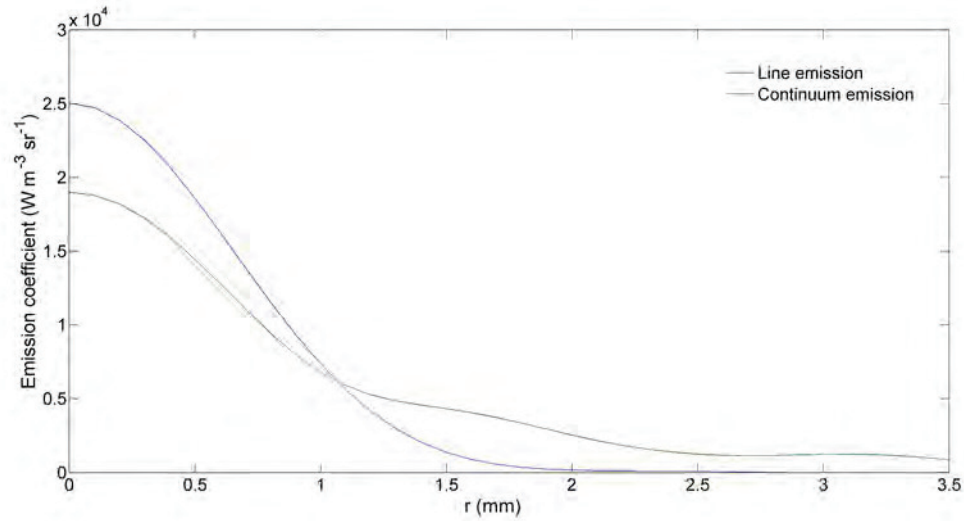


Figure 5.20 The emission coefficients of the line and continuum emission as a function of the radius.

temperature profile was created to see if the emission from the mantle had an influence on the temperature.

Radial profiles The atomic indium lines of lateral spectral profiles can be Abel transformed and then used to determine the temperature as a function of the radius. The transformation for the 6792 cm^{-1} line of the *low InI YAG* lamp is shown as an example in section 4.4. We Abel inverted the atomic lines of the spectrum, to see whether the temperatures could be replicated and to see whether the temperature profile shows contraction. The atomic indium lines that were used for the Boltzmann plots are listed in section 4.3. Figure 5.17 showed that line radiation decreases rapidly outside the center of the core. The Abel inverted profile can therefore only be used to determine the temperature (as a function of the radius) in the center of the lamp. The resulting temperatures as a function of the radius are shown in figure 5.21 by the blue dots. Figure 5.17 showed that the signal strength decreases rapidly further outside the core. The furthest point outside the core where a reliable Boltzmann plot could still be created was at $r = 1.6\text{ mm}$.

The measurement showed a core temperature of 4361 K. This is slightly higher than the temperatures detected in the integrating-sphere measurements. Both integrating-sphere measurements and side-on measurements have now shown that a typical core temperature of InI lamps consistently lie between 4000 K and 4500 K for lamps with only indium iodide filling. The uncertainty in the transition coefficients remain, however, so an error of 400 K in the temperature is to be expected, but the fact remains that these lamps are cool compared to the temperatures typically associated with CMH lamps. However, these temperatures were detected in high-pressure sodium (HPS) lamps [2], where the discharge is cooled by the efficient radiation of sodium. In CMH lamps small

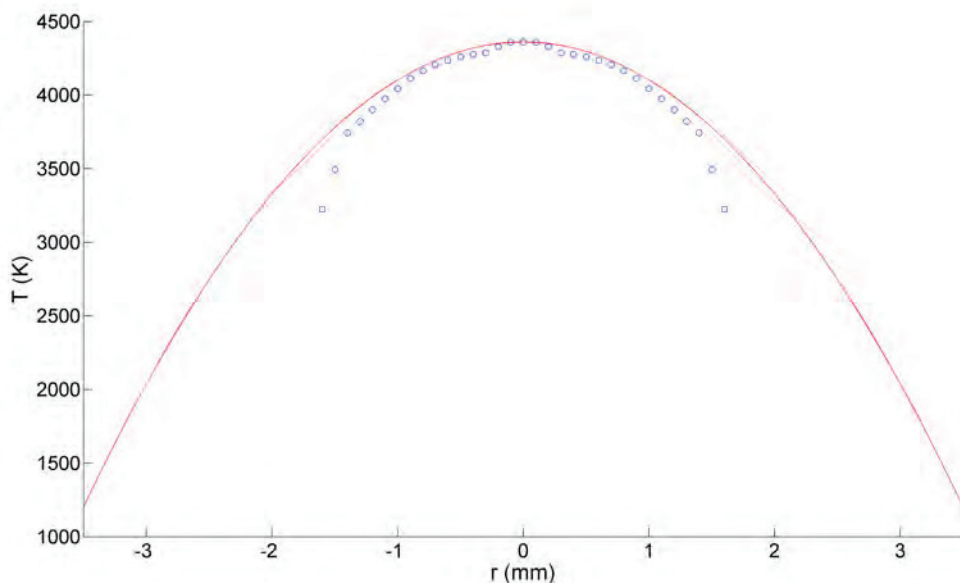


Figure 5.21 The temperature profile of the *low InI YAG* lamp. A parabolic curve is plotted through its maximum to show that the lamp has a contracted temperature profile.

additions of sodium often cool the outer core and the mantle, causing the core to contract and its temperature to increase. However, in HPS lamps, sodium is much more dominant, and its large presence combined with the fact that sodium is an efficient radiator reduces the core temperatures of these lamps. It is possible that the atomic indium but especially indium iodide are also very efficient radiators, especially considering their relatively low energy levels. This could result in a cool discharge, just like in HPS lamps. More important, however, is the fact this validates the use of Boltzmann plots in integrating-sphere measurements as an estimate for the core temperature.

The second important result of this measurement is the fact that this temperature profile gives definitive proof that the indium iodide indeed leads to contraction. In lamp theory, a non-contracted arc is assumed to be parabolic [44]. The measured temperature profile is contracted with respect to the parabolic curve. The center of the temperature curve is only slightly contracted with respect to the parabole, but further out of the core this temperature drops rapidly. As we have explained before, contraction can be the result of optically thin radiation in the outer core and the mantle. The radial profiles of figure 5.20 have already shown that there still is a significant emission of continuum radiation in outer core and mantle the discharge. Emission in the mantle is absent in a non-contracted discharge. This emission is responsible for the cooling down of the mantle and a decrease in temperature with respect to a parabolic temperature profile. This be seen in the the temperature profile of figure 5.21.

We have shown that the discharge of these lamps is contracted due to the emission of a molecular continuum. Moreover, a large part of this continuum lies in the infrared part

of the spectrum, which severely limits the efficacy of the lamp. This can be compensated partly by the addition of NaI-DyI₃ to the discharge. Their effect is not strong enough to lift the efficacy of indium iodide lamps to commercial levels. More importantly, their addition also leads to contraction of the arc. This, in combination with the fact that indium iodide already leads to contraction, limits the amount of additives that can be added to the discharge. As a consequence, InI is less suited as the buffer gas than mercury. In conclusion, lamps with InI as the buffer gas will not be as efficient as lamps with mercury.

5.4 Tin halides

The conclusion of the indium iodide measurements was that indium was unsuited for use as a buffer gas. The most important reasons for this were the emission of the infrared broad band radiation and the contraction of the arc. The question remained whether this was symptomatic of indium iodide or also the case for other metal-halide buffers. A new set of lamps were created which had tin halides as filling. Several studies have shown that tin mono-halides emit a broad band molecular continuum in the visible part of the electromagnetic spectrum [45, 46]. This raised the questions if tin halides could be used as a buffer gas, and if so, if its molecular continuum was limited to the visible part of the spectrum.

Therefore several lamps were created with tin bromide and tin iodide filling, to see if those metal halides were able to replace mercury. We also added a small amount of indium iodide to several lamps. The hypothesis was that indium iodide would still contribute to the voltage building qualities, but that the low amount of indium iodide could limit the output of infrared molecular radiation.

The choice was made to add NaI-DyI₃ to most lamps. It is still possible to investigate the buffer gas qualities of the tin halides with these salts present, while section 5.2.4 showed that the presence of NaI-DyI₃ had a positive influence on the efficacy of the lamps. We only made one lamp with only tin iodide and one lamp with only tin bromide in the salt pool, to investigate the continuum of the tin halides.

We were not able to measure these lamps with the same precision as the indium iodide lamps due to time constraints. Instead, we opted not to remove the discharge tubes from the bulb, so that the lamps could be measured under atmospheric conditions. This has several drawbacks. First, atmospheric conditions means that convection and conduction to the surrounding atmosphere will no longer be negligible. Also, much of the ultraviolet light is absorbed by the bulb, while water and carbon dioxide present in the atmosphere will absorb much of the far infrared radiation. The spectrum is therefore only reliable in a spectral range between 5000 cm⁻¹ and 26 500 cm⁻¹. Since the complete power output of the lamp could not be measured this way, it was not possible to create energy balances or Elenbaas plots of these lamps. However, the rest of the infrared spectrum and the visible spectrum could still be measured, so the effects of the tin halides and indium iodide on the spectrum of the lamps could be detected.

Lamp name	SnBr ₂ (mg)	NaI-DyI ₃ (mg)	U _{la} (V)	Efficacy (lm/W)
<i>SnBr</i> ₂	0.80	-	58.1	48
<i>SnBr</i> ₂ + <i>NaI-DyI</i> ₃	0.80	1.61	88.1	68

Table 5.6 Each lamp contained 350 mbar xenon as starter gas was driven at 70 W. The discharge tube was a Cosmo burner.

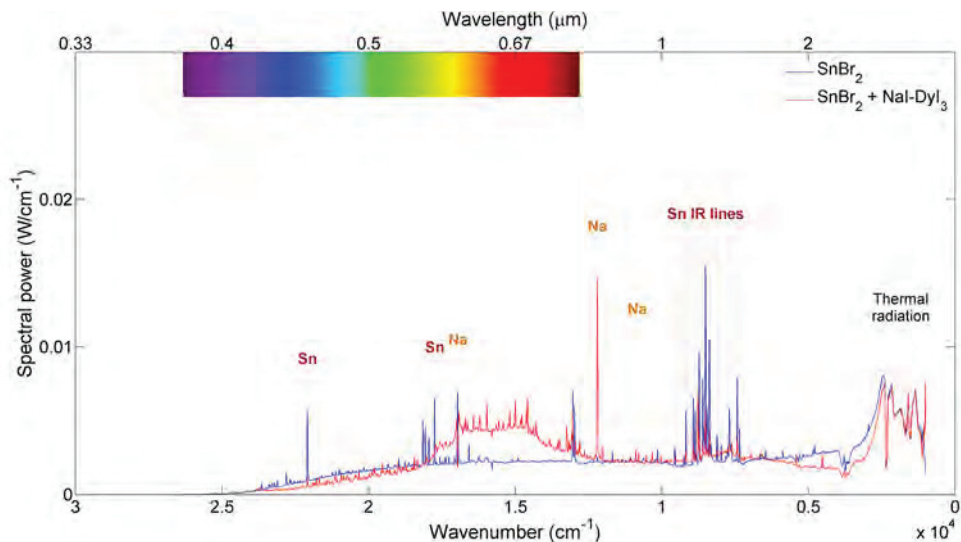


Figure 5.22 The electromagnetic spectra for lamps filled with SnBr₂ as the buffer gas. The graph shows a lamp with NaI-DyI₃ and a lamp without additives.

5.4.1 Tin bromide

Table 5.6 shows the fillings, lamp voltage and efficacy of two lamps with SnBr₂ as the buffer gas. The lamp voltage shows that the tin bromide has resistive qualities. The spectra of these lamps are shown in figure 5.22.

The spectrum of the *SnBr*₂ lamp looks very similar to the spectra of the *InI* lamps, except the thermal radiation bump. This shows large absorption bands of water and carbon dioxide. This is one of the reasons why it is not possible to create an energy balance for these lamps. Most of the lamp radiation is emitted as a broad band continuum, although some power is lost to atomic line emission as well. The atomic tin lines are mostly present in the infrared, just like the atomic lines in the *InI* lamps. Again trace amounts of other elements, such as sodium and potassium, can be seen in the spectrum. The unnamed line emission in the visible part of the spectrum are contaminations that can most likely be attributed to molybdenum and iron.

Ultraviolet radiation is absent from the spectrum. This may be due to the presence of the outer bulb, which is made of glass. Glass, however, is still partially transparent to ultraviolet radiation in the range shown in the graph, 330 nm - 380 nm, so it is not

enough to explain the complete absence of ultraviolet radiation in the spectrum. A similar process as in the *InI* lamps, where the ultraviolet radiance lines are absorbed by the molecules, can explain the absence of ultraviolet radiation in these tin lamps.

There is indeed a molecular continuum in the visible part of the spectrum, but it continues far into the infrared part of the spectrum, just like the continuum in *InI* lamps. The spectral power distribution of the continuum is constant in the infrared and red part of the spectrum, but decreases for wavelengths lower than 600 nm. We indeed measure the continuum that was detected by Drop et al. [45] and Chalmers et al. [46]. However, we also measure the infrared part of the spectrum, which shows that this continuum continues far into the infrared part of the spectrum. This is the reason behind the limited efficacy of the lamp.

The figure also shows a lamp of the same amount of SnBr_2 , but also with NaI-DyI_3 salts added to its filling. The changes in the spectrum are comparable to those in the *InI* + *NaI-DyI*₃ lamps. The sodium D line and the dysprosium continuum between 550 nm and 700 nm in the spectral range improve the efficacy of the lamp, which is raised by 20 lm/W to 68 lm/W. It also has an influence on the molecular continuum of tin bromide, which is lower in the visible part, but not in the infrared part of the spectrum. Just like in the *InI* lamps, this lowering is not very significant.

The atomic tin lines are much weaker in the lamp with additives. This effect is stronger in these lamps than in the *InI* lamps, because the energy levels and ionization levels of tin are of a higher energy than for atomic indium. Finally, there is less radiative output for the lamp with additives around 2 μm (5000 cm^{-1}). This is most likely due to a reduction in electrode radiation, since the current in the lamp with additives is much lower. This raises the point that this lamp has a higher resistivity. This means that the arc will be more contracted, because the additives emit optically thin radiation, which is again similar to the *InI* lamps.

Lamp name	SnBr_2 (mg)	NaI-DyI_3 (mg)	U_{la} (V)	Efficacy (lm/W)	T_c (K)
<i>Low SnBr</i> ₂	0.40	1.61	59.2	78	3367
<i>Medium SnBr</i> ₂	0.80	1.61	88.1	68	3623
<i>High SnBr</i> ₂	1.20	1.61	103.1	63	4264

Table 5.7 Each lamp contained 350 mbar xenon as starter gas. The input power was 70 W. The discharge tube was a Cosmo burner.

To test the influence of SnBr_2 on the spectra of the lamps three lamps were created with different amounts of SnBr_2 , see table 5.7. All lamps also contain NaI-DyI_3 . The spectral power distributions are shown in figure 5.23.

It is evident that SnBr_2 suffers from the same drawbacks as *InI*. Increasing the SnBr_2 leads to a suppression of the line radiation of the additives and an increase of the continuum radiation. Interestingly, figure 5.23 shows that a lamp with SnBr_2 filling emits a broad band molecular continuum. However, the visible part of this continuum

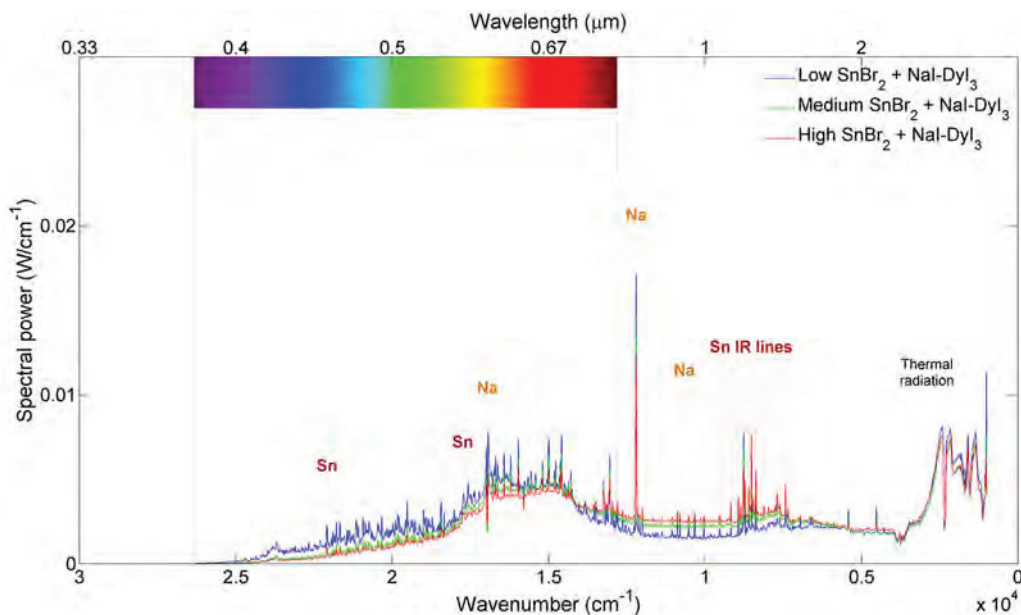


Figure 5.23 The spectral power distributions of three lamps with different amounts of SnBr_2 .

is suppressed with the addition of extra SnBr_2 , while the infrared continuum increases. This decreases the efficacy.

The atomic tin lines could not be used to determine the core temperature. The intensities of the 452.6 nm and 563.3 nm lines were too low to determine the power of these lines sufficiently accurate, while the transition coefficients are not known for the infrared tin lines. Therefore, 819 nm and 1141 nm sodium lines were used to estimate the core temperature. The resulting temperatures are quite low (see table 5.7), but this was also the case for the sodium lines in the *InI* lamps (see section 5.2.2). The possible reason is that the 819 nm line is not optically thin, especially since it is much more intense in the SnBr_2 lamps than in the *InI* lamps. This will lead to an underestimation of the temperature, since this line has a higher upper energy level than the 1141 nm line. A second reason is that the lamp might be de-mixed. Sodium is more likely to ionize than other species in the discharge. As a consequence the lamp might be de-mixed (see section 1.1.2.3). This means that most sodium will be present some distance for the center of the arc. Therefore most sodium could be radiating from an area with a lower temperature than the core of the discharge, which is reflected by the Boltzmann plots. The values for the core temperature are therefore only crude estimates. However, the trend shows that the core temperature increases with the increase of SnBr_2 . This could indicate that the core contracts as a result of the increase of optically thin molecular radiation emission.

While it was not possible to do the same in-depth analysis for lamps filled with tin bromide than for lamps filled with indium iodide, the spectra showed that both salts emit a strong continuum radiation. This lead to contraction of the arc column in indium

iodide lamps, and it seems plausible that the emission of the continuum would have the same effect on the tin bromide lamps. A large part of the continuum is infrared, which increases with the tin bromide dosage. This negatively influences the photometric properties of the lamp. Just like for the indium iodides the emission of the molecular band is partly suppressed by the addition of additives, but there remains significant molecular infrared emission. Tin bromide lamps will therefore have a limited efficacy.

Lamp name	SnBr ₂ (mg)	InI (mg)	NaI-DyI ₃ (mg)	U _{la} (V)	Efficacy (lm/W)	T _c (K)
<i>Low SnBr₂</i>	0.40	-	1.61	59.2	78	3367
	0.40	0.628	1.61	78.8	79	3484
	0.40	1.256	1.61	83.4	77	3798
<i>Medium SnBr₂</i>	0.80	-	1.61	88.1	68	3623
	0.80	0.628	1.61	96.7	68	3764
	0.80	1.256	1.61	98.3	69	3954
<i>High SnBr₂</i>	1.20	-	1.61	103.1	63	4264
	1.20	0.628	1.61	106.1	62	4057
	1.20	1.256	1.61	115.3	59	4245

Table 5.8 Each lamp contained 350 mbar xenon as starter gas. The input power was 70 W. The discharge tube was a Cosmo burner.

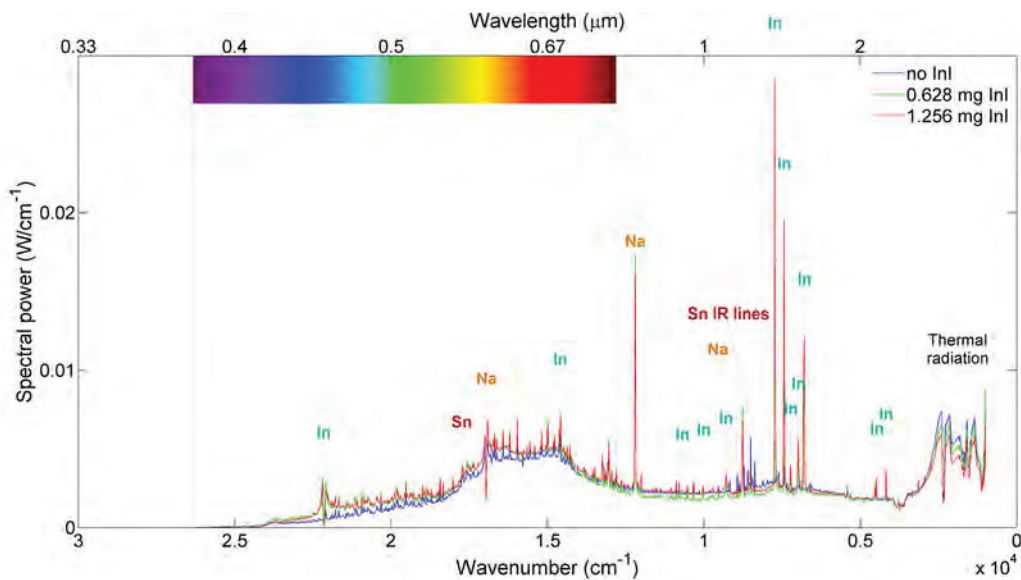


Figure 5.24 The spectra of *medium SnBr₂* lamps with varying InI filling.

We did also create several lamps with the same tin bromide filling as the lamps of table 5.7, but with small amounts of InI added to the filling. This choice was made under

the assumption that tin bromide would mostly radiate in the visible part of the spectrum. The hypothesis was that we perhaps could use the resistive qualities of InI combined with the visible continuum radiation of SnBr₂. We have just shown that the continuum radiation of tin bromide continues into the infrared, so tin bromide can be dismissed as an effective radiator of visible radiation. Nevertheless, it remains interesting to see what the added influence of indium iodide was. Their fillings, lamp voltage, efficacy and core temperature are listed in table 5.8.

The influence of indium iodide on the spectrum was the same for *low*, *medium* and *high* SnBr₂ lamps. As an example the spectra of the *medium* SnBr₂ lamps are shown in figure 5.8. The addition of InI has very little influence on the visible spectrum of the lamps, which is reflected by the efficacy of the lamps. There is, however, an increase of continuum radiation in the infrared part of the spectrum. Despite the absorption bands the height of the thermal bump shows that this leads to a reduction of the thermal radiation of the burner wall. This continuum increase cannot directly be attributed to InI, because indium will react with bromine and tin will react with iodine in the spectrum, so there is a large variation of molecular species present in the discharge.

The addition of InI does have positive effects on the lamps voltage, which increases for the *low*, *medium* and *high* SnBr₂ lamps, although the effect is the strongest for the lamps with the 0.40 mg SnBr₂ filling. The core temperature was again determined from the sodium lines. The indium lines could not be used, as it was not possible to separate them from the infrared tin lines. The core temperature increases for the *low* and *medium* SnBr₂ lamps. This is not the case for *high* SnBr₂ lamps. We already saw in the *InI* lamps that an increase in salt pool filling does not have a linear effect in the core densities. Perhaps this affects the *high* SnBr₂ lamps more strongly, since its salt pool is already more filled than the *low* and *medium* SnBr₂ lamps. Again, the combination of an increase in molecular radiation and core temperature seems to point to contraction of the arc due to InI. In conclusion, addition of InI reduces thermal losses and increase lamp voltage, which reduces wall losses, for tin bromide lamps, but does not improve the efficacy of the lamp.

5.4.2 Tin iodide

Tin bromide was not the only halide that seemed suitable for use as the buffer gas, tin iodide was also tested. Table 5.9 shows the details of two tin iodide lamps, one with and one without additives. The electromagnetic spectra of these lamps are shown in figure 5.25.

Lamp name	SnI ₂ (mg)	NaI-DyI ₃ (mg)	U _{la} (V)	Efficacy (lm/W)
SnI ₂	1.06	-	46.0	42
SnI ₂ + NaI-DyI ₃	1.06	1.61	85.7	64

Table 5.9 Each lamp contained 350 mbar xenon as starter gas. The input power was 70 W. The discharge tube was a Cosmo burner.

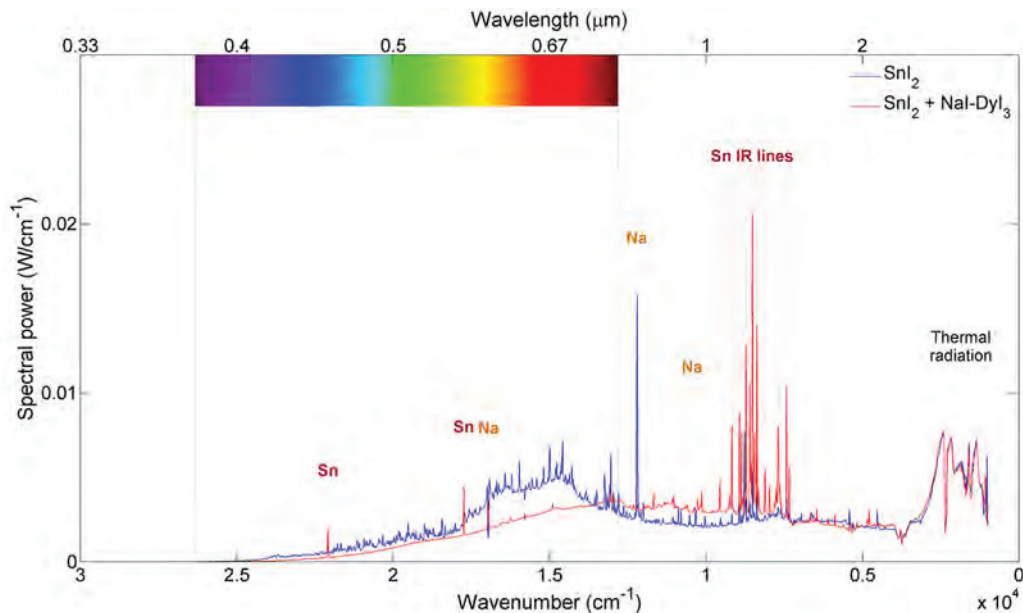


Figure 5.25 The electromagnetic spectra for lamps filled with SnI_2 as the buffer gas. The graph shows a lamp with and a lamp without NaI-DyI_3 .

The spectrum for the SnI_2 lamps is comparable to that of the SnBr_2 lamps. Much of the radiant flux is emitted in the form of a continuum, which runs from the infrared to the visible part of the spectrum, with ultraviolet radiation absent from the spectrum. The only atomic line radiation results from tin, mostly in the infrared, and traces of sodium. The spectral power of the continuum is constant in the infrared part of the spectrum, but decreases steadily for lower wavelengths in the visible part of the spectrum. This decrease starts at 700 nm. The efficacy of the SnI_2 lamps is lower than the efficacy of either pure SnBr_2 or pure InI lamps. The efficacy is again increased by adding NaI-DyI_3 . The addition of additives increases the efficacy with 22 lm/W. A similar increase was seen in the SnBr_2 lamps. However, again the additives do not significantly suppress the infrared part of the continuum.

To further investigate the influence of SnI_2 three lamps were created with different doses of SnI_2 . Their details can be seen in table 5.10. Their spectra are shown in figure 5.26.

The trends are identical to those of the SnBr_2 lamps. When the amount of SnI_2 is increased, both line radiation and a part of continuum in the visible part of the spectrum decreases, while the continuum in the infrared increases. This lowers the efficacy. The core temperature was calculated with sodium lines. The resulting temperatures are again relatively low, but do indicate an increase in core temperature. The increase in molecular radiation and the increase in core temperature suggest that the same mechanism is at play as for the other lamps: increased contraction due to the emittance of molecular radiation. This again limits the amount of additives that can be added to the lamp,

Lamp name	SnI ₂ (mg)	NaI-DyI ₃ (mg)	U _{1a} (V)	Efficacy (lm/W)	T _c (K)
<i>Low SnI₂</i>	0.51	1.61	63.4	77	3131
<i>Medium SnI₂</i>	1.06	1.61	85.7	64	3387
<i>High SnI₂</i>	1.61	1.61	93.0	53	3829

Table 5.10 Each lamp contained 350 mbar xenon as starter gas. The input power was 70 W. The discharge tube was a Cosmo burner.

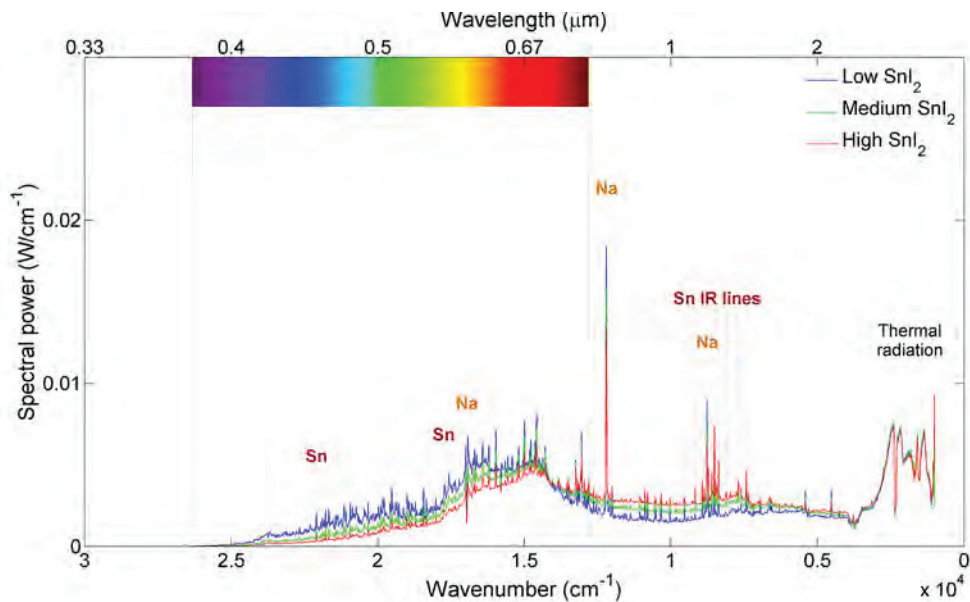


Figure 5.26 The spectral power of three lamps with different amounts of SnI₂ filling.

so SnI₂ does not meet the criteria to replace mercury. In conclusion, neither SnI₂ nor SnBr₂ suffices as a buffer gas.

Chapter 6

Conclusion and outlook

6.1 Conclusion

In this work we investigated indium iodide as an alternative to mercury in CMH lamps. Mercury acts as a buffer gas in such lamps because of its large electron-atom collisional cross section. Indium was considered to be a viable alternative, since it has an even larger electron-atom cross section than mercury. Lamps were filled with indium iodide in order to create a sufficient atomic indium vapor pressure in the discharge, since metal halides evaporate more easily than metals.

A variety of lamps were created. Several lamps had only indium iodide as filling. The goal of these lamps was to investigate the radiative and resistive properties of the indium iodide. Other lamps also had additives added to the filling, i.e. sodium iodide and dysprosium iodide. Typical CMH lamps have additives added to their filling to increase their efficacy. The lamps with additives we measured to determine the buffer gas qualities of indium iodide, for instance, whether the spectrum would be dominated by the additives or if indium iodide would still significantly contribute to the radiation.

The spectrum of the indium iodide lamps showed that most of the plasma radiation was emitted in the form of a continuum between wavelength of 400 nm and 3 μm , while only a small part of the plasma radiation was emitted in the form of atomic line radiation. There was an almost complete absence of ultraviolet radiation. Bremsstrahlung and recombination radiation were considered as a source for this continuum. To estimate their contribution to the spectrum we used a simplified model of the plasma: the channel model, in which the discharge is represented as a cylinder with constant temperature and densities. These estimates showed that these processes contributed less than 3 % to the total plasma radiation power.

Molecular transitions within the InI molecule are also able to emit a continuum. An investigation of the energy levels of molecular indium iodide showed that it is capable of absorbing ultraviolet radiation and emitting a broad continuum in the range of the measurements. Simulations within the EPG group indeed confirmed that molecular transitions are responsible for the emission of the continuum.

An increase in indium iodide in the filling lead to an increased resistivity of the

discharge, in line with what was expected. The spectra and energy balance showed that an increase of indium iodide filling leads to a decrease of the non-radiative losses, but an increase in infrared plasma radiation, while the efficacy between the lamps remained relatively unaffected. By applying the channel model we deduced that the indium iodide leads to contraction of the arc column. Arc contraction can be caused by the increased emission of optically thin molecular radiation.

These findings were confirmed by measurements in the side-on setup. Lateral scans showed that the discharge consisted of a core from which most optically thin atomic line radiation was emitted. Molecular radiation was emitted from both the core and the mantle. The temperature profiles from the side-on measurements also showed that indium iodide causes contraction due to emission from the mantle. The side-on measurements also confirmed that optically thin lines in integrating-sphere measurements can be used to estimate the core temperature.

The addition of sodium iodide and dysprosium did improve the photometric qualities of the lamp. The best efficacy was measured for a lamp with 1.08 mg InI and 1.49 mg NaI-DyI₃: 87 lm/W, an increase of 25 lm/W compared to the lamp without additives. The addition of additives would decrease the continuum emission, although they would still be considerable infrared continuum emission. More problematic is the fact that both indium iodide and the additives cause the arc column to contract. This limits the amount of additives that can be added to the lamp. If more additives are added to the lamp there will be a large chance that the arc will become unstable.

Tin halide lamps were also investigated, but less extensively than indium iodide. The spectral measurements did show the same trends of tin bromide and tin iodide as for indium iodide: a large continuum broad band that ranges from the visible to the infrared part of the spectrum, absence of ultraviolet emission and relatively low atomic line radiation emission compared to continuum emission. Both tin bromide and tin iodide could be used to increase the resistivity of the lamp, although tin. A lamp with 0.40 mg tin bromide and 1.61 mg NaI-DyI₃ added to the filling reached an efficacy of 79 lm/W. However, the efficacy would decrease if the amount of tin halide in the filling would increase, an effect that was already witnessed in indium iodide lamps. The measurements showed that neither tin bromide nor tin iodide as a viable alternative to mercury.

6.2 Outlook

The experimental ssetup functioned well during the project. We recommend only two small improvements. In our lamps there was very little emission of ultraviolet radiation. However, if to accurately measure the spectral power in the ultraviolet a calibration source would have to be found. Secondly, the ports of the fiber optic spectrometer and FTIR spectrometer are placed in different places in the sphere, which gives an unwanted discrepancy between the two. It would be recommended to place the port of the fiber optic spectrometer nearer to the port of the FTIR spectrometer.

Regrettably, research into mercury-free CMH lamps will not be continued by Philips

and the TU/e. This is unfortunate, as we have created an experimental setup that it is able to determine indepth the behavior of various CMH lamps. The combination of the integrating sphere and side-on setup proved to be highly effective. In case other buffer gases were ever tested, it would be recommended that, in combination with conventional PCA lamps, several lamps with a YAG burner would be created for side-on measurements.

The question still remains whether it is not possible to replace with metal-halides. There are strong indications that these lamps will emit much molecular radiation. A suitable metal halide would therefore have to emit mostly visible molecular radiation. But even if this is the case, there is still the risk that the metal halide causes sever arc contraction. Some tests at Philips showed metal halides that would merit further investigation, but considering the fact that the project is ending, this will most likely remain a question.

Acknowledgements

When I came to Gerrit asking for a project he immediately pointed me in Arij's direction. The subject of discharge lamps immediately grabbed my interest and one week later I was measuring my first lamps. I can only say that this has been informative year I have experienced at the TU/e, and that this is thanks to the people I have had the privilege to cooperate with.

First and foremost I have Arij to thank. I know how hard you have had to work this last year, raising three children and having to finish a PhD thesis, yet I have never had the feeling that you did not have time to discuss my results or help me come up with new ideas. I cannot express enough how I appreciate that you found time to answer my lengthy e-mails or even show up after work to discuss the progress of my thesis even while you were already working at ASML.

Secondly, I like to thank the Friday afternoon HID 'club'. Jesper, I really enjoyed our discussions, especially near the end of my project. Without your efforts I would never have gained the insight into the measurements that I have now. I wish you the best of luck getting your PhD. I like to thank Sander, whose often had the right tip to help me on my way experimentally. His experimental skills show no sign of diminishing despite spending most of his time in an (air-conditioned) office. I also like to thank Maxime, whose enthusiasm never faded. Your encyclopedic knowledge on HID lamps was truly inspiring. Finally, I like to thank Jos Suijker. I could not have written a large part of this thesis without your determination to get me the transition coefficients of the infrared lines of atomic indium.

I like to thank everybody of the technical support staff who helped me throughout the year. Paul Beijer and Jovita Moerel made a great H bridge for me. Ab, Loek, Eddy, Evert, Huib en Ries, your assistance has been greatly appreciated throughout the year. It remains amazing how much stuff can break down through no fault of your own.

Many thanks to the different room mates I have had throughout the year, especially Anneke, Leroy, Paul, Ben, Luuk, Rob and Koen, I always enjoyed our conversations and apologize for my incessant blabbering. A big thank you to the rest of EPG for all the fun lunches.

Finally, I like to thank Gerrit. We have not seen much of each other throughout the year, but I never considered this a problem. I enjoyed the great barbecues and consider the day at Six Flags Great Adventure as the pinnacle of the BuEx USA.

Bibliography

- [1] M.J.H. Kessels. High-pressure discharge lamp containing a starter antenna, Jul. 22, 2010. US Patent 0181910.
- [2] J. de Groot and J. van Vliet. *The high-pressure sodium lamp*. Philips Technical Library, 1986.
- [3] G.G. Lister, J.E. Lawler, W.P. Lapatovich, and V.A. Godyak. The physics of discharge lamps. *Review of Modern Physics*, 76:542–593, 2004.
- [4] W.M. Keeffe. Recent progress in metal halide discharge-lamp research. *Physical Science, Measurement and Instrumentation, Management and Education - Reviews, IEE Proceedings A*, 127:181–189, 1980.
- [5] J.F. Waymouth. *Electric Discharge Lamps (Monographs in Modern Electrical Technology)*. M.I.T. Press, 1971.
- [6] P. Flesch. *Light and Light Sources: High-intensity Discharge Lamps*. Springer, 2006.
- [7] J. Melis. Low frequency square wave electronic ballast for gas discharge, Jun. 27, 1995. US Patent 5428628.
- [8] A.J. Rijke, T.L. Lemmens, J.F.J. Janssen, S. Nijdam, Haverlag. M., J.J.A.M. Van der Mullen, and G.M.W. Kroesen. Quantitative assessment of the energy balances of three generations of ceramic high intensity discharge lamps. *Poster and Landmark Lecture at the 13th International Symposium on the Science and Technology of Lighting*, 1:LL09 183–184, 2012.
- [9] T.W. Clarkson. Mercury: Major issues in environmental health. *Environmental Health Perspectives*, 100:31–38, 1992.
- [10] Mercury study report to congress. US Environmental Protection Agency, December 1997.
- [11] G.H. Reiling. Characteristics of mercury vapor-metallic iodide arc lamps. *Journal of the Optical Society of America*, 54:532–540, 1964.

Bibliography

- [12] M. Born. Investigations on the replacement of mercury in high-pressure discharge lamps by metallic zinc. *Journal of Physics D: Applied Physics*, 34:909–924, 2001.
- [13] M. Born. Physics of mercury-free high-pressure discharge lamps. *Plasma Sources Science and Technology*, 11:A55–A63, 2002.
- [14] A.G. Jack and M. Koedam. Energy balances for some high pressure gas discharge lamps. *Journal of Illuminating Engineering Society*, 3:323–329, 1974.
- [15] D.O. Wharmby. Energy balance of high-pressure sodium discharges under controlled vapour conditions. *Journal of Physics D: Applied Physics*, 17:367–378, 1984.
- [16] A.J. Rijke, S. Nijdam, Haverlag. M., J.F.J. Janssen, J.J.A.M. van der Mullen, and G.M.W. Kroesen. A calibrated integrating sphere setup to determine the infrared spectral radiant flux of high-intensity discharge lamps. *Journal of Physics D: Applied Physics*, 44:224007, 2011.
- [17] D.J. Smith, G.A. Bonvallet, and J.E. Lawler. Infrared losses from a na/sc metal-halide high intensity discharge arc lamp. *Journal of Physics D: Applied Physics*, 36:1519–1528, 2003.
- [18] M.T. Herd and J.E. Lawler. Infrared continuum radiation from metal halide high intensity discharge lamps. *Journal of Physics D: Applied Physics*, 40:3386–3395, 2007.
- [19] F. Cabannes and J.. Chapelle. *Reactions under Plasma Conditions*. Wiley, New York, 1971.
- [20] L.M. Biberman and G.E Norman. On the calculation of photoionization absorption in atomic gases. *Optics and Spectrometry*, 10:297, 1961.
- [21] A.J. Rijke. *The Power Balance of Ceramic Metal-Halide High Intensity Discharge lamps*. PhD thesis, Eindhoven University of Technology, 2013.
- [22] W. Elenbaas. *The High Pressure Mercury Vapor Discharge*. North-Holland Publishing Co., 1951.
- [23] M.J. Buie, J.T.P. Pender, J.P. Holloway, T. Vincent, P.L.G. Ventzek, and M.L. Brake. Abel’s inversion applied to experimental spectroscopic data with off axis peaks. *Journal of Quantitative Spectroscopy and Radiative Transfer*, 55:231–243, 1996.
- [24] V. Dribinski, A. Ossadtschi, V.A. Mandelshtam, and H. Reisler. Reconstruction of abel-transformable images: The gaussian basis-set expansion abel transform method. *Review of Scientific Instruments*, 7:2634–2642, 2002.
- [25] A. Griffiths, Peter and James A. de Haseth. *Fourier Transform Infrared Spectroscopy*. John Wiley and Sons, 1986.

- [26] Labsphere. Technical guide: Integrating sphere theory and applications. <http://mmrc.caltech.edu/Cary%20UV-Vis%20Int.Sphere/labsphere%20Theory%20and%20App.pdf>.
- [27] J.C. de Vos. *The emissivity of tungsten ribbon : the tungsten striplamp as a standard source of radiation*. PhD thesis, University of Amsterdam, 1953.
- [28] A.E. Westlund and R.T. Fleming. Tungsten halogen lamp with heat-dissipating base, Feb. 4, 1986. US Patent 4,568,854.
- [29] Transmittance of quartz. http://www.technicalglass.com/fused_quartz_transmission.html. Technical Glass Products.
- [30] R.E. Rolling, A.I. Funai, and J.R. Grammer. Investigation of the effect of surface conditions on the radiant properties of metals. Air Force Materials Laboratory (U.S.), Lockheed Missiles and Space Company, 1964.
- [31] Y.S. Touloukian and D.P. DeWitt. *Thermal Radiative Properties: Metallic Elements and Alloys*. IFI/Plenum, 1970.
- [32] S. Nijdam. Eldes 2, a 2d phase resolved hid electrode model. Philips report CDL 04/10018 (restricted).
- [33] U.I. Safronova, M.S. Safronova, and M.G. Kozlov. Relativistic all-order calculations of in i and sn ii atomic properties. *Physical Review A*, 76:022501, 2007.
- [34] A. Kramida, Y. Ralchenko, J. Reader, and NIST ASD Team. Nist atomic spectra database. <http://physics.nist.gov/asd>, 2012.
- [35] Z. Felfli, A.Z. Msezane, and D. Sokolovski. Slow electron elastic scattering cross sections for in, tl, ga and at atoms. *Journal of Physics B: Atomic, Molecular and Optical Physics*, 45:045201, 2012.
- [36] J.E. Lawler, A. Koerber, and U. Weichmann. Infrared continuum radiation from high and ultra-high pressure mercury lamps. *Journal of Physics D: Applied Physics*, 38:3071–3085, 2005.
- [37] J.R. England and M.T. Elford. Momentum transfer cross section for electrons in mercury vapour derived from drift velocity measurements in mercury vapour-gas mixtures. *Australian Journal of Physics*, 44:647–675, 1991.
- [38] O. Zatsarinny, K. Bartschat, G. Garcia, F. Blanco, L.R. Hargreaves, D.B. Jones, R. Murrie, J.R. Brunton, M.J. Brunger, M. Hoshino, and J. Buckman. Electron-collision cross sections of iodine. *Physical Review A*, 83:042702, 2011.
- [39] R. Ruyves, V. Kelman, Y. Zhmenyak, and Y. Shpenik. Proposal for laser on self-terminating transition in blue spectral range on indium atom transition atoms 451.1 nm. *Radiation Physics and Chemistry*, 68:269–272, 2003.

Bibliography

- [40] A. Banerjee and K.K. Das. Theoretical spectroscopic studies of InI and InI^+ . *International Journal of Quantum Chemistry*, 112:453–469, 2012.
- [41] M. Gnybida, J.F.J. Janssen, J. Van Dijk, J. Suijker, M. Gendre, and G.M.W. Kroesen. Numerical investigation on the replacement of mercury in hid lamps. *Submitted to: Journal of Physics D: Applied Physics*, 2013.
- [42] M. Käning, L. Hitzschke, M. Berger, S. Franke, and R. Methling. Mercury-free high pressure discharge lamps dominated by molecular radiation. *Journal of Physics D: Applied Physics*, 44:244005, 2011.
- [43] J. Perel, J. Englander, and B. Bederson. Measurement of total cross sections for the scattering of low-energy electron by lithium, sodium and potassium. *Physical Review*, 128:1148–1154, 1962.
- [44] Fischer. *Influences of External and Self-Magnetic Fields on the Behaviour of Discharge Lamps*. Philips GmbH Forschungslaboratorium Aachen Lobornotiz nr. 13/78, 1978.
- [45] P.C. Drop, J.J. de Groot, A.G. Jack, and G.C.J. Rouweler. Some aspects of the tin halide molecular arc. *Lighting Research and Technology*, 6:212–216, 1974.
- [46] A.G. Chalmers, D.O. Wharmby, and F.L. Whittaker. Comparison of high-pressure discharges in mercury and the halides of aluminium, tin and lead. *Lighting Research and Technology*, 7:11–18, 1975.